NEAR INFRARED SPECTROSCOPY BASED FUNCTIONAL NEUROIMAGING: NEURAL CORRELATES AND APPLICATIONS IN NEURO-REHABILITATION

Dissertation

der Mathematisch-Naturwissenschaftlichen Fakultät

der Eberhard Karls Universität Tübingen

zur Erlangung des Grades eines

Doktors der Naturwissenschaften

(Dr. rer. nat.)

vorgelegt von

Ali Danish Zaidi

aus Neu Delhi, Indien.

Tübingen
2018

Gedruckt mit Genehmigung der Mathematisch-Naturwissenschaftlichen Fakultät der

Eberhard Karls Universität Tübingen.

Tag der mündlichen Qualifikation:	23.09.2021
Dekan:	Prof. Dr. Thilo Stehle
1. Berichterstatter:	Prof. Dr. Wolfgang Rosenstiel
2. Berichterstatter:	Prof. Dr. Niels Birbaumer

Declaration:

I hereby declare that I have produced the work entitled "Near infrared spectroscopy based functional neuroimaging: neuronal correlates and applications in neuro-rehabilitation", submitted for the award of a doctorate, on my own (without external help), have used only the sources and aids indicated and have marked passages included from other works, whether verbatim or in content, as such. I swear upon oath that these statements are true and that I have not concealed anything. I am aware that making a false declaration under oath is punishable by a term of imprisonment of up to three years or by a fine.

Tübingen, den ....

Date Signature

This work is dedicated to Mujtaba Husain Zaidi (Papamiyaan)…

CONTENTS

ACKNOWLEDGEMENTS

This work would not have been possible without the nurturing support and guidance of my two mentors, who went to great lengths to ensure my success. Professor Niels Birbaumer and Professor Ranganatha Sitaram have been a constant source of inspiration, wisdom, guidance and support in good times, as well as counselling and encouragement in bad ones. They have been constantly available and approachable despite their incredibly busy schedules and engagements. Talking to them, specifically when things were going south, would lift spirits and enable me to see the bigger picture. On innumerable occasions, I have entered their offices in hopeless despair, and have come out smiling. I thank them in believing in me when no one else would. It has been an honor and a pleasure to be associated with them.

I am indebted to Professor Nikos Logothetis, for allowing me into his lab. The exposure in his lab taught me a great deal about the sacrifice and commitment required to pursue high quality science, and was an incredible learning experience. Towards the end of this work, he went through very difficult times, and yet was always there to lend his support or feedback on issues with the kindest smile. I am also indebted to Professor Eberhard Fetz, who took out the time to discuss my projects and results, and was readily available to answer queries or debate results and interpretations.

Finally, this work wouldn't have been possible without the love and support of my family and friends.

Abbreviations

ALS:	Amyotrophic Lateral Sclerosis
BCI:	Brain-computer interface
EPI:	Echo-planar imaging
fMRI:	functional Magnetic Resonance Imaging
fNIRS:	functional Near-Infrared Spectroscopy
HBO:	Oxygenated hemoglobin
HBR:	Deoxygenated hemoglobin
HBT:	Total hemoglobin
LFP:	Local field potential
ME:	Movement Execution
MI:	Movement Imagery
SNR:	Signal to noise ratio
SVM:	Support-vector machine

ABSTRACT

Simultaneous measurements of intra-cortical electrophysiology and hemodynamic signals in primates are essential for relating human neuroimaging studies with intra-cortical electrophysiology in monkeys. Previously, technically challenging and resourcefully demanding techniques such as fMRI and intrinsic-signal optical imaging have been used for such studies. Functional near-infrared spectroscopy is a relatively less cumbersome neuroimaging method that uses near-infrared light to detect small changes in concentrations of oxy-hemoglobin (HbO), deoxy-hemoglobin (HbR) and total hemoglobin (HbT) in a volume of tissue with high specificity and temporal resolution. In a series of studies, we investigated the neurovascular correlates of fNIRS signals in primates and demonstrated its feasibility in brain-state classification for applications in brain-computer interfaces and neurofeedback in humans in four studies.

To test the feasibility of using epidural fNIRS with concomitant extracellular electrophysiology, in our first study we recorded neuronal and hemodynamic activity from the primary visual cortex of two anesthetized monkeys during visual stimulation. We recorded fNIRS epidurally. We performed simultaneous cortical electrophysiology using tetrodes placed between the fNIRS sensors. We observed robust responses to the visual stimulation in both [HbO] and [HbR] signals, and quantified the signal-to-noise

ratio of the epidurally measured signals. Our results show that epidural fNIRS detects single-trial responses to visual stimuli on a trial-by-trial basis, and when coupled with cortical electrophysiology, is a promising tool for studying local hemodynamic signals and neurovascular coupling.

A major issue with functional neuroimaging, is that the neuroimaging signal correlates with both spiking, and various bands of the local field potential (LFP), making the inability to discriminate between them a serious limitation for interpreting hemodynamic changes. In our second study, we use the technique described above to investigate the neuro-vascular correlates of the fNIRS signals, and find that low-frequency LFPs correlate with the hemodynamic signal's peak amplitude, whereas spiking correlates with its peak-time and initial-dip. We also find spiking to be more spatially localized than low-frequency LFPs. Our results suggest that differences in the spread of spiking and low-frequency LFPs across cortical surface influence different parameters of the hemodynamic response. These results demonstrate that the hemodynamic response-amplitude is a poor correlate of spiking activity. Instead, we demonstrate that the timing of the initial-dip and the hemodynamic response are much more reliable correlates of spiking, reflecting bursts in spike-rate and total spike-counts respectively.

In our third study, we turned our attention to the initial-dip. The initial-dip is a transient decrease frequently observed in functional neuroimaging signals, immediately after stimulus onset, and is believed to originate from a rise in deoxy-hemoglobin (HbR) caused by local neural activity. It has been shown to be more spatially specific than the hemodynamic response, and is believed to represent focal neuronal activity. However, despite being observed in various neuroimaging modalities (such as fMRI, fNIRS, etc), its origins are disputed and its neuronal correlates unknown. Here, we show that the initial-dip is dominated by a decrease in total-hemoglobin (HbT). We also find a

biphasic response in HbR, with an early decrease and later rebound. However, HbT decreases were always large enough to counter spiking-induced increases in HbR. Moreover, the HbT-dip and HbR-rebound were strongly coupled to highly localized spiking activity. Our results suggest that the initial-dip helps prevent accumulation of spiking-induced HbR concentration in capillaries by flushing out HbT, probably by active venule dilation.

The purpose of our fourth study was to develop and test a real-time method for subject-specific and subject-independent classification of multi-channel fNIRS signals using support-vector machines (SVM), to determine its feasibility as an online neurofeedback system. We used left versus right hand movement execution and movement imagery as study paradigms in a series of experiments. In the first two experiments, activations in the motor cortex during movement execution and movement imagery were used to develop subject-dependent models that obtained high classification accuracies thereby indicating the robustness of our classification method. In the third experiment, a generalized classifier-model was developed from the first two experimental data, which was then tested in new subjects. Application of this method in new participants showed mean classification accuracy of 63% for movement imagery tasks and 80% for movement execution tasks. These results demonstrate that SVM based real-time subject-independent classification of fNIRS signals is feasible. This method has applications in the field of hemodynamic BCIs, and neuro-rehabilitation.

SYNOPSIS

INTRODUCTION

Studying the brain: a historical perspective

The exact physiological seat of the human mind was the subject of great mystery and debate throughout the roughly 200,000-year old history of the human species, with even Aristotle and Plato disagreeing on the matter (Finger, 2001). The first nomination of the brain being the seat of consciousness is believed to come from the father of western medicine, Hippocrates sometime in the 4th century BC. Not only did he argue that the brain is the center of perception (given its proximity to most sensory organs like the eyes, ears, tongue and nose), but went on to claim that it is also the seat of our venerated intelligence. During the early Islamic and European ages of enlightenment, anecdotal evidence was obtained from the observation that injuries to the head and brain lead to deficits in cognitive functions, and an array of medical problems associated with the brain were also identified, and an array of experiments demonstrated that perception arises in the brain (ref missing).

However, it was the first half of the 19th century that saw an enormous explosion in the study of the brain. Camillo Golgi's technique to stain cells and observe them under the microscope (leading to the identification of neurons) along with Luigi Galvani's demonstration of the electrical properties of neurons and muscles seeded two

intimate yet distinct questions involving the study of the brain: *what* is it made of and *how* does it function, giving birth to the subfields of neuroanatomy and neurophysiology respectively. Neuroanatomy aimed to study the structure of the brain, the kinds of cells it was composed of, their relative number, and the ways they were connected to one another. Neurophysiology, the study of *how* the brain functions, relied on studying the activity of neurons (in isolation or aggregation) in both health and disease.

The seminal work of Galvani, demonstrating a relationship between electrical activity and animal physiology (later termed electrophysiology) ensured that electrical activity remained the sole neurophysiological signal employed in the study of brain function for the better part of a century and half. Most of these studies were conducted on animals, where it was possible to record either from inside, or in close proximity to the brain, by surgically removing the scalp or skull. Human studies, however, were mostly limited to electrical recordings from the surface of the scalp, termed **E**lectro-**E**ncephalo**G**raphy (EEG; Hans Berger 1929), where the quality of the signals was poor. This tool, although extensively used, was limited in the spatial specificity it provided, as it recorded the average electrical activity from a very large population of neurons. In contrast, primate electrophysiology enabled recordings from inside the awake, behaving primate brain enabling the investigation of the response of single neurons in specific brain areas during a multitude of behavioral tasks.

Apart from sparse recordings from within the brains of patients with neurological conditions (such as epilepsy, Parkinson's disease, cancer in the CNS, etc.), the inability to obtain signals from deeper brain areas in human neurophysiology experiments lead to a large gap between invasive primate studies and non-invasive human EEG recordings. A tool capable of recording activity from the entire brain, with enough spatial resolution to discriminate between different areas of the brain was needed.

Interestingly, there was another candidate signal that began to capture researcher's interest in the 1990s: functional magnetic resonance imaging (fMRI), which measures the changes in the oxygenation of brain tissue (hemodynamic changes) and is frequently used (albeit with debatable assumptions) as a proxy for changes in underlying neuronal activity. FMRI became the single most used technique for studying human cognition by the turn of the 21st century, and the rate of publication rose at an astronomical rate. In 2015 alone, there were approximate 30,000 publications with fMRI vs 6,000 for EEG, a ratio of 5:1. FMRI enabled the recording of activity of the entire brain in action, albeit at a lower temporal resolution, enabling the estimation of which brain areas are involved in different tasks, and to what extent.

What is the hemodynamic signal?

In 1890, Charles Roy and Charles Sherrington first experimentally linked brain function to its blood flow, at Cambridge University in the UK. The next step to resolving how to measure blood flow in the brain was Linus Pauling's and Charles Coryell's discovery in 1936 that oxygen-rich blood with HbO was weakly repelled by magnetic fields, while oxygen-depleted blood with HbR was attracted to a magnetic field, though less so than ferromagnetic elements such as iron. Seiji Ogawa at AT&T Bell labs recognized that this could be used to augment MRI, which could study just the static structure of the brain, since the differing magnetic properties of HbR and HbO caused by blood flow to activated brain regions would cause measurable changes in the MRI signal. In a seminal 1990 study based on earlier work by Thulborn et al., Ogawa and colleagues scanned rodents in a strong magnetic field (7.0 T) MRI. To manipulate blood oxygen level, they changed the proportion of oxygen the animals breathed. As this proportion fell, a map of blood flow in the brain was seen in the MRI. They verified this

by placing test tubes with oxygenated or deoxygenated blood and creating separate images. To show these blood flow changes were related to functional brain activity, they changed the composition of the air breathed by rats, and scanned them while monitoring brain activity with EEG.

Three studies in 1992 were the first to explore using the BOLD contrast in humans. Kenneth Kwong and colleagues, used a gradient-echo Echo Planar Imaging (EPI) sequence at a magnetic field strength of 1.5 T to study activation in the visual cortex. Bandettini and colleagues used EPI at 1.5 T to show activation in the primary motor cortex, a brain area at the last stage of the circuitry controlling voluntary movements. The magnetic fields, pulse sequences and procedures and techniques used by these early studies are still used in current-day fMRI studies.

Like every physiological process in the body, neuronal activity also consumes metabolic energy. This metabolic activity causes a depletion of oxygenation in the neurons and their surrounding tissue. To replenish the oxygen, more blood flows into that volume of tissue from the arteries, carrying oxygen saturated hemoglobin molecules in red blood cells. This influx of blood leads to an increase in both the blood volume and oxygenated hemoglobin. The blood-flow change is localized to within 2 or 3 mm of where the neural activity is. Usually the incoming oxygen is more than the oxygen consumed by the neuronal tissue, and this causes a net decrease in deoxygenated hemoglobin (dHb) in that brain area's blood vessels. Together, these changes in blood-oxygenation and blood-volume are referred to as the hemodynamic signal, and the measurement of these signals across the entire brain (or parts of it) is termed functional neuroimaging. Functional neuroimaging has become the cornerstone of modern cognitive neurosciences.

However, it must be remembered that the hemodynamic signal is only an indirect measure of neuronal activity that is most often acquired without any concomitant

electrophysiological measurements. Hence, one of the biggest challenges is to understand the relationship of different kinds of neuronal activity (such as changes in neuronal excitation or inhibition) and their corresponding hemodynamic signals so as to better interpret the changes in the hemodynamic signals observed during such functional neuroimaging studies.

The question of how the hemodynamic signal relates to the underlying changes in neuronal activity is the major motivation behind this work, with the first four chapters being dedicated to the study of neurovascular coupling. The fifth chapter explores the feasibility of using hemodynamic signals (acquired using fNIRS) for detecting imagined movements, and using machine learning techniques to construct models that can learn to discriminate between different brain states, and are powerful enough to generalize over new subjects (a hitherto unchartered territory in fNIRS BCIs).

STUDY HYPOTHESIS AND OBJECTIVES

Study 1: Simultaneous epidural functional near-infrared spectroscopy and cortical electrophysiology as a tool for studying local neurovascular coupling in primates.

1. We aimed at testing (a) the feasibility of using fNIRS for recording cortical hemodynamic changes from the dura, and (b) the feasibility of combining this technique with intra-cortical electrophysiology using tetrodes. We hypothesised that compared to the usual placement of optodes on the surface of the scalp, where cortical hemodynamic signals are contaminated by artefacts arising from hemodynamic changes within the scalp, optodes placed on the dura will lead to a much better signal to noise ratio, while also ensuring that the dura is not compromised, increasing the risk of infection.
2. We aimed at comparing the signal to noise ratio of recordings from epidural fNIRS between two placements of detectors: a "near" detector, placed 6mm away from the emitter, and a "far" detector, placed 12mm from the emitter.

3. We also aimed at determining whether microelectrode recordings will be affected by pulses of near-infrared light leading to photo-electric effect based artefacts in the acquisition of neuro-electric signals.

Study 2: The timing of hemodynamic changes reliably reflects spiking activity.

1. The primary objective of this study was to understand the nature of the relationship between changes in blood oxygenation and volume, and the neuronal activity measured by intra-cortical electrophysiology.
2. We also aimed at testing the feasibility of using features in the hemodynamic response (such as peak-amplitude, peak-time, etc) and electrophysiological recordings (such as peaks in spiking or various bands of the LFP instead of using the more common method of correlating the time series of these signals.
3. Based on this method, we aimed at finding the best feature-to-feature correlation that would enable better interpretation of hemodynamic changes than is currently possible.

Study 3: The hemodynamic initial-dip consists of both volumetric and oxymetric changes correlated to localized spiking activity.

1. In this study, our primary objective was to better understand the neuronal correlates of the elusive initial-dip observed in various neuroimaging studies.
2. This study also aimed at proposing an alternative explanation to how the initial-dip arises by trying to elucidate its vascular mechanisms.

Study 4: Real-Time Subject-Independent Pattern Classification of Overt and Covert Movements from fNIRS Signals.

1. In this study we aimed to determine the feasibility of using fNIRS to classify left versus right hand motor cortical activations using support-vector machine (SVM) based classification. There were three sub-objectives to the study:
    a. To determine if an SVM could be trained on motor-execution (the performance of a motor task), and how efficiently it could classify motor-imagery (the imagination of performing a motor task without any physical movement).
    b. To determine if an SVM could be trained on motor-imagery and used for classification of motor-execution.
    c. To determine if a subject-independent classifier could be developed, capable of classifying motor execution and imagery from completely new subjects. We believed this last objective had deep applications in brain-state classification and neurofeedback using fNIRS where a trained SVM could be generalized.

RESULTS AND DISCUSSION

Simultaneous measurements of intra-cortical electrophysiology and functional neuroimaging are essential for relating the vast array of human neuroimaging studies with the extensive body of primate electrophysiology, which is unlikely to be obtained by using either technique in isolation (Logothetis et al., 2001). Such measurements in primates have previously been performed by combining cortical electrophysiology either with fMRI (Goense and Logothetis, 2008; Pauls et al., 2001) or Intrinsic Signal Optical Imaging (ISOI) (Cardoso et al., 2012; Sirotin and Das, 2009). Using fMRI one can obtain a 3D map of the hemodynamic activations in the brain, albeit at a low sampling rate (~1 Hz). The challenges for combining fMRI with cortical electrophysiology include interference compensation and correction of the gradient noise, apart from the relatively large monetary investment. ISOI has the advantage of both high spatial resolution and high sampling rate of hemodynamic signals above a region of cortex. However, in order to perform ISOI on primates, the dura above the region of interest (ROI) needs to be removed, sometimes being replaced by a transparent silicone membrane. This perturbation of the dura is a potential source of infection. Combining ISOI with electrophysiology is also a challenge, as the electrode drive can be a hindrance to the imaging, significantly reducing the number of electrodes

that can be used in tandem (Sirotin and Das, 2009). A less explored, and far less expensive approach for measurement of hemodynamic signals in primates is functional Near-Infrared Spectroscopy (fNIRS).

FNIRS is a non-invasive neuroimaging method that uses a near-infrared light source and detector pair (optode pair), to measure changes in concentrations of oxy-hemoglobin (HbO), deoxy-hemoglobin (HbR) and total hemoglobin (HbT), in a small volume of tissue (Ferrari and Quaresima, 2012). The advantages of fNIRS include its portability, metabolic specificity, high temporal resolution, high sensitivity in detecting small substance concentrations, affordability, and low susceptibility to movement artifacts (Kohl-Bareis et al., 2002; Villringer and Chance, 1997). Typically, fNIRS is measured from optodes fixed on the scalp, where it is subjected to spurious signals from hemoglobin concentration changes in the scalp tissue. The cortical hemodynamic signals are severely dampened by those originating from the scalp tissue, and most often the underlying cortical responses are only retrieved after rigorous signal averaging (Saager et al., 2011). One way to circumvent the problem is to record fNIRS signals from directly above the dura, after removing the scalp and bone. This would bring the optodes very close to the region of interest, with more infrared light illuminating the cortical tissue, eventually leading to a higher signal-to-noise ratio (SNR). Under these circumstances, fNIRS could be a very sensitive technique for hemodynamic measurements in primates, specifically to measure local neurovascular signals during electrophysiological recordings.

My work during my PhD focused on investigating the fNIRS signal in terms of its neural and vascular correlates, as well as its application in BCIs and neurofeedback. I began my work by developing and testing a novel method for acquiring fNIRS signals epidurally (section 3.1) from primates. I then aimed at understanding the neuronal correlates of the epidurally acquired fNIRS signals, and aimed at trying to unravel its

vascular origins (sections 3.2 and 3.3). Finally, I tried to assess the feasibility of using fNIRS for real-time pattern classification of cortical activations during movement execution and imagery, and aimed to demonstrate that it was possible to develop a multi-channel SVM based pattern classification algorithm that could classify activations new subjects, leading to the first successful demonstration of multi-channel subject-independent pattern classification from fNIRS signals (section 3.4). A brief description of these studies, their results and their significance follows below.

Simultaneous epidural fNIRS and intra-cortical electrophysiology

Traditionally fNIRS has always been acquired from the surface of the scalp (Ferrari and Quaresima, 2012). The vast majority of studies use an optode pair, with an emitter and detector placed perpendicular to the surface of the scalp, and separated by about 3cm to acquire hemodynamic signals from cortical tissue. The light from the emitter is refracted by biological tissue in all directions, and a small portion of the photons follow a banana-shaped path to reach the detector. Mathematical modeling of photon paths in the head have revealed that fNIRS has depth penetrance of about 1/3 to 1/2 of the separation of the optodes (Cui et al., 1991, 2011; Villringer, 1997). And hence for recording cortical hemodynamic changes that are around 1cm below the surface of the scalp, the optodes are placed 3cm away from each other. However, it was unclear whether this was true for optodes placed epidurally. Only a single study had reported the use of fNIRS epidurally in primates (Fuster et al., 2005), where the emitter and detector were placed 1cm apart.

To assess the optimal placement of optodes, we constructed a holder that housed three optodes placed linearly, 6mm apart from each other. We used one of the outer optodes as an emitter and the other two as detectors, generating two channels with an

inter-optode distance of 6 and 12 mm respectively. We also placed two rows of three tetrodes between each optode pair to record intra-cortical electrophysiology. This setup was lowered on to the monkey's dura above the visual cortex. We used a visual stimulation paradigm with a rotating chequerboard to stimulate the visual cortex in anesthetized monkeys, which was turned on for 5 seconds and turned off for 15, which constituted a single trial of our experiment. This paradigm was adapted from earlier work studying neurovascular coupling in the visual cortex of anesthetized primates (Logothetis et al., 2001).

We observed strong hemodynamic responses in the visual cortex on a trial-by-trial basis in both the HbO and HbR signals. Interestingly, the HbO responses in the 'near' channel were significantly higher than those of the 'far' channel, even though the far channel was supposed to detect hemodynamic changes from a larger volume of cortical tissue (based on the path of the photons). We observed that the PSDs of the HbO and HbR signals were more strongly modulated at 0.05 Hz (the frequency of the stimulation; 20s trial duration). We calculated the raw SNR of the HbO and HbR signals by dividing the signal power at 0.05 Hz by the entire PSD (between 0.01 and 10 Hz). Again, we obtained significantly higher SNRs for the 'near' emitter than the 'far' emitter for both HbO and HbR (see Table 1 and Figure 3A in Appendix 1). The mean SNR of the near emitter was 1078 for HbO and 1057 for HbR. We also observed a strong pulse artefact in the HbO signals at ~1.4 Hz, in the raw traces of HbO, which wasn't clearly observed in the HbR. The ability to resolve hemodynamic changes on a trial-by-trial basis, along with the pulse observed in the HbO signal, demonstrates the sensitivity of epidurally acquired fNIRS signals.

One concern of using near-infrared light along with microelectrode recordings was the generation of artefacts in the electrophysiology recordings arising from the photo-electric effect, which is commonly observed in two-photon imaging. However, we

observed no artefacts in the electrophysiological recordings at the sampling frequency of fNIRS (20Hz), demonstrating that the combination of the two methods enables simultaneous acquisition of these two signals without interference or interaction.

This demonstration of the feasibility and sensitivity of simultaneous fNIRS and intracortical electrophysiology opens new avenues for studying neurovascular coupling. In principle, all that is required for recording fNIRS is a photo-emitter and detector pair. The components to produce an optode pair are incredibly cheap and readily available from any hobby electronics store. Furthermore, the analysis of the signals acquired from fNIRS constitute a simple transformation of the absorbance of light from two wavelengths, which is neither computationally intensive nor algorithmically demanding. This means that the addition of epidural fNIRS to an already existing electrophysiology setup is incredibly simple, unlike the other techniques used to acquire hemodynamic changes for studying neurovascular coupling, such as fMRI or two-photon imaging, both of which require a significant monetary investment and expertise. The significance and advantages of this technique can be assessed from the following subsections.

However, this method suffers from one major limitation. Epidural fNIRS can only acquire signals from brain areas that are near the surface of the cortex, and is unable to record from deeper brain areas. Furthermore, the actual depth penetrance of epidural fNIRS is yet to be established.

The hemodynamic initial-dip consists of both volumetric and oxymetric changes correlated to localized spiking activity

Given the high SNR obtained from epidural fNIRS signals, we next aimed at understanding how the changes in blood oxygenation and volume correlate with neuronal activity. Earlier studies had demonstrated that hemodynamic changes

correlate with neuronal activity (Logothetis et al., 2001), but it was difficult to associate hemodynamic changes with a specific kind of neuronal activity (Goense and Logothetis, 2008). Specifically, it was difficult to assess whether the hemodynamic changes observed arose from neuronal excitation or inhibition (Logothetis, 2008), making the interpretation of results from functional neuroimaging studies very difficult.

We sought determine whether our new technique could lead to novel insights into neurovascular coupling. Using the same experimental paradigm described in Section 3.1, we analyzed the relationships between hemodynamic and neuronal changes. Given the higher SNR from the 'near' channel, we only analyzed the data from that channel and from the electrode placed nearest to the emitter. We divided the extracellular field potential into eight frequency bands and obtained their respective band envelopes (see Appendix 2 results section for details). We also obtained multi-unit spiking activity by counting the number of spikes in 50ms bins and converting it into spike-rates. Instead of using time-series correlations, we used feature based correlations in our analysis. We identified four features in the hemodynamic response, namely peak-amplitude, peak-time, initial-dip peak amplitude and initial-dip peak-time. These features were then correlated with different features of the neuronal activity.

Surprisingly, we obtained a strong negative correlation between the hemodynamic peak amplitude and various features of spiking activity such as the peak spike-rate after stimulus onset, the mean spike-rate during stimulus presentation, etc. Instead, we observed a strong positive correlation with the peak-spike rate and the peak-time of the hemodynamic response. We also obtained strong correlations between the peak spike rate and both the peak-amplitude of the initial-dip as well as its peak time. However, the peak-time of the initial dip correlated the strongest with the total sum of spikes from the beginning of the trial up to the hemodynamic response peak time. We also assessed how the hemodynamic signal correlated with the various LFP bands. We correlated the peak-

amplitude of the various LFP bands with all four features of the hemodynamic signal and obtained significant correlations for the DeltaTheta (1-4 Hz) and Alpha (4-8 Hz) bands.

To ensure that these correlations weren't artefacts of our visual stimulation paradigm, we analyzed spontaneous activity acquired by closing the monkeys' eyes and covering them with thick gauze. We obtained strong correlations between the hemodynamic response peak-time and spiking activity, whereas the peak-amplitude of the hemodynamic response correlated well with bursts in the Alpha band.

Based on the analysis of both stimulus induced and spontaneous activity, we found that spiking correlates with the peak-time of the hemodynamic response and low-frequency LFPs with its peak-amplitude. Spiking and low-frequency LFPs seem to represent different neuronal processes, namely, neuronal output and synaptic processing respectively (Belitski et al., 2008). The ability to infer changes in spiking activity as well as low-frequency LFPs from hemodynamic changes represents a significant leap forward in the interpretation of neuroimaging signals, enabling the teasing apart of contributions from different kinds of neuronal processes. Interestingly, when we do time-series based correlations, we obtain results similar to other studies (Goense and Logothetis, 2008; Logothetis et al., 2001), where the gamma band correlates strongly with the hemodynamic signal. We also find spiking to be more spatially localized than low-frequency LFPs. Further analysis of the dependence of hemodynamic signals on the spatio-temporal spreads of neuronal activity suggest that differences in the spatial spread of spiking and low-frequency LFPs across cortical surface influence different parameters of the hemodynamic response. Together, these results demonstrate that the hemodynamic response-amplitude is a poor correlate of spiking activity. Instead, we demonstrate that the timing of the initial-dip and the hemodynamic response are much more reliable correlates of spiking, reflecting bursts in spike-rate and

total spike-counts respectively. This demonstrates that a feature based approach for studying neurovascular coupling can lead to deeper insights into the nature of these relationships. These results represent the first ever report of independently inferring spiking activity and low-frequency LFPs from hemodynamic responses, and hence a significant leap forward in the interpretation of neuroimaging signals. A major limitation of this study, however, is that it was performed in anesthetized monkeys, and although earlier reports have suggested that the neurovascular coupling in anesthetized and awake preparations are similar, at least for fMRI (Goense and Logothetis, 2008), the true nature of the similarity or differences is subject to speculation and debate.

The hemodynamic initial-dip consists of both volumetric and oxymetric changes correlated to localized spiking activity

In our previous study, we demonstrated that bursts in spike-rates are correlated with the initial-dip. In this study, we aimed at further exploring this phenomenon. The initial-dip is an elusive and transient dip in the hemodynamic signal that is sometimes observed immediately after stimulus onset, and is believed to arise from an increase in HbR signals caused by neuronal activity. However, both its origins and neuronal correlates are all but entirely unknown.

Surprisingly, within the three hemodynamic signals we recorded, namely HbO, HbR and HbT, we observed that the initial-dip was strongest in the HbT signals. We also observed that trials that had low-spiking activity elicited a very small initial-dip. Only trials with very strong bursts in spike-rates elicited a strong initial-dip. Also, only the high-frequency LFPs correlated with the initial-dip, with spiking activity still eliciting the strongest coupling. We also observed a biphasic response in the HbR, with an early dip and a later rebound. We also observed similar results in the analysis of

spontaneous activity, demonstrating that these results are independent of our visual stimulation paradigm.

Based on our results as well as those from other studies, we hypothesize that the initial-dip is a vascular phenomenon that arises as a consequence of active venule dilation. This dilation leads to a sudden decrease in the capillary pressure causing them to flush out the blood into the veins. We also show that the HbT dip ensures that HbR concentration in the capillaries remains more or less constant, ensuring that larger increases in HbR concentration are compensated by larger HbT dips. This suggests that the initial-dip counteracts the rising HbR concentration in the capillaries. This study unveils the reasons behind the elusive nature of the initial-dip while also aiming at elucidating its vascular origins, by suggesting a new mechanism that might cause it. Furthermore, this represents the first report of a unique correlate of bursts in highly localized spiking activity in the hemodynamic signal. A major limitation of this study, however, is that using fNIRS we cannot segregate the contributions of HbO, HbR and HbT responses from the various vascular compartments, which meant that we could not provide definite evidence for our proposed mechanism of the initial-dip.

Real-Time Subject-Independent Pattern Classification of Overt and Covert Movements from fNIRS Signals

Unlike the previous studies that aimed at elucidating the neurovascular origins of hemodynamic signals using fNIRS, this study aimed at testing the feasibility of using fNIRS for classification of brain states. We demonstrated that multichannel fNIRS could be used to classify left versus right hand movement imagery and movement execution.

The purpose of the present study was to develop and test a real-time method for subject-specific and subject-independent classification of multi-channel fNIRS signals

using support-vector machines (SVM), so as to determine its feasibility as an online neurofeedback system. Towards this goal, we used left versus right hand movement execution and movement imagery as study paradigms in a series of experiments. In the first two experiments, activations in the motor cortex during movement execution and movement imagery were used to develop subject-dependent models that obtained high classification accuracies thereby indicating the robustness of our classification method. In the third experiment, a generalized classifier-model was developed from the first two experimental data, which was then applied for subject-independent neurofeedback training. Application of this method in new participants showed mean classification accuracy of 63% for movement imagery tasks and 80% for movement execution tasks. These results, along with their corresponding offline analysis reported in this study demonstrate that SVM based real-time subject-independent classification of fNIRS signals is possible.

The results obtained in our experiments suggest the applicability of our technique for neurofeedback experiments. However, the system is still open to modifications in areas such as robustness, usability etc. Even though the performance of the subject independent classifier is as good as the subject-dependent paradigm, it can still be optimized by incorporating head size, shape and activation pattern information from the individual subjects involved. This method has important applications in the field of hemodynamic BCIs, and neuro-rehabilitation where patients can be trained to learn spatio-temporal patterns of healthy brain activity (Sitaram et al., 2016, 2011).

When considering hemodynamic signals, the only other work for real-time subject-independent classification of brain states was done in fMRI (Sitaram et al., 2011). However, MRIs have a significant limitation in being uncomfortable, non-portable, loud and highly susceptible to movement artefacts. FNIRS has advantages in all these domains, and is also available at a fraction of the costs of an MRI machine. Furthermore,

the demonstration of subject-independent pattern classification demonstrate that the system can be used on completely new subjects. This has applications in neurofeedback, where a classifier can be trained on "healthy" brain activity, and then patients can be trained to emulate those spatio-temporal patterns.

Conclusions and future work

These studies aim at addressing different aspects of fNIRS, from testing the feasibility of acquiring it epidurally, to combining it with intracortical electrophysiology, to investigating its neuronal and vascular correlates, and finally to test its feasibility in subject-independent brain-state classification.

In the first study we demonstrate that fNIRS, when acquired epidurally, has a very high SNR, and when combined with intracortical electrophysiology, makes a powerful tool for studying neurovascular coupling. Future experiments would aim at optimizing the positioning of the optodes relative to each other, and also at investigating the use of optodes consisting of optical fibers that penetrate into the brain to record from deeper brain areas such as the hippocampus or thalamus. Such a technique, when combined with electrophysiology would enable the investigation of local neurovascular coupling in deeper brain areas with a much higher spatial and temporal resolution than is currently possible.

The demonstration of fNIRS as a candidate for real-time online classification of brain states also lead to its implementation for a study that attempted to communicate with completely locked-in patients suffering from Amyotrophic Lateral Sclerosis (ALS) (Chaudhary et al., 2017). The authors were capable of classifying "yes" versus "no" responses from completely locked in patients using fNIRS signals, but not from EEG

signals. This study represents a breakthrough in communication with ALS patients that are completely locked in.

For other human applications, a wireless, completely implantable fNIRS system would have applications in the domains of epilepsy monitoring, sleep monitoring, stroke recovery monitoring and neurofeedback. Whereas neuro-electric signals don't improve much when recorded from under the scalp, fNIRS signals show a vast improvement in their SNR. Coupled with the knowledge gained from our studies on the neurovascular correlates of the fNIRS signals, this technique could revolutionize minimally invasive implants for seizure forecasting and stroke rehabilitation, and would improve the accuracy of fNIRS based BCIs for communication and rehabilitation.

References

Belitski, A., Gretton, A., Magri, C., Murayama, Y., Montemurro, M. a, Logothetis, N.K., Panzeri, S., 2008. Low-frequency local field potentials and spikes in primary visual cortex convey independent visual information. J. Neurosci. 28, 5696–5709. https://doi.org/10.1523/JNEUROSCI.0009-08.2008

Chaudhary, U., Xia, B., Silvoni, S., Cohen, L.G., Birbaumer, N., Zee, P. van der, 2017. Brain–Computer Interface–Based Communication in the Completely Locked-In State. PLOS Biol. 15, e1002593. https://doi.org/10.1371/journal.pbio.1002593

Cui, W., Kumar, C., Chance, B., 1991. Experimental study of migration depth for the photons measured at sample surface. Proc. SPIE 1431, 180–191. https://doi.org/10.1117/12.44189

Cui, X., Bray, S., Bryant, D.M., Glover, G.H., Reiss, A.L., 2011. A quantitative comparison of NIRS and fMRI across multiple cognitive tasks. Neuroimage 54, 2808–2821. https://doi.org/10.1016/j.neuroimage.2010.10.069

Ferrari, M., Quaresima, V., 2012. A brief review on the history of human functional near-infrared spectroscopy (fNIRS) development and fields of application. Neuroimage 63, 921–935. https://doi.org/10.1016/j.neuroimage.2012.03.049

Finger, S., 2001. Origins of Neuroscience - A History of Explorations Into Brain Function, A History of Explorations Into Brain Function. https://doi.org/10.1002/ana.410360532

Fuster, J., Guiou, M., Ardestani, A., Cannestra, A., Sheth, S., Zhou, Y. Di, Toga, A., Bodner, M., 2005. Near-infrared spectroscopy (NIRS) in cognitive neuroscience of the primate brain. Neuroimage 26, 215–220. https://doi.org/10.1016/j.neuroimage.2005.01.055

Goense, J.B.M., Logothetis, N.K., 2008. Neurophysiology of the BOLD fMRI Signal in Awake Monkeys. Curr. Biol. 18, 631–640. https://doi.org/10.1016/j.cub.2008.03.054

Logothetis, N.K., 2008. What we can do and what we cannot do with fMRI. Nature 453, 869–878. https://doi.org/10.1038/nature06976

Logothetis, N.K., Pauls, J., Augath, M., Trinath, T., Oeltermann, a, 2001. Neurophysiological investigation of the basis of the fMRI signal. Nature 412, 150–157. https://doi.org/10.1038/35084005

Sitaram, R., Lee, S., Ruiz, S., Rana, M., Veit, R., Birbaumer, N., 2011. Real-time support vector classification and feedback of multiple emotional brain states. Neuroimage 56, 753–765. https://doi.org/10.1016/j.neuroimage.2010.08.007

Sitaram, R., Ros, T., Stoeckel, L.E., Haller, S., Scharnowski, F., Lewis-Peacock, J., Weiskopf, N., Blefari, M., Rana, M., Oblak, E., Birbaumer, N., Sulzer, J., 2016. Closed-loop brain training: the science of neurofeedback. Nat. Neurosci.

https://doi.org/10.1038/nrn.2016.164
Villringer, A., 1997. Non-invasive optical spectroscopy and imaging of human brain function. Trends Neurosci. 20, 435–442. https://doi.org/10.1016/S0166-2236(97)01132-6

PERSONAL CONTRIBUTIONS TO PAPERS AND MANUSCRIPTS

Simultaneous epidural functional near-infrared spectroscopy and cortical electrophysiology as a tool for studying local neurovascular coupling in primates

Ali Danish Zaidi: Study design, data acquisition, data analysis, manuscript preparation

Matthias Munk: Study implementation, data acquisition

Andreas Schmidt: Data acquisition

Cristina Risueno-Segovia: Data acquisition

Rebekka Bernard: Data acquisition

Eberhard Fetz: Study design, interpretation of results, manuscript revision

Nikos Logothetis: Study implementation, data acquisition, interpretation of results, manuscript revision

Niels Birbaumer: Study design, interpretation of results, manuscript revision

Ranganatha Sitaram: Study design, data acquisition, interpretation of results, manuscript revision

The timing of hemodynamic changes reliably reflects spiking activity

Ali Danish Zaidi: Study design, data acquisition, data analysis, manuscript preparation

Niels Birbaumer: Study design, interpretation of results, manuscript revision

Eberhard Fetz: Study design, interpretation of results, manuscript revision

Nikos Logothetis: Study implementation, data acquisition, interpretation of results, manuscript revision

Ranganatha Sitaram: Study design, data acquisition, interpretation of results, manuscript revision

The hemodynamic initial-dip consists of both volumetric and oxymetric changes correlated to localized spiking activity.

Ali Danish Zaidi: Study design, data acquisition, data analysis, manuscript preparation

Niels Birbaumer: Study design, interpretation of results, manuscript revision

Eberhard Fetz: Study design, interpretation of results, manuscript revision

Nikos Logothetis: Study implementation, data acquisition, interpretation of results, manuscript revision

Ranganatha Sitaram: Study design, data acquisition, interpretation of results, manuscript revision

Real-Time Subject-Independent Pattern Classification of Overt and Covert Movements from fNIRS Signals

Neethu Robinson*: Study design, data acquisition, data analysis, manuscript preparation

Ali Danish Zaidi*: Study design, data acquisition, data analysis, manuscript preparation

Mohit Rana: Study design, data acquisition, manuscript revision

Vinod A. Prasad: Interpretation of results, manuscript revision

Cuntai Guan: Interpretation of results, manuscript revision

Niels Birbaumer: Study design, interpretation of results, manuscript revision

Ranganatha Sitaram: Study design, data acquisition, data analysis, manuscript revision

* These authors contributed equally to this work

Appendix: Papers and Manuscripts

Appendix 1: Simultaneous epidural functional near-infrared spectroscopy and cortical electrophysiology as a tool for studying local neurovascular coupling in primates

NeuroImage 120 (2015) 394–399

Contents lists available at ScienceDirect

NeuroImage

journal homepage: www.elsevier.com/locate/ynimg

Simultaneous epidural functional near-infrared spectroscopy and cortical electrophysiology as a tool for studying local neurovascular coupling in primates

Ali Danish Zaidi [a,b,*], Matthias H.J. Munk [a,c], Andreas Schmidt [a,b], Cristina Risueno-Segovia [a], Rebekka Bernard [a], Eberhard Fetz [d], Nikos Logothetis [a,e], Niels Birbaumer [b,f,g], Ranganatha Sitaram [b,h,**]

[a] Max Planck Institute for Biological Cybernetics, Tübingen, Germany
[b] Institute for Medical Psychology and Behavioral Neurobiology, University of Tübingen, Germany
[c] Systems Neurophysiology, Fachbereich Biologie, Technische Universität Darmstadt, Germany
[d] Department of Physiology and Biophysics and Washington National Primate Research Center, University of WA, Seattle, USA
[e] Center for Imaging Sciences, Biomedical Imaging Institute, University of Manchester, UK
[f] Ospedale San Camillo, Istituto di Ricovero e Cura a Carattere Scientifico, Venezia-Lido, Italy
[g] Department of Psychology, Biological Psychology, Universidad de las Islas Baleares, Spain
[h] Department of Biomedical Engineering, University of Florida, Gainesville, FL, USA

ARTICLE INFO

Article history:
Received 23 April 2015
Accepted 7 July 2015
Available online 11 July 2015

ABSTRACT

Simultaneous measurements of intra-cortical electrophysiology and hemodynamic signals in primates are essential for relating human neuroimaging studies with intra-cortical electrophysiology in monkeys. Previously, technically challenging and resourcefully demanding techniques such as fMRI and intrinsic-signal optical imaging have been used for such studies. Functional near-infrared spectroscopy is a relatively less cumbersome neuroimaging method that uses near-infrared light to detect small changes in concentrations of oxy-hemoglobin (HbO), deoxy-hemoglobin (HbR) and total hemoglobin (HbT) in a volume of tissue with high specificity and temporal resolution. FNIRS is thus a good candidate for hemodynamic measurements in primates to acquire local hemodynamic signals during electrophysiological recordings. To test the feasibility of using epidural fNIRS with concomitant extracellular electrophysiology, we recorded neuronal and hemodynamic activity from the primary visual cortex of two anesthetized monkeys during visual stimulation. We recorded fNIRS epidurally, using one emitter and two detectors. We performed simultaneous cortical electrophysiology using tetrodes placed between the fNIRS sensors. We observed robust and reliable responses to the visual stimulation in both [HbO] and [HbR] signals, and quantified the signal-to-noise ratio of the epidurally measured signals. We also observed a positive correlation between stimulus-induced modulation of [HbO] and [HbR] signals and strength of neural modulation. Briefly, our results show that epidural fNIRS detects single-trial responses to visual stimuli on a trial-by-trial basis, and when coupled with cortical electrophysiology, is a promising tool for studying local hemodynamic signals and neurovascular coupling.

Introduction

Simultaneous measurements of intra-cortical electrophysiology and functional neuroimaging are essential for relating the vast array of human neuroimaging studies with the extensive body of primate electrophysiology, which is unlikely to be obtained by using either technique in isolation (Logothetis et al., 2001). Such measurements in primates have previously been performed by combining cortical electrophysiology either with fMRI (Goense and Logothetis, 2008; Logothetis et al., 2001) or intrinsic signal optical imaging (ISOI) (Cardoso et al., 2012; Sirotin and Das, 2009). Using fMRI, one can obtain a 3D map of the hemodynamic activations in the brain, albeit at a low sampling rate (~1 Hz). The challenges for combining fMRI with cortical electrophysiology include interference compensation and correction of the gradient noise, apart from the relatively large monetary investment. ISOI has the advantage of both high spatial resolution and high sampling rate of hemodynamic signals above a region of the cortex. However, in order to perform ISOI on primates, the dura above the region of interest (ROI) needs to be removed, sometimes being replaced by a transparent silicone membrane.

Abbreviations: ECoG, Electrocorticogram; fMRI, Functional magnetic resonance imaging; fNIRS, Functional near-infrared spectroscopy; HbO, Oxygenated hemoglobin; HbR, Deoxygenated hemoglobin; ISOI, Intrinsic-signal optimal imaging; MI, Neural modulation index; MUA, Multi-unit activity; PSD, Power spectral density; SNR, Signal-to-noise ratio; TTL, Transistor–transistor logic.

* Correspondence to: Max Planck Institute for Biological Cybernetics, Spemannstrasse 38, Tübingen, Germany.
** Correspondence to: Institute of Biological and Medical Engineering, and Department of Psychiatry in the Section of Neuroscience, Pontificia Universidad Católica de Chile, Santiago, Chile.
E-mail addresses: azaidi@tue.mpg.de (A.D. Zaidi), ranganatha.sitaram@bme.ufl.edu (R. Sitaram).

http://dx.doi.org/10.1016/j.neuroimage.2015.07.019
1053-8119/

This perturbation of the dura is a potential source of infection. Combining ISOI with electrophysiology is also a challenge, as the electrode drive can be a hindrance to the imaging, significantly reducing the number of electrodes that can be used in tandem (Sirotin and Das, 2009). A less explored, and far less expensive approach for measurement of hemodynamic signals in primates is functional near-infrared spectroscopy (fNIRS).

FNIRS is a non-invasive neuroimaging method that uses a near-infrared light source and detector pair (optode pair), to measure changes in concentrations of oxy-hemoglobin (HbO), deoxy-hemoglobin (HbR) and total hemoglobin (HbT) in a small volume of tissue (Ferrari and Quaresima, 2012). The advantages of fNIRS include its portability, metabolic specificity, high temporal resolution, high sensitivity in detecting small substance concentrations, affordability and low susceptibility to movement artifacts (Kohl-Bareis et al., 2002; Villringer and Chance, 1997). Typically, fNIRS is measured from optodes fixed on the scalp, where it is subjected to spurious signals from hemoglobin concentration changes in the scalp tissue. The cortical hemodynamic signals are severely dampened by those originating from the scalp tissue, and most often the underlying cortical responses are only retrieved after rigorous signal averaging (Saager et al., 2011). One way to circumvent the problem is to record fNIRS signals from directly above the dura, after removing the scalp and bone. This would bring the optodes very close to the region of interest, with more infrared light illuminating the cortical tissue, eventually leading to a higher signal-to-noise ratio (SNR). Under these circumstances, fNIRS could be a very sensitive technique for hemodynamic measurements in primates, specifically to measure local neurovascular signals during electrophysiological recordings.

In this study, we tested the sensitivity of epidural fNIRS and the feasibility of combining epidural fNIRS with recordings from microelectrodes in neocortex. We recorded hemodynamic and neuronal activity from the primary visual cortex in two anesthetized monkeys during visual stimulation. We developed a plastic chamber inset that housed optodes and guide tubes arranged in a linear fashion (Fig. 1A) to enable us to position the optodes and electrodes close to each other, and hence, record both types of signals simultaneously from a small volume of cortical tissue. We observed clear, strong trial-by-trial activations in the [HbO] and [HbR] signals that were correlated with the underlying cortical neural activation. These results demonstrate that epidurally measured fNIRS signals have high SNR, and when combined with cortical electrophysiology, provide a highly reliable and sensitive method for studying local neurovascular-coupling.

Methods

Surgery and craniotomy

Two healthy adult rhesus monkeys, M1 (female; 8 kg) and M2 (male; 10 kg), were used for experiments. Vital parameters were monitored during anesthesia. After sedation of the animals using ketamine (15 mg/kg), anesthesia was initiated with fentanyl (31 μg/kg), thiopental (5 mg/kg) and succinylcholine chloride (3 mg/kg), and then the animals were intubated and ventilated. A DatexOhmeda Avance (GE, USA) was used for ventilation, with respiration parameters adjusted to maintain an end-expiratory CO_2 of 4.0%. Anesthesia was maintained with remifentanil (0.5–3 μg/kg/min) and eye movements were prevented by mivacurium chloride (4–7 mg/kg/h). Depending on the blood pressure, an iso-osmotic solution (Jonosteril, Fresenius Kabi, Germany) or a plasma expander (Volulyte, Fresenius Kabi, Germany) was infused at a rate of ~10 (5–15) ml/kg/h. During the entire experiment, body temperature was carefully regulated between 38.5 °C and 39.5 °C, and SpO_2 was maintained above 95%. Under anesthesia, a small skin cut and craniotomy were made above the left hemisphere in order to access the primary visual cortex (V1). In all subsequent experiments, the bone opening was cleaned from connective tissue exposing the dura for insertion of microelectrodes. For each monkey, at least two weeks were allowed for recovery between successive experiments. All experiments were approved by the local authorities (Regierungspräsidium, Tübingen) and are in agreement with guidelines of the European Community for the care of laboratory animals.

Positioning of optodes and electrodes

To enable precise positioning of electrodes relative to the optodes, we developed a cylindrical plastic chamber inset (Fig. 1A) that rested on the skull of the monkey around the craniotomy. The bottom of the inset was molded to the curvature of the skull so that it fit snugly on the bone. The inset had three large vertical holes of 2.5 mm diameter each, spaced 6 mm apart, arranged linearly (Fig. 1B). These holes were used to hold the NIRS optodes. The optodes protruded approximately 5 mm from the lower surface of the plastic inset (Fig. 1A) so as to touch the dural surface. Out of these three optodes, one peripheral optode was used as an emitter and two optodes were used as detectors. The emitter–detector pair that was separated by 6 mm was called the 'near' channel, and the emitter detector pair separated by 12 mm was called the 'far' channel.

Between the optode holes, there were two rows of three smaller holes, linearly aligned, measuring 0.4 mm in diameter, for holding the guide tubes with tetrodes and/or single electrodes inside (Fig. 1B). Each of these holes was 1.2 mm apart from the other, and the two rows were separated by a distance of 1 mm from the center. The guide tubes also protruded approximately 5 mm from the lower surface of the inset. The inset, housing the optodes and electrodes was then lowered on to the craniotomy using a stereotactic manipulator. After correct positioning was confirmed, we began driving the electrodes into the cortex. During the recording, the most medial optode served as the emitter and the others served as detectors. Halfway into the

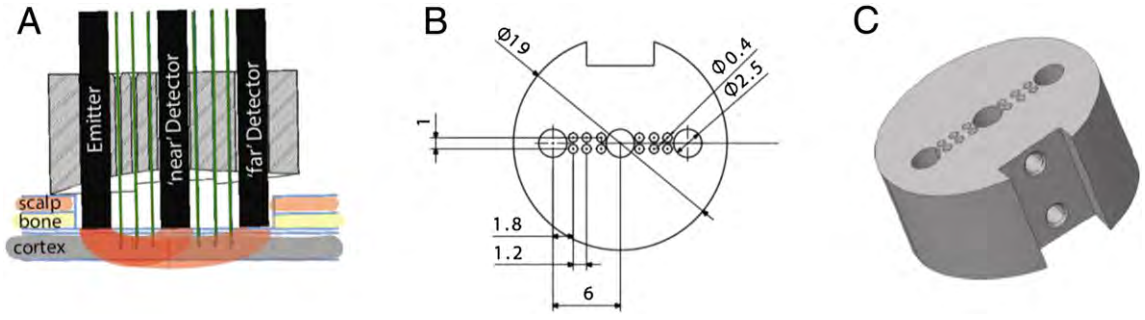

Fig. 1. Schematic representation of plastic inset with the optodes and electrodes in position. (A) Vertical section through the plastic inset showing the relative position of optodes (black cylinders) and tetrodes (green arrows pointing downwards). The scalp and bone were removed during surgery and the optodes were lowered on the dura. The guide tubes of the tetrodes also rested on the dura. The tetrodes were driven into the cortex. (B) A top-view of the plastic inset showing the relative positions of optodes and electrodes, and the diameters of the holes. The three large, central holes are for optodes and the twelve small holes between them are for guide tubes for holding and driving electrodes. The holes on the lower edge are for screws to help stabilize the fNIRS optodes. All values are in millimeters. (C) 3D rendering of the plastic inset with the holes for optodes and electrodes aligned linearly in the center. The two holes on the front face were used for screws to attach the inset to the Thomas Recording Matrix head.

session, the position of the emitter was exchanged, so that the most lateral optode became the emitter and the others become the detectors. The central optode was always used as the 'near' detector.

fNIRS measurement

For fNIRS measurements, we used a NIRScout machine (NIRx Medizintechnik GmbH, Berlin), which performs dual wavelength LED light-based spectroscopic measurements at 760 and 850 nm. Sampling was performed at 20 Hz. We used modified emitters and detectors, and optical fiber bundles for sending the light from the LED source into the tissue, and also for detecting refracted light from the tissue. Both the emitter and detector fiber bundles had iron ferrule tips with an aperture of 2.5 mm on the ends that touched the dura. The recording instrument was connected via USB to a laptop computer running an interactive software (NIRStar, NIRx Medizintechnik, GmbH, Germany) provided along with the instrument. The software was used for starting and stopping recordings, and also for setting up the various recording parameters, such as the number of sources and detectors, and the sampling rate. The instrument received TTL pulses from the stimulus system and the electrophysiological recording system for synchronization. The system sent 1-ms TTL pulses every 50 ms to the recording system that corresponded to light pulses. After correct positioning of optodes on to the dura, a gain calibration for the signal was performed.

Electrophysiology

We used custom-built tetrodes and electrodes. All tetrodes and single electrodes had impedance values less than 1 (range, 0.2–0.8) MΩ. The impedance of each channel was noted before loading the tetrodes onto the drive, and once again during unloading after the experiment, to ensure that all contacts were intact throughout the duration of the experiment. To drive the electrodes into the brain we used a 64-channel matrix (Thomas Recording GmbH, Giessen, Germany). The electrodes were loaded in guide tubes a day before the experiment. The output was connected to a speaker and an oscilloscope, with a switch to help cycle between different channels. We advanced electrodes into the cortex one by one until we heard a reliable population response to a rotating checkerboard flickering at 0.5 Hz, left the electrode to relax the tissue and checked tens of minutes later to see how stable the recording was.

Visual stimulation

A fundus camera was used to locate the fovea of each eye. For presenting visual stimulation, a fiber optic system (Avotec, Silent Vision, USA) was positioned in front of each eye, so as to be centered on the fovea. To adjust the plane of focus, contact lenses (hard PMMA lenses, Wöhlk, Kiel, Germany) were inserted to each eye. We used a whole-field, rotating checkerboard to drive the neural activity. The direction of rotation was reversed every second. Each trial consisted of 5 s of visual stimulation followed by 15 s of a dark screen. A single run consisted of 20 trials. Data presented are from 14 runs spread over 8 experimental days.

Data analysis

All analyses were performed in MATLAB using custom-written code. The runs that failed to elicit any significant modulation in the MUA band were excluded from the analysis. Also, only runs that cleared visual screening for artifacts were used.

fNIRS signal processing

The raw wavelength absorption data from the NIRS system were converted to concentration changes of [HbO] and [HbR] using a modified Beer–Lambert equation (Villringer and Chance, 1997). For correlating hemodynamic signals with neural activity, the signals were band-pass filtered between 0.01 and 5 Hz to remove low-frequency drifts and high-frequency noise. The major discernible sources of physiological noise in the NIRS signals are from respiration and pulse. The pulse artifact varies between 1.1 and 2 Hz, The respiration artifact, on the other hand, has a much higher power, and hence contributes more significantly to the variance of the signal. This artifact peaks at 0.1 or 0.09 Hz (corresponding to respiration cycles lasting 10 or 11 s). Although filtering the signal between 0.01 and 1 Hz would remove the pulse artifact, it would not remove the respiration artifact. The respiration artifact can only be removed either by filtering the signal below 0.09 Hz, or by using notch filters at 0.1 and 0.09 Hz. However, both of these procedures could also lead to a loss of information in the signal corresponding to other features, for example, the HbO initial dip (Fig. 2D).

Since the change in [HbR] was negative, the peak-amplitudes for [HbR] are thus also negative. For a trial-by-trial analysis, the hemodynamic response for each trial was zero-corrected by subtracting, from each hemodynamic response, the value at the start of the trial.

Calculation of SNR of hemodynamic signals

We obtained power spectral densities for the [HbO] and [HbR] signals for each run. To calculate the raw SNR, we divided the peak power with the mean power for each run.

Electrophysiological signal processing

The raw broadband signal was sampled at 20.8333 kHz. From the raw signal, the multiunit activity (MUA; 1000–3000 Hz) was filtered out. The envelope of the MUA was then obtained by taking the absolute value of the Hilbert transform of the filtered signal. The band-envelope was then converted to standard deviation units by subtracting the mean and dividing by the standard deviation of the signal. The modulation index (MI) for each trial was calculated using the formula $MI = (MUA_{On} - MUA_{Off})/(MUA_{On} + MUA_{Off})$; where MUA_{On} is the mean MUA activity during the On epoch and MUA_{Off} is the mean MUA power during the Off epoch for each trial.

Statistics

All significance values are based on Wilcoxon's signed rank test on the various distributions of hemodynamic and neuronal activity, such as [HbO] and [HbR] peak-amplitudes and peak-time, and the neural modulation index. Standard error of means is reported along with all mean values in the text. In the figures, the shaded regions represent 95% confidence intervals.

Results

Single trial responses in [HbO] and [HbR] in an example run

We observed reliable responses to visual stimulation manifested as changes in the concentrations of both HbO and HbR on a trial-by-trial basis. Fig. 2A shows the [HbO] and [HbR] signals for an example run. The mean value has been subtracted from each signal. As can be clearly seen, during each On epoch the [HbO] signal begins to rise after a small delay (~1 s). It peaks around 7 s, and then begins to fall again, returning to the baseline value. The [HbR] follows a similar time-course, albeit inverted. Although there is some variability in the peak-amplitudes of the [HbO] for each trial, the strong response to the visual stimulation for each trial shows the sensitivity of epidural fNIRS and its high SNR (see Section 3.2 for details on SNR). The [HbO] and [HbR] signals had larger peak-amplitude and lesser noise for the 'near' emitter–detector pair (6 mm distance) compared to the 'far' (12 mm distance) (Table 1; Fig. 3B), and hence data from only the 'near' pair are shown. A strong pulse artifact with a periodicity of ~1.4 Hz was also observed in the fNIRS signals as small but regular peaks in the [HbO] (Fig. 2C).

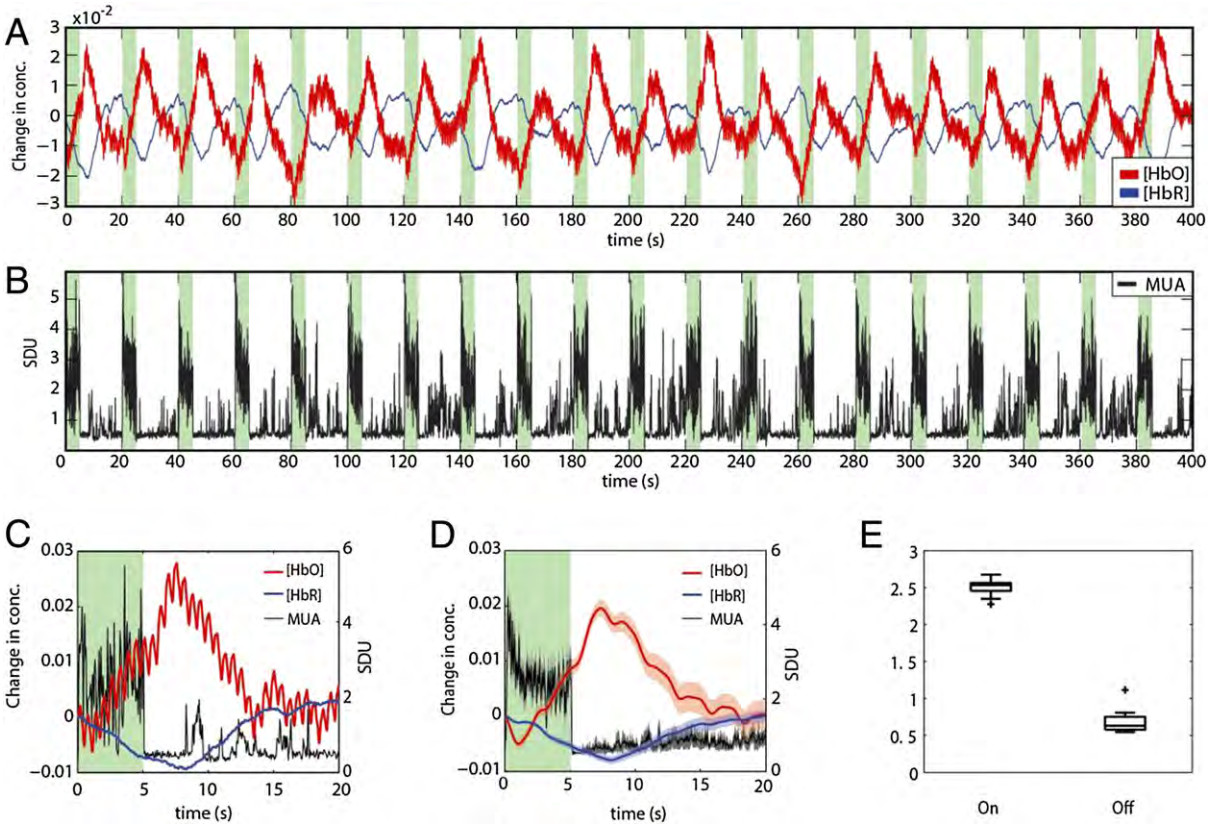

Fig. 2. Data from example run consisting of 20 trials. (A) Raw, unfiltered signals of changes in concentrations in HbO (red) and HbR (blue) from an example run. The On (green) and Off (white) epochs were 5 and 15 s, respectively, repeating 20 times. The *x*-axis represents time in seconds. The means have been subtracted from both signals. Strong trial-by-trial activations can be clearly observed in both signals. (B) Band-envelope of the MUA (1–3 kHz) signal for the same run as Fig. 1A. The signal was standardized by subtracting the mean and dividing by the standard deviation, and the minimum value was subtracted. The *y*-axis represents standard deviation units, the *x*-axis represents time in seconds. (C) The first 20 s of the [HbO], [HbR] and MUA signals plotted in A and B. The pulse artifact in the [HbO] signal is clearly visible. (D) The mean [HbO], [HbR] and MUA signals obtained after averaging the 20 trials in A and B. Each trial was zero-corrected (the value at the beginning of the trial was set to zero). The shaded regions represent 95% confidence intervals. (E) Distribution of mean MUA values during 20 On and Off epochs shown in B. The means of the two distributions are significantly different ($p < 10^{-8}$; Wilcoxon rank-sum test).

Fig. 2D shows the mean [HbO] and [HbR] signals over the 20 trials of the run. The shaded regions represent 95% confidence intervals.

Fig. 2B plots the MUA activity (in SDU) as a function of time for the same run, showing clear responses to the visual stimuli. The distribution of mean activity during each On and Off epoch is shown in Fig. 2E. The modulation index (MI) for each trial was calculated by obtaining the mean MUA activity during the On and Off epochs of each trial, and applying the formula $MI = (MUA_{On} - MUA_{Off})/(MUA_{On} + MUA_{Off})$; where MUA_{On} is the mean MUA activity during the On epoch and MUA_{Off} is the mean MUA power during the Off epoch. The median of the MI for the 20 trials was significantly greater than zero (mean MI for 20 trials is 0.6, $p < 10^{-4}$; Wilcoxon signed rank test).

Raw signal-to-noise ratio

We estimated the raw signal-to-noise ratio of [HbO] and [HbR] signals during visual stimulation. To calculate SNR, we obtained the power spectral density (PSD) for the [HbO] and [HbR] signals for each run. For every run, the peak in the PSD was around 0.05 Hz (0.0479 ± 0.0005), corresponding to the 20 s trial length (Fig. 3A shows the mean PSD for the 14 runs; data averaged over both monkeys). We refer to the peak-amplitude of the PSD corresponding to the visual modulation as P_{stim}. The 'near' P_{stim} was higher than the 'far' P_{stim} for both [HbO] and [HbR] signals ($p < 10^{-4}$; Wilcoxon signed rank test), showing that the signal modulation was higher in the 'near' channel than the 'far' channel. Also, the P_{stim} for [HbO] was larger than the P_{stim} for [HbR], for both 'near' and 'far' channels (Fig. 3A, thick versus thin traces).

To obtain the SNR for each run, we divided the P_{stim} by the mean power for that run. Table 1 summarizes the SNR distributions for all 14 runs. The mean SNRs for 'near' channel were larger than those from the 'far' channel for both [HbO] and [HbR] signals, but were not significantly different (based on Wilcoxon rank sum test). However, the mean HRF peak-amplitude for the 'near' channel was significantly larger than that for the 'far' channel for both [HbO] and [HbR] signals (Fig. 3B; $p < 10^{-3}$ for all trials over 14 runs; see Supplementary Figure 1 for comparison of 'near' and 'far' channels of a single trial).

The fact that the highest peak in the PSD corresponds to the periodicity of visual stimulation, combined with very high SNR for the signals demonstrates the sensitivity of epidurally measured fNIRS signals.

Table 1
Raw SNR values for [HbO] and [HbR] signals from the 'near' and 'far' channels.

Parameter	Mean	SEM	Significance*
'near' [HbO]	1078.1	76.4	$p < 10^{-3}$
'near' [HbR]	1057.7	93.7	$p < 10^{-3}$
'far' [HbO]	914.6	55.2	$p < 10^{-3}$
'far' [HbR]	889.2	57.7	$p < 10^{-3}$

* Based on the Wilcoxon signed rank test.

Hemodynamic responses to visual stimulation

Fig. 4A shows the distributions of peak-amplitude and peak-time for each trial for both [HbO] and [HbR] for both monkeys. The left panel represents the distribution of peak-amplitudes, and the right

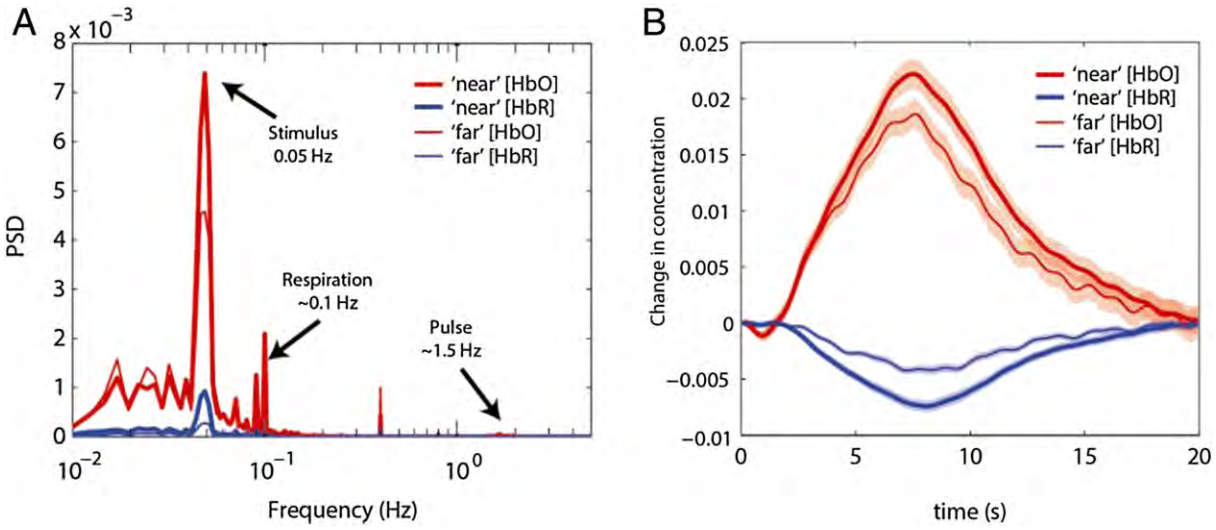

Fig. 3. PSD of [HbO] and [HbR] and corresponding SNR. The thick and thin traces correspond to the 'near' and 'far' channels, and the [HbO] and [HbR] traces are colored red and blue, respectively. (A) The mean power spectral density as a function of frequency. Mean of 14 runs from 2 monkeys. The strongest modulation is around 0.05 Hz, which corresponds to the frequency of visual simulation. Artifacts from respiration and pulse are also marked. (B) The mean HRF obtained by averaging overall trials from all runs for both monkeys. The peak-amplitudes in the 'near' channel are larger for those in the 'far' channel.

panel represents the distribution of peak-time. The [HbO] peak-amplitudes and peak-times for M1 and M2 are shown in Table 2. The absolute values of peak-amplitudes for [HbO] signals were larger than those for the [HbR] signals for both monkeys. Also, the time to peak for the [HbO] was sooner than the time to peak for the [HbR].

Correlations with neuronal activity

In order to determine how the fNIRS signals were related to underlying neuronal activity, we determined whether the [HbO] peak-time was correlated with the MUA MI (Fig. 4B). We obtained the average MI and peak-time for each run. There is a clear and significant correlation between the MI and [HbO] peak-time ($r = 0.65$; $p = 0.011$). A similar relationship was observed between MI and [HbR] ($r = 0.71$; $p = 0.004$). We found stronger correlations between [HbR] peak-time and MI, probably because the [HbR] is less susceptible to biological artifacts caused by breathing and the pulse, both of which are much more obvious in the [HbO] signals (Fig. 2C and 2D). We also found stronger correlations for [HbO] and [HbR] peak-time than the peak-amplitude (Supplementary Figure 2).

Discussion

Comparison with earlier studies

Epidural fNIRS has been acquired in rats (Crespi, 2007; Crespi et al., 2005) without, and in monkeys (Fuster et al., 2005) with combined electrophysiological recordings. The Crespi studies have shown that epidural fNIRS reliably represents tissue oxygenation changes, but neuronal activity was not recorded. Fuster et al. conducted a study combining epidural fNIRS with ECoG, but did not document the SNR of the fNIRS signals or their correlations with ECoG signals. A device for studying neurovascular coupling in humans based on intracranial acquisition of hemodynamic and neuronal signals has also been developed for diagnostic evaluation for surgical therapy in epilepsy patients (Keller et al., 2009). However, these studies do not quantify

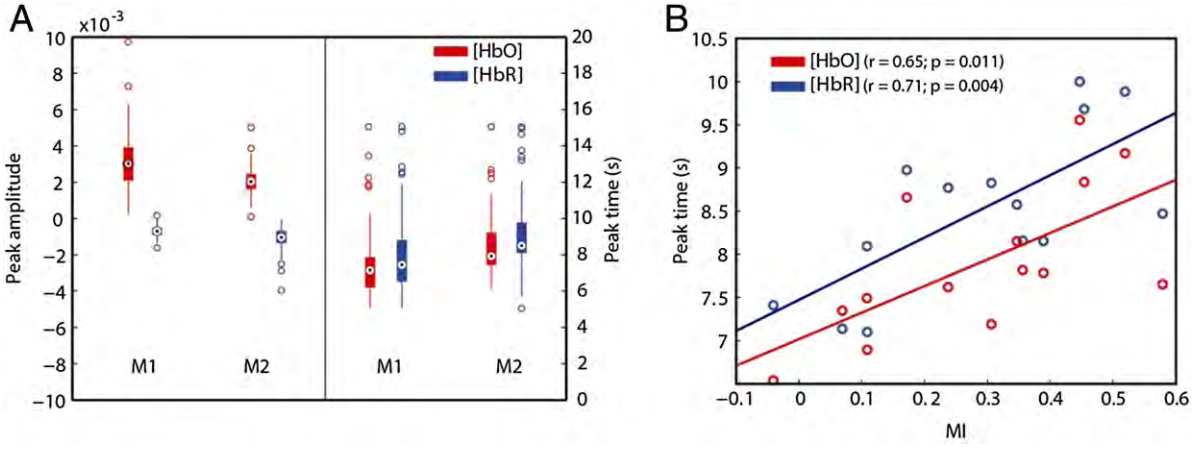

Fig. 4. Distribution of peak-amplitudes and peak-times for all sessions, and their neuronal correlates. (A) The distribution of the peak-amplitude (left panel) and peak-time (right panel) for both [HbO] and [HbR] for each monkey for each trial. For each boxplot, the circle with the black dot represents the median, the thick and thin lines represent the 67% and 95% confidence intervals, respectively, and the hollow circles represent the outliers. The data represent 280 trials recorded over 14 runs. For values refer to Table 1. (B) Neural modulation (MI; *x*-axis) versus the peak-time for the [HbO] and [HbR] (*y*-axis). There is a significant correlation between MI and [HbO] and [HbR] peak-time. Each data point is an average over the 20 trials for each run.

Table 2
Distribution of 'peak-amplitude' and 'peak-time' for [HbO] and [HbR] responses.

Monkey	Parameter	Mean	SEM	Significance*
M1	[HbO] peak-amplitude	0.0309	0.0014	$p < 10^{-20}$
	[HbO] peak-time	7.2842	0.1505	$p < 10^{-20}$
	[HbR] peak-amplitude	−0.0107	0.0005	$p < 10^{-20}$
	[HbR] peak-time	7.7767	0.1727	$p < 10^{-20}$
M2	[HbO] peak-amplitude	0.0206	0.0005	$p < 10^{-27}$
	[HbO] peak-time	8.3737	0.1115	$p < 10^{-27}$
	[HbR] peak-amplitude	−0.0071	0.0002	$p < 10^{-27}$
	[HbR] peak-time	9.0716	0.1282	$p < 10^{-27}$

* Based on Wilcoxon signed rank test.

the sensitivity of invasively acquired fNIRS signals, nor do they check for a relationship with the underlying neuronal activity. We performed simultaneous epidural fNIRS and cortical electrophysiological recordings in two anesthetized macaques during visual stimulation. We observed robust trial-by-trial activations represented as changes in [HbO], [HbR] and neuronal activity in both monkeys. The raw SNR for both [HbO] and [HbR] signals was very high, and the mean peak-time for the hemodynamic response for each run correlated significantly with the mean MUA modulation.

Correlations with neuronal activity

We found significant correlations between hemodynamic peak-time with the underlying neuronal modulations, but not for the peak-amplitude (see Supplementary Figure 1). One of the reasons could be the lack of dynamic range in the stimulus intensity, since we only used a high-contrast rotating checkerboard as a visual stimulus. This may lead to reduction in the dynamic range of the hemodynamic signal. However, on a trial-to-trial basis, the peak-amplitude may also be affected by other processes, for example, the trend of the signal before trial onset. If the oxygen concentration in the tissue is high, and close to saturation, the dynamic range of the signal might be reduced, and smaller peaks in the hemodynamic response might be observed. Instead, if the tissue oxygen concentration is low, the dynamic range of the hemodynamic signal could be high, leading to higher peaks. The slope of the signal before trial onset may influence the tissue saturation, and consequently, signal amplitude. If the signal trend affects the dynamic range of the [HbO] signal, with rising signals decreasing the dynamic range, then the peak-amplitude of the hemodynamic response should be negatively correlated with the slope before trial-onset (see Supplementary Figure 3). The amplitude of the hemodynamic signal has also been reported to depend non-linearly on the underlying neuronal activity (Franceschini et al., 2008), and signal amplitude has been shown to depend on the relationship between the different frequency bands of the electrophysiological signal (Magri et al., 2012). Any or all of the above reasons could influence the peak-amplitude, and hence distort its relationship with the neuronal MI. The reasons for the same are currently being investigated.

Limitations

Near-infrared light is incapable of penetrating deep into brain tissue, and hence the acquisition of fNIRS signals is not possible from deeper brain structures such as the thalamus, superior colliculus, substantia nigra, etc. (Ferrari and Quaresima, 2012). Also, the spatial resolution of fNIRS signals is within millimeters. Therefore, this technique is only applicable for measuring hemodynamic changes of cortical tissue close to the dural surface, with a spatial resolution in millimeters. The exact spatial resolution of fNIRS is currently being investigated.

Conclusions

Overall, our results show that epidural fNIRS is a reliable and sensitive method for studying local hemodynamic changes. We also obtained high SNRs for both [HbO] and [HbR] signals recorded from both the 'near' and the 'far' channels. Lastly, we observed strong visual modulation in the [HbO] and [HbR] signals that, and their peak-times were strongly correlated with the underlying neural activity. The current work establishes that simultaneous epidural-fNIRS-electrophysiology is a relatively cheap yet sensitive method for studying neurovascular coupling in primates.

Acknowledgments

We would like to thank Vishal Kapoor and Esther Florin for their valuable suggestions during the analysis of data and writing of the manuscript, and Eduard Krampe and Mirsat Memej for help with the design of the recording chamber and inset. This work was supported by funding from The Max Planck Society (MPG), German Research Foundation (DFG) and the Werner Reichardt Center for Integrative Neurosciences (CIN), Tübingen.

Appendix A. Supplementary data

Supplementary data to this article can be found online at http://dx.doi.org/10.1016/j.neuroimage.2015.07.019.

References

Cardoso, M.M.B., Sirotin, Y.B., Lima, B., Glushenkova, E., Das, A., 2012. The neuroimaging signal is a linear sum of neurally distinct stimulus- and task-related components. Nat. Neurosci. 15, 1298–1306. http://dx.doi.org/10.1038/nn.3170.

Crespi, F., 2007. Near-infrared spectroscopy (NIRS): a non-invasive in vivo methodology for analysis of brain vascular and metabolic activities in real time in rodents. Curr. Vasc. Pharmacol. 5, 305–321.

Crespi, F., Bandera, A., Donini, M., Heidbreder, C., Rovati, L., 2005. Non-invasive in vivo infrared laser spectroscopy to analyse endogenous oxy-haemoglobin, deoxy-haemoglobin, and blood volume in the rat CNS. J. Neurosci. Methods 145, 11–22. http://dx.doi.org/10.1016/j.jneumeth.2004.11.016.

Ferrari, M., Quaresima, V., 2012. A brief review on the history of human functional near-infrared spectroscopy (fNIRS) development and fields of application. Neuroimage 63, 921–935. http://dx.doi.org/10.1016/j.neuroimage.2012.03.049.

Franceschini, M.A., Nissilä, I., Wu, W., Diamond, S.G., Bonmassar, G., Boas, D.A., 2008. Coupling between somatosensory evoked potentials and hemodynamic response in the rat. Neuroimage 41 (2), 189–203. http://dx.doi.org/10.1016/j.neuroimage.2008.02.061.

Fuster, J., Guiou, M., Ardestani, A., Cannestra, A., Sheth, S., Zhou, Y., Toga, A., Bodner, M., 2005. Near-infrared spectroscopy (NIRS) in cognitive neuroscience of the primate brain. 26 pp. 215–220. http://dx.doi.org/10.1016/j.neuroimage.2005.01.055.

Goense, J.B.M., Logothetis, N.K., 2008. Neurophysiology of the BOLD fMRI signal in awake monkeys. Curr. Biol. 18, 631–640. http://dx.doi.org/10.1016/j.cub.2008.03.054.

Keller, C.J., Cash, S.S., Narayanan, S., Wang, C., Kuzniecky, R., Carlson, C., Devinsky, O., Thesen, T., Doyle, W., Sassaroli, A., Boas, D.A., Ulbert, I., Halgren, E., 2009. Intracranial microprobe for evaluating neuro-hemodynamic coupling in unanesthetized human neocortex. J. Neurosci. Methods 179, 208–218. http://dx.doi.org/10.1016/j.jneumeth.2009.01.036.

Kohl-Bareis, M., Obrig, H., Steinbrink, J., Malak, J., Uludag, K., Villringer, A., 2002. Noninvasive monitoring of cerebral blood flow by a dye bolus method: Separation of brain from skin and skull signals. J. Biomed. Opt. 7, 464–470. http://dx.doi.org/10.1117/1.1482719.

Logothetis, N.K., Pauls, J., Augath, M., Trinath, T., Oeltermann, A., 2001. Neurophysiological investigation of the basis of the fMRI signal. Nature 412, 150–157. http://dx.doi.org/10.1038/35084005.

Magri, C., Schridde, U., Murayama, Y., Panzeri, S., Logothetis, N.K., 2012. The amplitude and timing of the BOLD signal reflects the relationship between local field potential power at different frequencies. The Journal of Neuroscience 32, 1395–1407. http://dx.doi.org/10.1523/JNEUROSCI.3985-11.2012.

Saager, R.B., Telleri, N.L., Berger, A.J., 2011. Two-detector corrected near infrared spectroscopy (C-NIRS) detects hemodynamic activation responses more robustly than single-detector NIRS. Neuroimage 55, 1679–1685. http://dx.doi.org/10.1016/j.neuroimage.2011.01.043.

Sirotin, Y.B., Das, A., 2009. Anticipatory haemodynamic signals in sensory cortex not predicted by local neuronal activity. Nature 457, 475–479. http://dx.doi.org/10.1038/nature07664.

Villringer, A., Chance, B., 1997. Non-invasive optical spectroscopy and imaging of human brain function. Trends Neurosci. 20, 435–442.

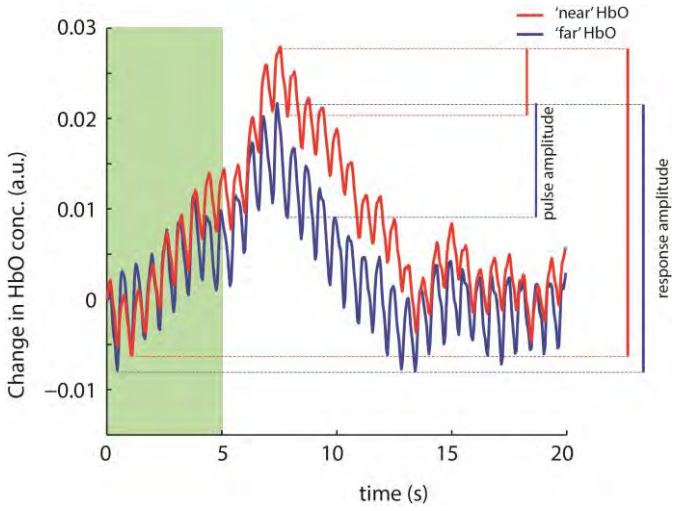

Supplementary figure 1. Single trial comparison of 'near' and 'far' HbO signals. The HbO responses measured from the 'near' and 'far' channels for a single trial of 5s stimulation followed by 15s of rest are shown in the figure. The amplitudes of the pulse and the stimulus response are also compared. It can be clearly seen that the 'near' channel has a larger response amplitude together with a smaller pulse amplitude, indicating higher signal-to-noise ratio.

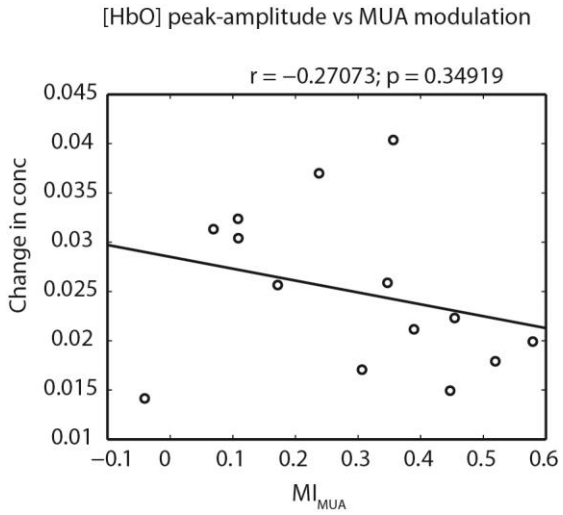

Supplementary Figure 2. Relationship of peak-amplitude with MUA modulation. We find no significant relationship between the mean peak amplitude of the hemodynamic response and the mean MUA modulation. Each data-point represents the mean value over all 20 trials of a run. For a discussion see Section 4.2.

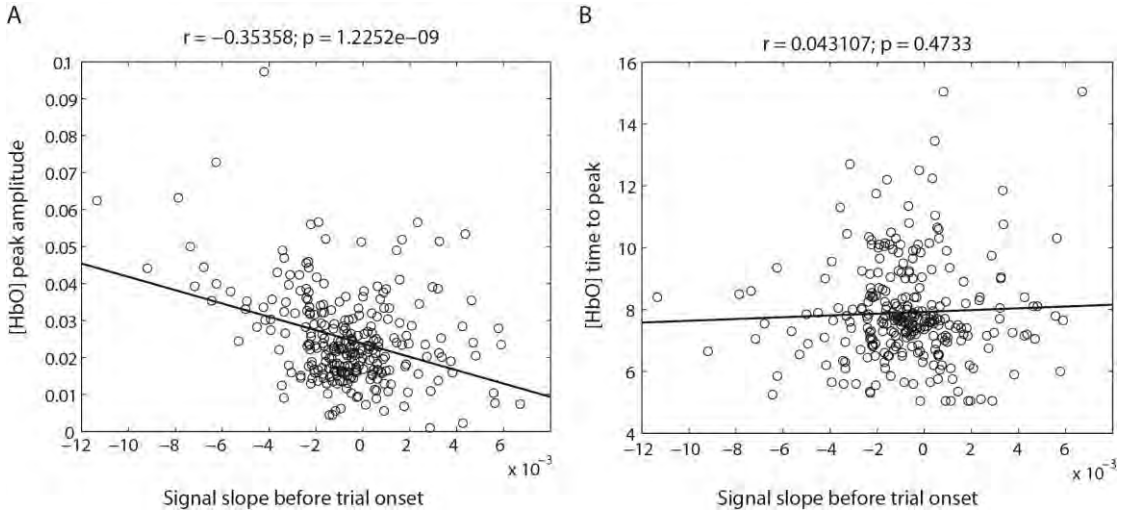

Supplementary Figure 3. Relationship of peak-amplitude and peak-time with underlying signal trends. Here we plot the dependence of the [HbO] peak-amplitude (A) and peak-time (B) on the slope before trial onset. The slope of at the end of the previous trial is calculated by taking the difference between [HbO] values at t=20s and t=17s, and dividing it by 3 i.e., slope = ($[HbO]_{t=20}$ – $[HbO]_{t=17}$)/3. On a trial-by-trial basis, there is a significant correlation between slope at trial onset and [HbO] peak-amplitude (A). However, there is no such dependence with the peak-time (B). The dependence of peak-amplitude on signal trend could be the reason why we don't observe strong correlations between peak-amplitude and neural modulation. Likewise, the independence of peak-time on signal trends leads to a better estimation of underlying neuronal modulation.

Appendix 2: The timing of hemodynamic changes reliably reflects spiking activity

The timing of hemodynamic changes reliably reflects spiking activity

Ali Danish Zaidi*[1,2], Niels Birbaumer[2,3], Eberhard Fetz[4], Nikos Logothetis[1,5], Ranganatha Sitaram*[2,6]

Affiliations:

1. Max Planck Institute for Biological Cybernetics, Tübingen, Germany.
2. Institute for Medical Psychology and Behavioral Neurobiology, University of Tübingen, Germany.
3. Wyss Center for Bio and Neuroengineering, Geneva, Switzerland.
4. Department of Physiology and Biophysics and Washington National Primate Research Center, University of Washington, Seattle, USA.
5. Center for Imaging Sciences, Biomedical Imaging Institute, University of Manchester, UK.
6. Institute for Biological and Medical Engineering, and Department of Psychiatry and Division of Neuroscience, Schools of Engineering, Biology & Medicine, Pontificia Universidad Católica de Chile.

Abstract

Functional neuroimaging is a powerful non-invasive tool for studying brain function, using changes in blood-oxygenation as a proxy for underlying neuronal activity. The neuroimaging signal correlates with both spiking, and various bands of the local field potential (LFP), making the inability to discriminate between them a serious limitation for interpreting hemodynamic changes. Here, we record activity from the striate cortex in two anesthetized monkeys (*Macaca mulatta*), using simultaneous functional near-infrared spectroscopy (fNIRS) and intra-cortical electrophysiology. We find that low-frequency LFPs correlate with hemodynamic signal's peak-amplitude, whereas spiking correlates with its peak-time and initial-dip. We also find spiking to be more spatially localized than low-frequency LFPs. Our results suggest that differences in spread of spiking and low-frequency LFPs across cortical surface influence different parameters of the hemodynamic response. Together, these results demonstrate that the hemodynamic response-amplitude is a poor correlate of spiking activity. Instead, we demonstrate that the timing of the initial-dip and the hemodynamic response are much more reliable correlates of spiking, reflecting bursts in spike-rate and total spike-counts respectively.

Introduction

Functional neuroimaging is currently one of the best non-invasive tools for understanding brain function in healthy, and dysfunction in diseased subjects (Logothetis, 2008), where the peak amplitude of the hemodynamic response is most often used as a proxy for the strength of underlying excitatory neural activity, such as spiking or activity in the gamma band. However, the precise interpretation of the neuroimaging signal is rendered difficult by the fact that it has been reported to reflect various neuronal processes, such as multi-unit spiking, the activity in the various frequency bands of the LFP (Bartolo et al., 2011; Boynton, 2011; Goense and Logothetis, 2008; Logothetis et al., 2001; Maier et al., 2008; Murayama et al., 2010; Rauch et al., 2008; Viswanathan and Freeman, 2007), and even the

relationships among different LFP bands (Magri et al., 2012). Spikes and low-frequency LFPs may, however, represent distinct neural processes such as feedforward and feedback influences (Bastos et al., 2015). For example, spiking seems to represent the features of a visual stimulus (feedforward), whereas neuro-modulatory inputs are reflected in low-frequency LFP bands (feedback) (Belitski et al., 2008). This makes the inability to differentiate between activations associated with spiking-activity or low-frequency LFPs the major limitation in the interpretation of hemodynamic changes (Logothetis, 2008). However, the major portion of such studies focus mainly on the amplitude of the hemodynamic signal, and two other parameters, namely, its peak-time (the time taken by the hemodynamic response to reach its peak) and initial-dip (a transient dip in the hemodynamic signal observed just after stimulus onset) have mostly been ignored.

Interestingly, spiking and low-frequency LFPs are known have different spatio-temporal features. For example, low-frequency LFP activity is more temporally synchronized, but has a larger spread over cortical surface (Logothetis et al., 2007). Spiking activity, in contrast, is spatially more localized, but has a larger temporal spread (e.g. a train of spikes). Since the hemodynamic response is believed to reflect the spatio-temporal pattern of local neuronal activity, it isn't unreasonable to assume that such differences in the pattern of neuronal activity might be reflected in different features of the hemodynamic signal. The ability to identify features in the hemodynamic signal that serve as markers for a specific kind of neuronal activity would enable a clearer and much more precise interpretation of functional neuroimaging studies. Hence, to determine how different hemodynamic parameters correlated to different neuronal processes (such as spiking or LFPs), we performed simultaneous measurements of hemodynamic signals (using fNIRS) and intra-cortical electrophysiology in the primary visual cortex (V1) of two anesthetized monkeys (**Fig. 1a-b**). FNIRS uses a light emitter-detector pair (optode pair) to measure changes in the concentration of oxygenated ([HbO]) and deoxygenated ([HbR]) hemoglobin in a small volume of tissue (Ferrari and Quaresima, 2012; Villringer, 1997). We have recently demonstrated that fNIRS has high SNR when acquired epidurally (Zaidi et al., 2015), making it ideal for studying local neuro-vascular interactions. Using this technique, we recorded sessions of both spontaneous and stimulus-induced activity in the primary visual cortex of two anesthetized monkeys, where a high-contrast whole-field rotating chequerboard was used as visual stimulus. **Fig 1c** shows traces of [HbO], [HbR] and spiking activity for an example run consisting of 20 trials. Each trial consisted of 5s of stimulus presentation followed by 15s of a dark screen. The visual stimulus invoked strong responses, clearly observed in single trials as changes in the traces of HbO, HbR and spike rates.

Results

Timing of the hemodynamic changes best reflects spiking activity

To analyze the relationship between neural modulation and the hemodynamic response, we sorted the trials based on the strength of their spike-rate modulation (**Fig. 2a$_{1\text{-}2}$**), and obtained their corresponding HbO traces (**Fig. 2a$_3$**). A negative trend was observed in the peak-amplitude of the HbO response (**Fig 2a$_3$**), whereas a positive trend was observed in the HbO peak-time (**Fig 2a$_4$**). To overcome the large trial-by-trial variation in the data, we sorted the trials from low to high spike-rate modulation and binned them into five groups. The mean spike rates and [HbO] traces for each group are shown in **Fig. 2b$_{1\text{-}2}$**. **Fig 2b$_{3\text{-}4}$** show the means spike rate versus the mean HbO peak-amplitude and HbO peak-time for each group, along with their standard error of mean (SEM). Surprisingly, spike-rate modulation correlated negatively with HbO peak-amplitude (**Fig. 2b$_3$**; $r = -0.98$; $p < 0.005$; n = 50/group, 5 groups), but positively with HbO peak-time **(Fig. b$_4$**; $r = 0.93$, $p < 0.023$; n=50/group, 5 groups). This relationship was also observed for [HbR] signals (albeit weaker) and was independent of both the number of groups the data were divided into (*supplementary figure 1*), and the threshold for spike detection (*supplementary figure 2*). Trials with higher spike-rate modulations also elicited higher peak-rates and total spike-counts during stimulus presentation (**Fig. 2b$_1$**). A strong relationship between peak spike-rate during stimulus onset and HbO peak-time ($r = 0.8$; $p < 0.01$; **Fig. 2c$_1$**; n=25/group, 10 group) was also observed. However, correlations between total spike-count during stimulus presentation and the HbO peak-time were the strongest (**Fig. 2c$_3$**; $r = 0.9$; $p < 0.001$; n = 25/group, 10 groups).

We also observed robust initial-dips in the high spiking trials (**Fig. 2b$_2$**). The initial-dip has been shown to represent local neuronal activity better than the positive peak (Kim et al., 2000; Watanabe et al., 2013). We therefore analyzed the relationship between spiking and both the initial-dip peak-amplitude and peak-time. We observed a strong correlation between the peak spike-rate and both the HbO initial-dip amplitude ($r = -0.741$; $p = 0.014$; n = 25/group, 10 groups; initial-dip amplitude is negative) and the initial-dip peak-time (**Fig. 2c$_2$**; $r = -0.966$; $p < 10^{-5}$; n=25/bin, 10 bins), demonstrating that although both the amplitude and timing of the initial-dip reflect bursts in spiking activity, its peak-time has a much stronger relationship. Among the various LFP bands, only the high frequency bands correlated with the peak-time of the initial-dip, but not with its amplitude ($p<0.1$). These results imply that for both the initial-dip and hemodynamic response, their peak-times reflect high-frequency neuronal activity more reliably than peak-amplitude, with the strongest correlations observed with spiking activity.

Amplitude of the hemodynamic response reflects low-frequency LFP activity

We next determined the relationship between modulations in the various LFP bands and hemodynamic responses. We filtered the extra-cellular field potential into eight frequency bands, and obtained their respective band-envelope. The trials were then sorted and binned based on the strength of modulation in each band. This band modulation was then correlated with HbO peak-amplitude and HbO peak-time. A positive correlation between DeltaTheta (1-8 Hz)

modulation and HbO peak-amplitude was found ($r = 0.9$, $p < 0.001$; **Fig. 2d$_1$**; n=25/group, 10 groups; *supplementary figure 3*), and a negative (albeit non-significant) correlation with HbO peak-time ($r = -0.5$, $p > 0.1$; n=25/group, 10 groups). Opposing relationships of HbO peak-amplitude with spike-rates and DeltaTheta suggest an interaction between these two neuronal processes. Indeed, a strong negative correlation between DeltaTheta modulation and spike rates was observed ($r = -0.86$; $p < 0.0015$; **Fig. 2d$_3$**). However, when comparing low and high spiking trials within the first quartile of DeltaTheta modulations, we observed a significant increase in both HbO peak-amplitude ($p<0.002$, n=62; Wilcoxon's rank sum test) and HbO peak-time ($p<0.004$, n=62; Wilcoxon's rank sum test) with increase in spiking activity (**Fig. 2d$_3$**). This demonstrates that although spiking does affect HbO peak-amplitude positively, this effect is overshadowed by the influence of low frequency processes on both HbO peak-amplitude and spiking. **Fig. 2e** summarizes the relationship between modulations in different LFP frequency bands and the hemodynamic response parameters. Only modulations in DeltaTheta and Alpha ($r = 0.69$, $p < 0.029$; n = 25/group, 10 groups) correlated significantly with HbO peak-amplitude (and among themselves, $r = 0.91$, $p < 0.001$; n = 25/group, 10 groups). In contrast, only modulations in the MUA band correlated significantly with HbO peak-time. Since the modulation index of the DeltaTheta envelope was not significantly different than zero in our data ($p > 0.1$, Wilcoxon's signed rank test, mean = 0.0149 ± 0.011 SEM; *supplementary figure 4)*, these observations seem to reinforce the notion that spiking and low-frequency LFPs might represent different neural processes in the primary visual cortex (Belitski et al., 2008).

Analysis of spontaneous activity reveals similar relationships

It might be argued that these relationships do not represent local neurovascular coupling, but are artifacts arising from strong visual stimulation. To ensure this was not the case, we analyzed sessions of spontaneous activity, recorded in the absence of visual stimulation with the subject's eyes closed. Bursts in spike rates were detected and corresponding [HbO] traces were obtained from -5 to +20 seconds relative to the burst peak, and zero corrected by subtracting the mean value from -5 to -3s relative to burst peak. These traces were then sorted and grouped based on burst strength (Fig 3a1-2). The peak-rate of spiking was strongly correlated with both HbO peak-time ($r = 0.97$, $p <$ 10-5; n=85/group, 10 groups; Fig 3b1) and initial-dip ($r = -0.8$, $p = 0.005$; n=85/group, 10 groups; Fig 3b2), but not HbO peak-amplitude ($r = 0.31$; $p = 0.62$; n = 85/group, 10 groups). The correlation between peaks in the different LFP band-envelopes and HbO peak-amplitude and HbO peak-time was also analyzed. Strong correlations were observed only between activity in high-frequency LFPs and HbO peak-time, whereas no significant relationships were found for peak amplitudes (Fig. 3c). These observations demonstrate that the relationship between spiking activity and hemodynamic peak-time are consistent across recordings of both spontaneous and stimulus-induced activity.

Discussion

Prima facie, our results might seem different from earlier studies of neurovascular coupling (Goense and Logothetis, 2008; Logothetis et al., 2001). However, it must be noted that most previous studies have analyzed time-series cross-correlations between neuronal activity and hemodynamic signals to estimate the strength of neurovascular coupling. In our study, we use a feature based approach, where individual features of neuronal activity are correlated with features of the hemodynamic response. Indeed, a cross-correlation based analysis reveals results similar to those previously observed (Goense and Logothetis, 2008; Logothetis et al., 2001), with low-frequency processes eliciting weak, and high-frequency processes eliciting strong correlations, for both time-series cross-correlation analysis (*Supplementary figure 5*) and HRF-convolutions obtained from spontaneous activity (*Supplementary figure 6*). However, cross-correlations are strongly dependent on the shape of the underlying signals, and consequently, may misrepresent underlying relationships. Our feature-based approach enables a more robust investigation, as we use multiple features of neuronal activity (e.g. neuronal modulation index, peak neuronal activity, mean activity during stimulus presentation, etc.) and obtain similar results.

These results probably arise from the differences in the spatio-temporal spread of low and high-frequency neuronal processes across the cortical surface. Both previous work (Logothetis et al., 2007) and our data demonstrate that correlations in high-frequency neuronal processes have a small spread over cortical surface (**Fig. 4a**) than those in high-frequencies (**Fig. 4b**). Modulations in lower frequencies, in contrast, are more synchronized (small temporal spread) and have a larger spatial-spread over the cortical surface, potentially dilating more vessels simultaneously. The simultaneous increase in flow rate of HbO would translate to an increase in the peak-amplitude of the hemodynamic signal. Indeed, both previous work (Devor et al., 2005) and our data (**Fig. 4c**) demonstrate that a larger spread of neuronal activity across the cortical surface causes larger hemodynamic response amplitudes. In contrast, localized neuronal responses are known to cause arteriole dilation with high spatial precision and limited spread (Sirotin et al., 2009). Being more localized, high-frequency processes such as spiking would dilate fewer arterioles, and with longer activity, the flow rate in these dilated arterioles would saturate. Thus, larger spike counts should affect HbO peak-time more than HbO peak-amplitude. Indeed, compared to early-peaking trials, late-peaking trials had significantly higher spike-rates during both the 'On' and 'Off' epochs (**Fig. 4d**). Furthermore, we found a strong correlation between the HbO peak-time and the total number of spikes up to the HbO peak-time for each trial ($r=0.98$, $p<10^{-6}$, **Fig. 4d inset**). This result clearly demonstrates the HbO peak-time reliably reflects the sum of spikes (i.e., the temporal spread of spiking) from trial-onset up to the hemodynamic response peak.

Curiously, we also observed that the timing of the initial-dip correlated with bursts in spike-rates better than its amplitude. To determine if the amplitude was more reflective of the spatial-spread of spiking than the strength of

spiking, we analyzed the effect of synchronized bursts in spiking across tetrodes on both the initial-dip peak-amplitude and peak-time. We first obtained all trials with high spike-rate bursts on Tetrode1 (bursts larger than the median value), and further divided these trials into two groups, based on whether Tetrode2 had spike-bursts larger or smaller than the median (obtaining trials with high (n=81) and low (n=38) spike-coherence, respectively). We found that compared to low spike-coherence, trials with high spike-coherence had significantly larger initial-dip amplitudes ($p<0.001$; Wilcoxon's one-tailed rank-sum test), but their initial-dip peak-times, and response peak-amplitudes and peak-times were unchanged ($p>0.4$) (*supplementary figure 7*). These observations support our recent suggestion that the initial-dip is a vascular response (Zaidi et al, submitted), given its dependence on the spatio-temporal dynamics of the underlying spiking activity, and also clearly demonstrate that differences in the spatial spread of neuronal processes across cortical tissue are reflected in different parameters of the hemodynamic signal.

Since we use simultaneous epidural fNIRS and intra-cortical electrophysiology to measure hemodynamic changes in anesthetized monkeys, it might be questioned how these results compare to the awake preparation, or to different neuroimaging modalities. But stark differences are unlikely, as under the anesthesia conditions we used, the correlations between neuronal activity and hemodynamic signals are not very different between the anesthetized and awake preparations, at least in the primary visual cortex (Goense and Logothetis, 2008). Furthermore, previous work in awake human subjects, where BOLD-fMRI responses to an almost identical visual stimulation paradigm were recorded, demonstrates that hemodynamic response peak-times and initial-dips are strongly correlated (Watanabe et al., 2013). Our data also reveals a strong correlation between HbO peak-time and initial-dip ($r=0.84$, $p=0.0025$; n=25/group, 10 groups), both of which correlate strongly with spiking (**Fig. 2c_1-c_2**, **Fig. 3b_1-b_2**). Based on this similarity with awake human recordings, we expect our results to be consistent across both neuroimaging modalities and states of wakefulness.

Since we do not find a relationship between excitatory neural activity and the hemodynamic response peak-amplitude, a result consistent across recordings of stimulus-induced and spontaneous activity, our study adds to the mounting evidence that the amplitude of the hemodynamic response is an unspecific marker of excitatory neuronal activity. Although we did find correlations in the hemodynamic signal's peak-amplitude and low-frequency LFP activity, these relationships were not consistent across recordings of stimulus-induced and spontaneous activity, probably because of the difference in the underlying relationships of the various LFP bands in these two conditions (*Supplementary figure 8*). Consequently, these results also question the usefulness of canonical HRFs, as well as the practice of convolving them with neuronal activity and correlating them to observed hemodynamic responses. Furthermore, we also find that spiking is inversely correlated to low-frequency LFPs, and also to the hemodynamic response amplitude. Previous work has also demonstrated that low-frequency LFPs are inversely correlated to spiking, in both alert, behaving monkeys (Panagiotaropoulos et al., 2013) and the awake and REM states in humans

(Destexhe, 1998), corroborating our results, and supporting the idea that they represent two distinct neural processes.

To summarize, our results demonstrate that the amplitude of hemodynamic responses is a poor correlate of spiking activity. Instead, we demonstrate that it is the timing of both the initial-dip and the hemodynamic response that is a much more reliable correlate of spiking activity, reflecting bursts in spike-rate and the sum-of-spikes until the hemodynamic response peak, respectively.

References

Bartolo, M.J., Gieselmann, M.A., Vuksanovic, V., Hunter, D., Sun, L., Chen, X., Delicato, L.S., and Thiele, A. (2011). Stimulus-induced dissociation of neuronal firing rates and local field potential gamma power and its relationship to the resonance blood oxygen level-dependent signal in macaque primary visual cortex. Eur. J. Neurosci. *34*, 1857–1870.

Bastos, A.M., Vezoli, J., Bosman, C.A., Schoffelen, J.M., Oostenveld, R., Dowdall, J.R., DeWeerd, P., Kennedy, H., and Fries, P. (2015). Visual areas exert feedforward and feedback influences through distinct frequency channels. Neuron *85*, 390–401.

Belitski, A., Gretton, A., Magri, C., Murayama, Y., Montemurro, M. a, Logothetis, N.K., and Panzeri, S. (2008). Low-frequency local field potentials and spikes in primary visual cortex convey independent visual information. J. Neurosci. *28*, 5696–5709.

Boynton, G.M. (2011). Spikes, BOLD, Attention, and Awareness: A comparison of electrophysiological and fMRI signals in V1. J. Vis. *11*, 12–12.

Destexhe, a (1998). Spike-and-wave oscillations based on the properties of GABAB receptors. J. Neurosci. *18*, 9099–9111.

Devor, A., Ulbert, I., Dunn, A.K., Narayanan, S.N., Jones, S.R., Andermann, M.L., Boas, D.A., and Dale, A.M. (2005). Coupling of the cortical hemodynamic response to cortical and thalamic neuronal activity. Proc. Natl. Acad. Sci. U. S. A. *102*, 3822–3827.

Ferrari, M., and Quaresima, V. (2012). A brief review on the history of human functional near-infrared spectroscopy (fNIRS) development and fields of application. Neuroimage *63*, 921–935.

Goense, J.B.M., and Logothetis, N.K. (2008). Neurophysiology of the BOLD fMRI Signal in Awake Monkeys. Curr. Biol. *18*, 631–640.

Kim, D.S., Duong, T.Q., and Kim, S.G. (2000). High-resolution mapping of iso-orientation columns by fMRI. Nat. Neurosci. *3*, 164–169.

Logothetis, N.K. (2008). What we can do and what we cannot do with fMRI. Nature *453*, 869–878.

Logothetis, N.K., Pauls, J., Augath, M., Trinath, T., and Oeltermann, a (2001). Neurophysiological investigation of the basis of the fMRI signal. Nature *412*, 150–157.

Logothetis, N.K., Kayser, C., and Oeltermann, A. (2007). In Vivo Measurement of Cortical Impedance Spectrum in Monkeys: Implications for Signal Propagation. Neuron *55*, 809–823.

Magri, C., Schridde, U., Murayama, Y., Panzeri, S., and Logothetis, N.K. (2012). The amplitude and timing of the BOLD signal reflects the relationship between local field potential power at different frequencies. *32*, 1395–1407.

Maier, A., Wilke, M., Aura, C., Zhu, C., Ye, F.Q., and Leopold, D.A. (2008). Divergence of fMRI and neural signals in V1 during perceptual suppression in the awake monkey. Nat. Neurosci. *11*, 1193–1200.

Murayama, Y., Bießmann, F., Meinecke, F.C., Müller, K.R., Augath, M., Oeltermann, A., and Logothetis, N.K. (2010). Relationship between neural and hemodynamic signals during spontaneous activity studied with temporal kernel CCA. Magn. Reson. Imaging *28*, 1095–1103.

Panagiotaropoulos, T.I., Kapoor, V., and Logothetis, N.K. (2013). Desynchronization and rebound of beta oscillations during conscious and unconscious local neuronal processing in the macaque lateral prefrontal cortex. Front. Psychol. *4*, 1–10.

Rauch, A., Rainer, G., and Logothetis, N.K. (2008). The effect of a serotonin-induced dissociation between spiking and perisynaptic activity on BOLD functional MRI. Proc. Natl. Acad. Sci. U. S. A. *105*, 6759–6764.

Sirotin, Y.B., Hillman, E.M.C., Bordier, C., and Das, A. (2009). Spatiotemporal precision and hemodynamic mechanism of optical point spreads in alert primates. Proc. Natl. Acad. Sci. U. S. A. *106*, 18390–18395.

Villringer, A. (1997). Non-invasive optical spectroscopy and imaging of human brain function. Trends Neurosci. *20*, 435–442.

Viswanathan, A., and Freeman, R.D. (2007). Neurometabolic coupling in cerebral cortex reflects synaptic more than spiking activity. Nat. Neurosci. *10*, 1308–1312.

Watanabe, M., Bartels, A., Macke, J.H., Murayama, Y., and Logothetis, N.K. (2013). Temporal Jitter of the BOLD Signal Reveals a Reliable Initial Dip and Improved Spatial Resolution. Curr. Biol. *23*, 2146–2150.

Zaidi, A.D., Munk, M.H.J., Schmidt, A., Risueno-Segovia, C., Bernard, R., Fetz, E., Logothetis, N., Birbaumer, N., and Sitaram, R. (2015). Simultaneous epidural functional near-infrared spectroscopy and cortical electrophysiology as a tool for studying local neurovascular coupling in primates. Neuroimage *120*, 394–399.

Acknowledgements

The authors thank Cristina Risueno and Rebekka Bernard for help with data collection, and Vishal Kapoor and Esther Florin for feedback on an earlier version of this manuscript. This work was supported by funding from the Max Planck Society (MPG), German Research Foundation (DFG) and the Werner Reichardt Center for Integrative Neurosciences (CIN), Tübingen, the New INDIGO grant fund and the Badenwuerttemberg-Singapore Life Sciences grant.

Abbreviations

[HbO]: concentration of oxy-hemoglobin ($mol \cdot cm^{-3}$)

[HbR]: concentration of deoxy-hemoglobin ($mol \cdot cm^{-3}$)

BOLD: blood-oxygen level dependent signal

FNIRS: functional near-infrared spectroscopy

LFP: local field potential

MUA: multi-unit activity

HbO peak-amplitude: peak amplitude of the HbO response

HbO peak-time: time from stimulus onset until peak of HbO response

SDU: Standard-deviation units

Methods

Surgery and craniotomy

Two healthy adult monkeys, M1 (female; 8 kg) and M2 (male; 10 kg), were used for the experiments. All vital parameters were monitored during anaesthesia. After sedation of the animals using ketamine (15 mg/kg), anaesthesia was initiated with fentanyl (31 µg/kg), thiopental (5 mg/kg), and succinylcholine chloride (3 mg/kg), and then the animals were intubated and ventilated. A Servo Ventilator 900C (Siemens, Germany) was used for ventilation, with respiration parameters adjusted to each animal's age and weight. Anaesthesia was maintained using remifentanil (0.2–1 µg/kg/min) and mivacurium chloride (4–7 mg/kg/h). An iso-osmotic solution (Jonosteril, Fresenius Kabi, Germany) was infused at a rate of 10 ml/kg/h. During the entire experiment, each animal's body temperature was maintained between 38.5 °C and 39.5 °C, and SpO2 was maintained above 95%. Under anaesthesia, a craniotomy was made on the left hemisphere of the skull to access the primary visual cortex. During each experiment, the bone was removed to create a rectangular slit measuring 3 mm anterio-posteriorly and 20 mm medio-laterally, exposing the dura. Connective tissue, if present above the dura, was carefully removed. For each monkey, at least two weeks were allowed to pass between successive experiments. All experiments were approved by the local authorities (Regierungspräsidium, Tübingen) and are in agreement with guidelines of the European Community for the care of laboratory animals.

Near-infrared Spectroscopy

We used a NIRScout machine purchased from NIRx Medizintechnik GmbH, Berlin. The system performs dual wavelength LED light-based spectroscopic measurements. The wavelengths used were 760nm and 850nm with LEDs operating at 2.5mW per wavelength. Sampling was performed at 20Hz. We used modified emitters and detectors, and optical fibre bundles for sending the

light from the LED source into the tissue, and also for detecting refracted light from the tissue. The fibre bundles were ordered from NIRx Medizintechnik GmbH, Berlin, Germany. Both the emitter and detector fibre bundles had iron ferrule tips with an aperture of 2.5mm on the ends that touched the dura. The recording instrument was connected via USB to a laptop computer running an interactive software called NIRStar provided along with the instrument. The software was used for starting and stopping recordings, and also for setting up the various parameters, such as, the number of sources and detectors, and the sampling rate. The instrument received TTL pulses from the stimulus system and the electrophysiological recording system, for synchronization purposes. The system sent 1ms TTL pulses every 50ms to the recording system that corresponded to light pulses.

Electrophysiology

Custom built tetrodes and electrodes were used. All tetrodes and single electrodes had impedance values less than 1 MΩ. The impedance of each channel was noted before loading the tetrodes on to the drive, and once again while unloading the tetrode after the experiment, to ensure that the contacts were intact throughout the duration of the experiment. To drive the electrodes into the brain a 64-channel Eckhorn matrix was used (Thomas Recording GmbH, Giessen, Germany). The electrodes were loaded in guide tubes a day before the experiment. On the day of the experiment, the tetrodes were driven using a software interface provided by Thomas Recording GmbH, Giessen, Germany. The output was connected to a speaker and an oscilloscope, with a switch to help cycle between different channels. We advanced electrodes into the cortex one by one until we heard a reliable population response to a rotating checkerboard flickering at 0.5Hz.

Spontaneous activity

For each run, spontaneous activity was recorded for 15 minutes, in the absence of visual stimulation. The eyes of the monkey were closed and a cotton gauze was used to cover the eyelids. Peak spike-rates were obtained by implementing peak-detection in the trace of spike-rates. For spiking and all frequency bands, it was ensured that peaks are at least 20s apart from each other.

Visual stimulation

A fundus camera was used to locate the fovea for each eye. For presenting visual stimulation, a fibre optic system (Avotec, Silent Vision, USA) was positioned in front of each eye, so as to be centered on the fovea. To adjust the plane of focus, contact lenses (hard PMMA lenses, Wöhlk, Kiel, Germany) were inserted to the monkey's eyes. We used whole-field, rotating chequerboard to drive the neural activity. The direction of rotation was reversed every second. Each trial consisted of 5 seconds of visual stimulation followed by 15 seconds of a dark screen. A single run consisted of 20 trials. Data presented are from 14 runs spread over 8 experimental days.

Signal processing and data analysis

All analyses were performed in MATLAB using custom written code. Only runs that cleared visual screening for artifacts were used. Data points that were larger than 5 SDU were excluded from the analysis, so as to avoid tail-effects for correlation analysis. Normality for each distribution was confirmed before analysis was performed. Trials with HbO peak-time and peak-amplitude larger than 5 SDU were removed from the analysis to avoid tail effects in correlation analysis (Supplementary figure 10).

296 FNIRS signal processing

297 The raw wavelength absorption data from the NIRS system was converted to concentration changes of [HbO] and [HbR] using a
298 modified Beer-Lambert equation. For correlating hemodynamic signals with neural activity, the signals were filtered between 0.01
299 and 5 Hz to remove any low frequency drifts. Since the change in [HbR] was negative, the peak amplitudes for [HbR] are, thus,
300 also negative. For a trial-by-trial analysis, the hemodynamic response for each trial was zero-corrected by subtracting, from each
301 hemodynamic response, the value at the start of the trial.

302 Electrophysiological signal processing

303 The mean extracellular field potential signal was recorded at 20.8333 kHz and digitized using a 16-bit AD converted. From the
304 raw signal, eight frequency bands (namely, DeltaTheta (1-8 Hz), Alpha (9-15 Hz), Spindle (15-20 Hz), low Gamma (20-40 Hz),
305 Gamma (40-60 Hz), high Gamma (60-120 Hz), very high Gamma (120-250 Hz) and MUA (1-3 kHz)) were band-pass filtered
306 using a 10^{th} order Butterworth filter. The envelope for each band was then obtained by taking the absolute value of the Hilbert
307 transform of the filtered signal. The band-envelope was then converted to standard deviation units by subtracting the mean and
308 dividing by the standard deviation of the signal. This signal was then resampled at 20 Hz, to allow comparisons with
309 hemodynamic signals.

310 Spike rates were obtained by detecting peaks in the MUA signal larger than a threshold (2, 3 or 4 SDU), and by counting the
311 threshold-crossing events in 50ms bins. Varying the detection threshold between 2, 3 or 4 SDU did not affect the results; the
312 modulation of spike rates was significant irrespective of spike-detection threshold. Only recordings from the tetrode closest to the
313 emitter were used.

314 Calculation of modulation indices

315 The 'On' epoch for each trial was defined as the time from 0 to 5.1 seconds. The extra 0.1s were added to accommodate for the off
316 response. The 'Off' epoch was defined as the time between 5.1 to 10.1 seconds. The modulation index (MI) for each trial was then
317 calculated using the formula: neural modulation = $(BE_{On}-BE_{Off}) / (BE_{On}+BE_{Off})$; where BE_{On} is the mean band envelope during the
318 five seconds of Stim On, and BE_{Off} is the mean band envelope during the first five seconds of Stim Off for each trial.

319 Statistics

320 All correlation coefficients represent Pearson's correlation coefficient and corresponding significance values.

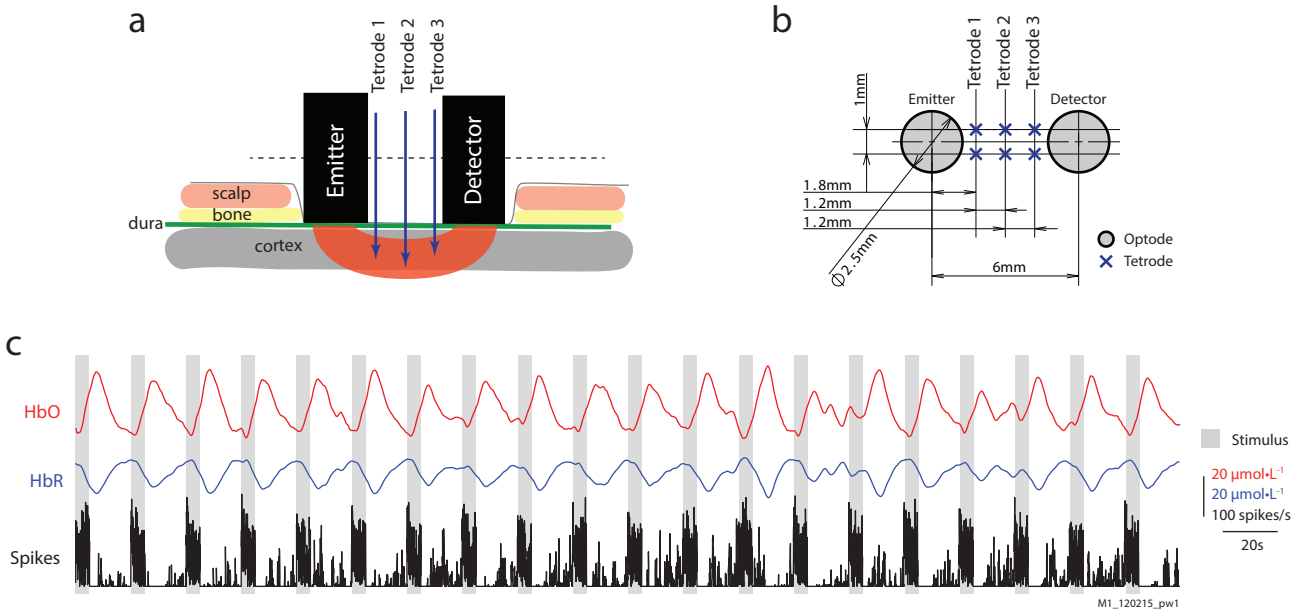

Figure 1. Overview of acquired signals. A) Illustration of the sensor array with placement of fNIRS optodes and electrodes relative to scalp and brain tissue. B) Transverse section of the sensor array with distances between optodes and electrodes. See methods for details. C) Traces of HbO, HbR, and Spiking from an example run with 20 trials. Grey bars represent epochs of visual stimulation.

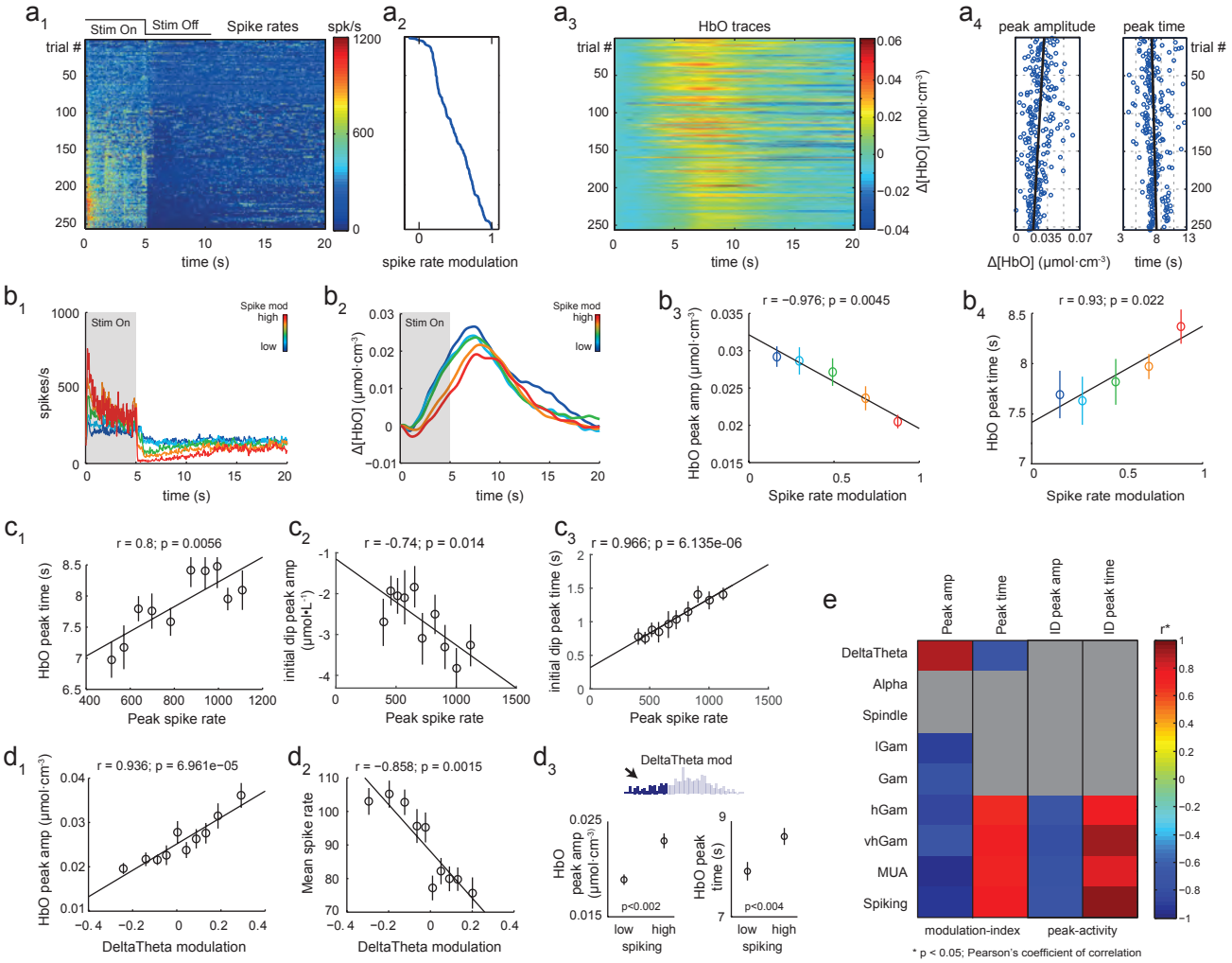

Fig 2. Correlation of spike-rates and LFPs to peak-time and peak-amplitude. a1) Spike rate of trials sorted based on modulation index of spike rate. a2) modulation index of each trial corresponding to a1. a3) [HbO] traces of the corresponding trials from a1. a4) A clear negative trend in peak-amplitude and positive trend in HbO peak-time can be observed for traces corresponding to a2, along with a large trial-by-trial variation. b1-2) Mean traces of spike rates (b1) and [HbO] traces (b2) for each group, when trials were sorted and grouped based on spike-rate modulation. b3-4) Correlation of mean spike-rate modulation with mean HbO peak-amplitude (b3) and mean peak-time (b4) (n=50 per group) from each group. c1-2) Correlations of mean peak-time with peak spike rate. c2-3) Correlations of peak spike-rate with initial-dip peak-amplitude and peak-time. d1) Correlation of DeltaTheta modulation with peak-amplitude (d1) and mean spike rate (d2) for trials sorted and grouped on DeltaTheta modulation. d3) Within the first quartile of DeltaTheta modulations (inset), spiking significantly affected both peak-amplitude and peak-time (p-values based on two-tailed Wilcoxon ranked sum test). e) Correlations of HbO response peak-amplitude and peak-amplitude with the modulation index, and the initial-dip peak-amplitude and peak-time with peak activity in different LFP frequency bands. Only significant correlations (p<0.05; n=25/group, 10 groups) are coloured. All error bars represent SEM.

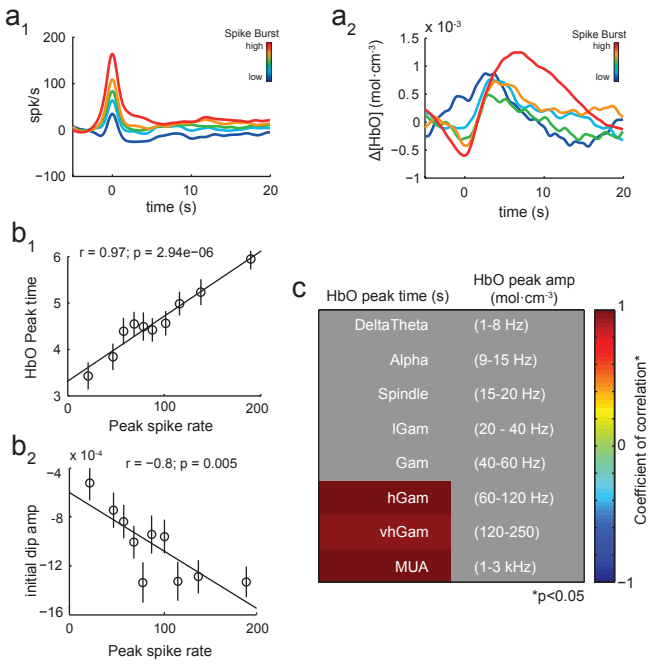

Fig 3. Relationships between neural activity and HbO parameters in spontaneous activity. a1-2) Mean traces of spike rate (a1) and corresponding [HbO] traces (a2) for each group, sorted from low to high spike-burst strengths. b) Correlations of the peak spike-rate for each group and the peak-time (b1) and initial-dip (b2) when spike bursts were sorted on peak spike rate. Error bars represent SEM. c) Correlation of peak-amplitude and peak-time with peaks in the envelope of different LFP frequency bands. Only significant correlations ($p<0.05$) are coloured. The peak-amplitude correlates with peaks in the Alpha band, and peak-time with peaks in the high gamma bands and MUA band.

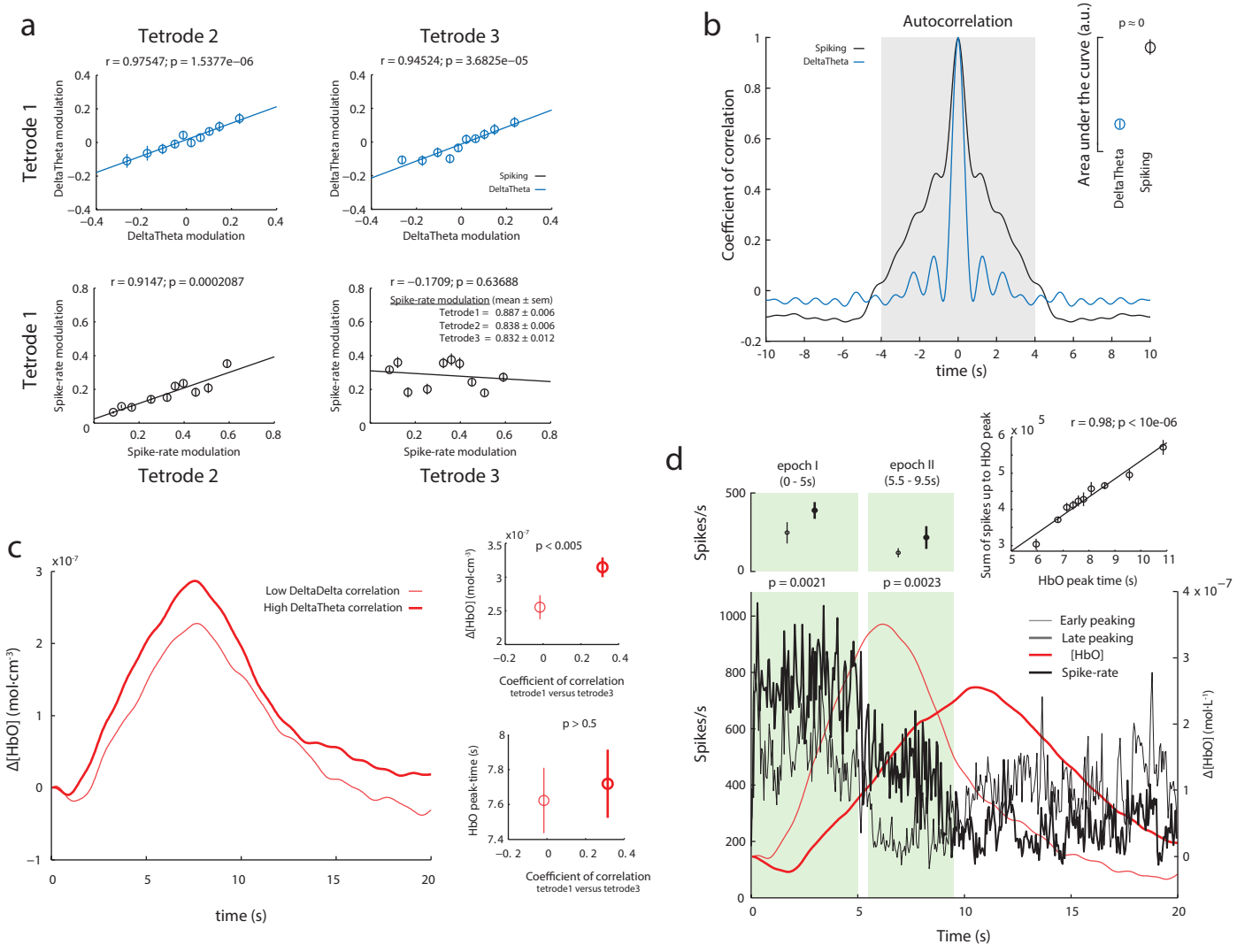

Fig 4. Spatio-temporal profiles of spiking versus DeltaTheta activity, and thier effect on the hemodynamic response. (a) DeltaTheta modulations are highly correlated between both Tetrode1 and Tetrode2, and Tetrode1 and Tetrode 3. However, spike-rate modulation are highly correlated between Tetrode1 and Tetrode2, while no correlations exist between Tetrode1 and Tetrode3, even though the distributions of spike-rate modulations are almost identical across tetrdodes. This illustrates that spiking activity is more spatially localized than DeltaTheta activity. (b) Mean autocorrelation of spike-rates and DeltaTheta activity across all trials. Inset) Distributions of the area-under-the-curve (between -4s to +4s, shaded region in main figure) for spiking and DeltaTheta activity. Bars represent CI-95 Spiking has a larger temporal spread than DeltaTheta. (c) Trials with higher correlations of DeltaTheta between Tetrode1 and Tetrode 3 (thick traces) have a significantly higher peak-amplitude (inset top-right) (but not peak-time (inset bottom-right) than those with low correlations (thin traces). (d) When comparing early-peaking (thin traces) vs late-peaking (thick traces) trials (top and bottom 10% of all trials, n=26), we find that late-peaking trials have significantly higher spike-rates not only during stimulus presentation (epoch I) but also after the stimulus is turned off (epoch II). A very strong correlation is observed when between the HbO peak-time and the sum of the spikes up to HbO peak-time for each trial (inset).

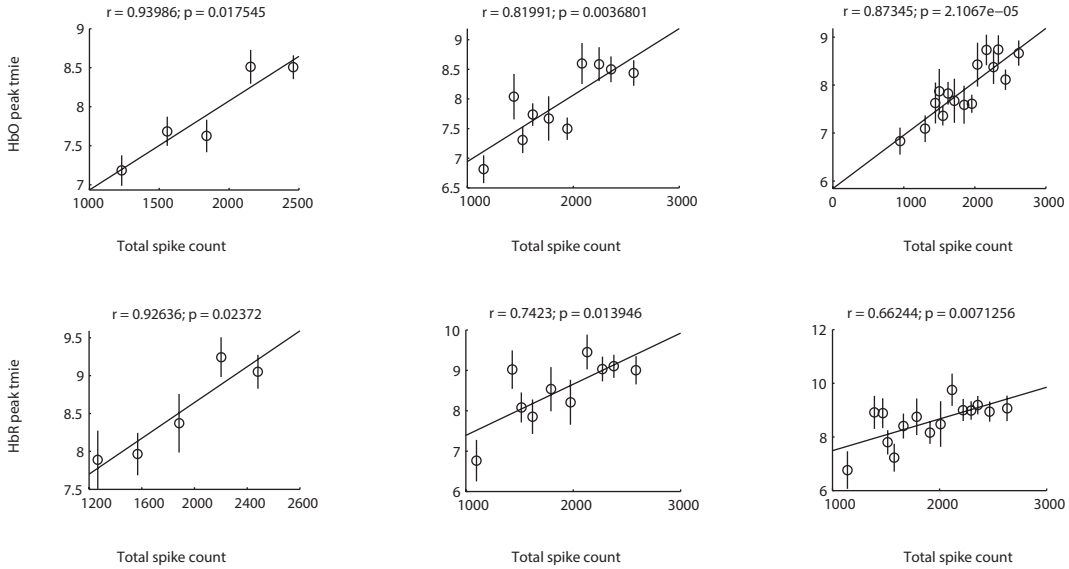

Supplementary figure 1. Independence of results on group size. Trials were divided into 5, 10 and 15 groups, and the mean total spike count for each group was correlated with the mean HbO and HbR peak time. Varying the size of the group did not change the relationship between the total spike counts and HbO and HbR peak times.

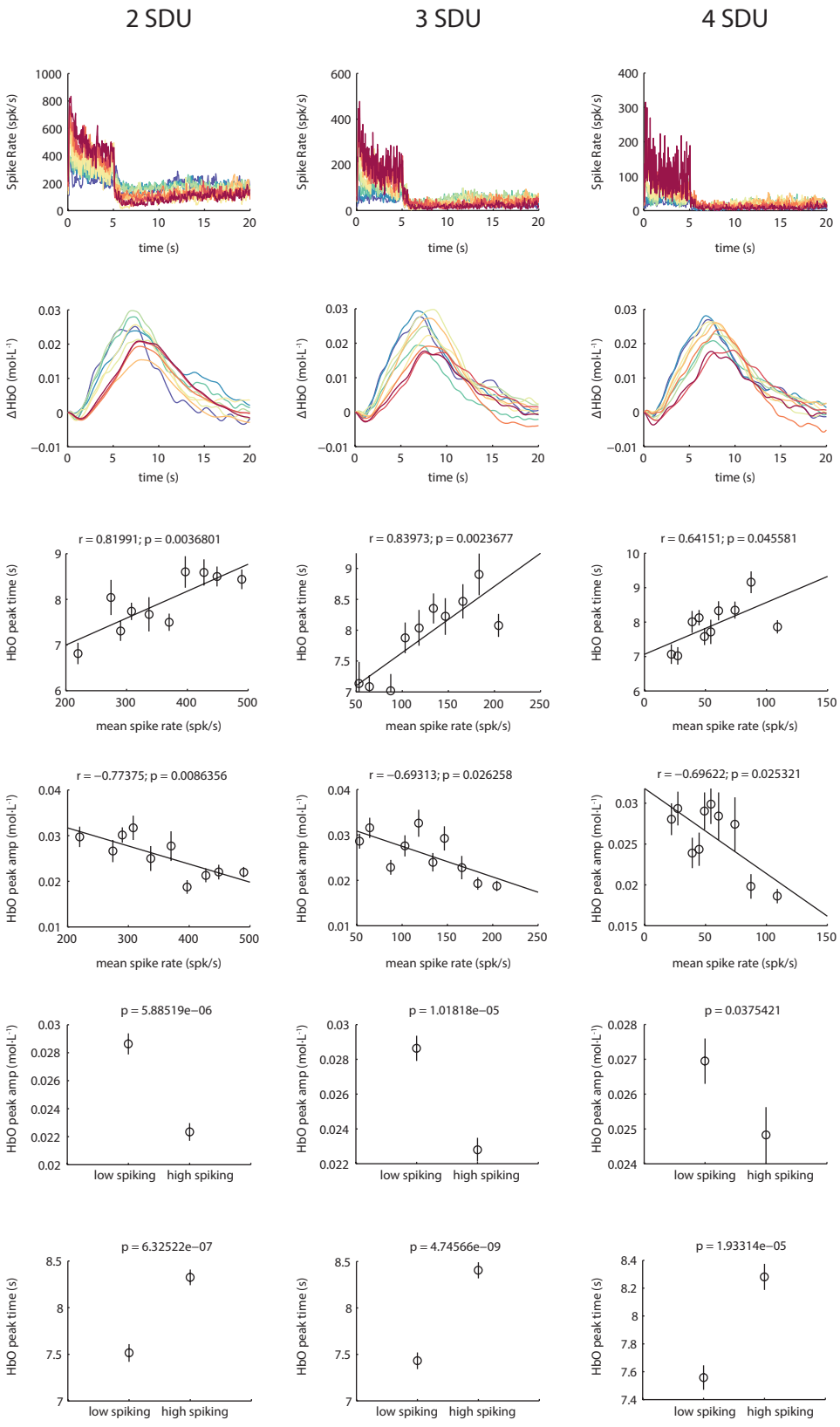

Supplementary figure 2. Results shown in Fig. 2 are consistent across multiple spike detection thresholds.

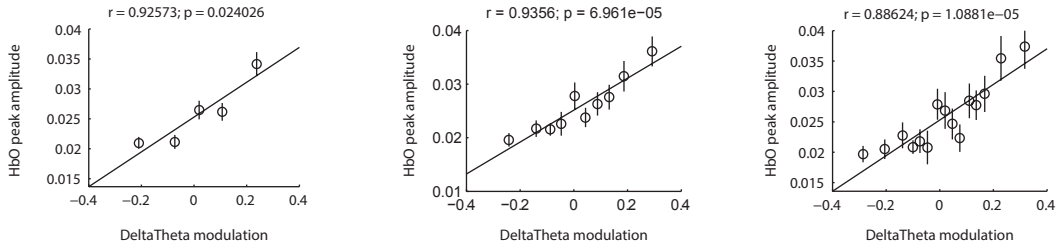

Supplementary figure 3. Correlations between DeltaTheta modulation and HbO peak-amplitude are independent of group size or number of trials per bin. We also observed a correlation between HbO peak-amplitude with the peak DeltaTheta amplitude during stimulus presentation (r = 0.67, p = 0.03; n=25/bin, 10 bins), but it wasn't as strong as the correlation of HbO peak-amplitude with DeltaTheta modulation (r = 0.94, p < 10-4; n = 25/bin, 10 bins; middle panel above).

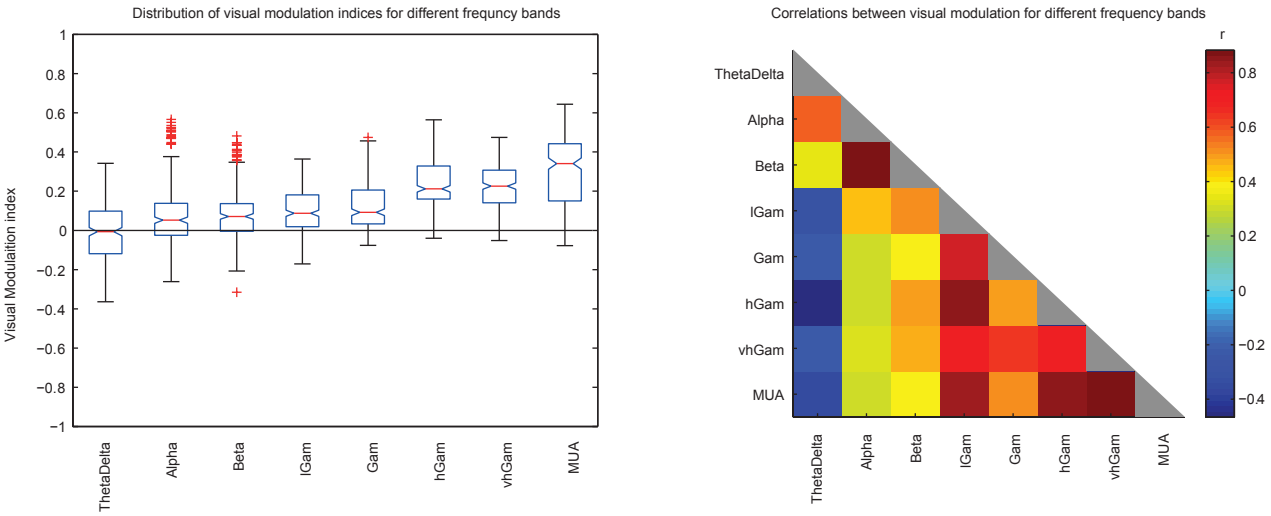

Supplementary figure 4. Visual modulation of different frequency bands and their relationships.
Left panel shows the distribution of visual modulation indices for the different frequency bands (see Methods for definition of bands). Notches represent 95% confidence intervals. Apart from the DeltaTheta, every band had significant visual modulation, which increased with increasing frequency bands.
Right panel shows the correlations between the visual modulation indices in different frequency bands. In general the three lowest frequency bands, namely DeltaTheta, Alpha and Spindle seemed to correlate positively with each other, and negatively with all bands afterwards. Modulation indices between the highest frequency bands were tightly correlated. This observation suggests that low-frequency (1-20 Hz) and high-frequency (20 – 1000 Hz) neuronal activity may represent different neuronal processes, with spiking being more representative of stimulus induced activity and low-frequency LFPs representing neuromodulatory inputs.

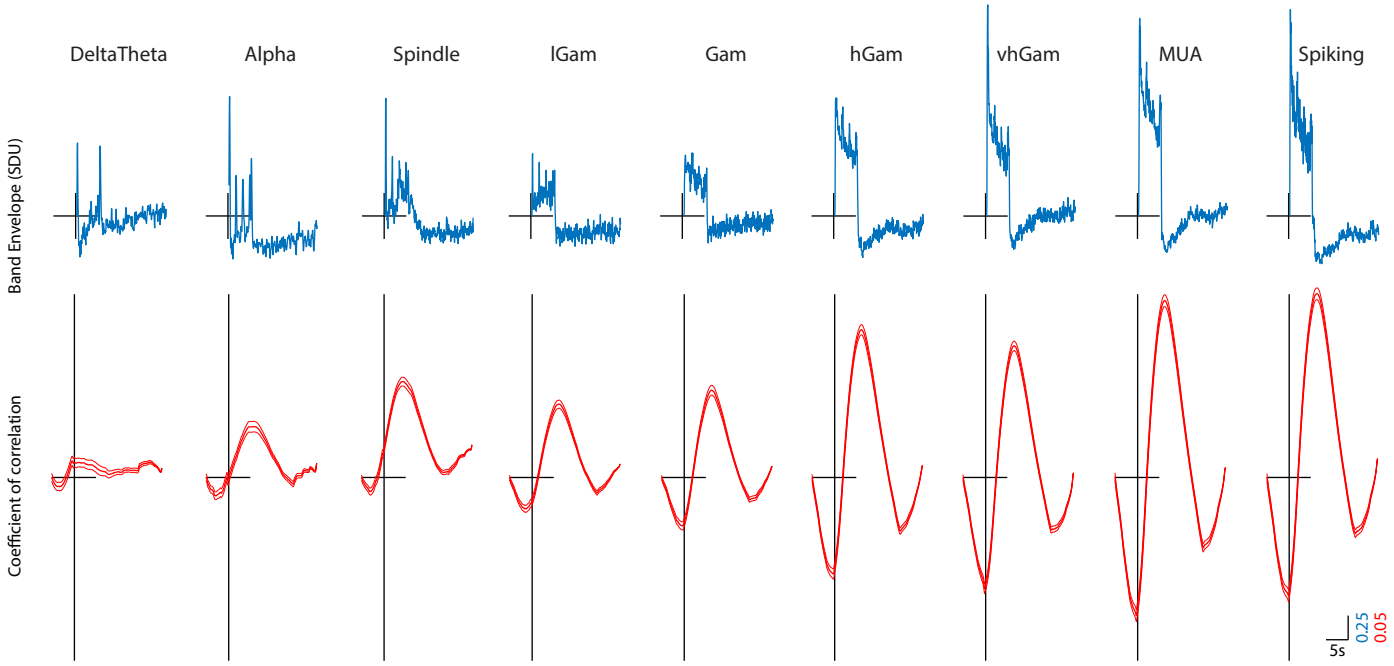

Supplementary figure 5. Mean LFP profiles and cross-correlations with the HbO response.
The upper panels represent the mean LFP profiles for each LFP band during stimulus induced activity. The center of the cross represents the origin. The lower panels reprsent the mean cross-correlations between each LFP timeseries and the HbO response for each trial. As can be clearly observed, the cross-correlations are low for the low-frequency LFPs and high for the high-frequency LFPs. These results are fundamentally different from what we observe based on a feature-to-feature correlation analysis (see Fig. 2).

a

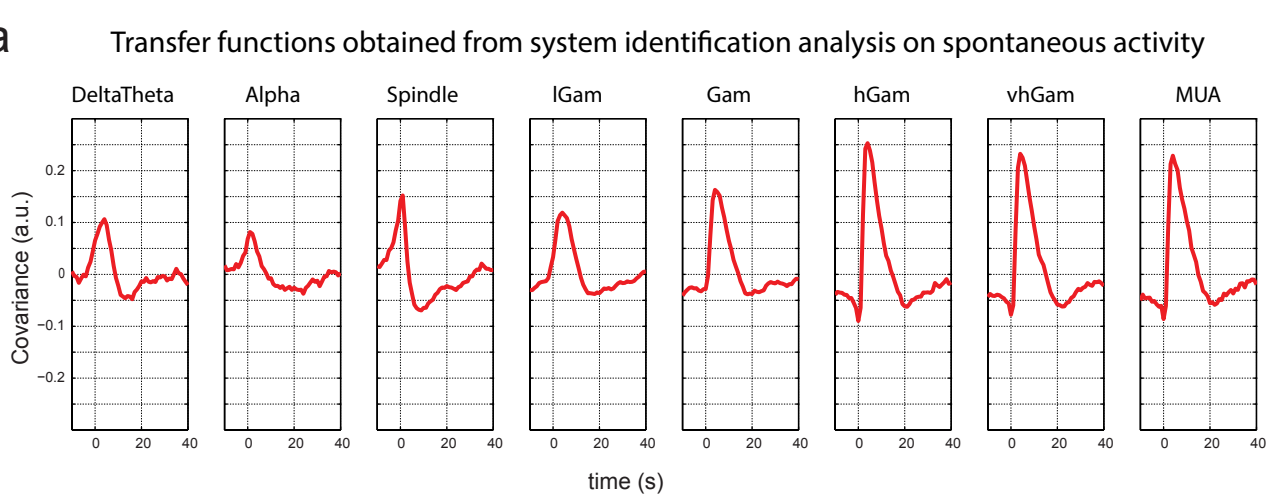

b

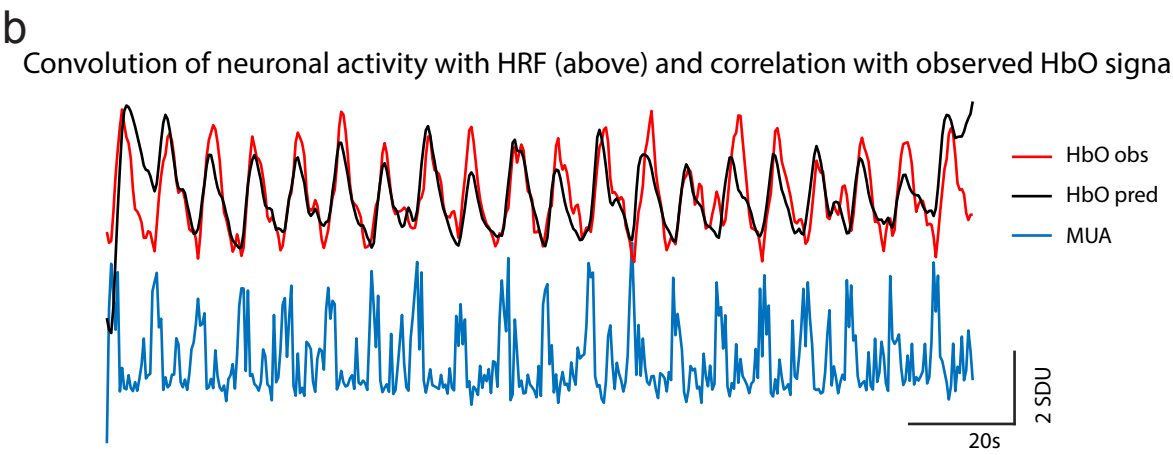

c

Resuts across all band envelopes

coefficient of correlation

(HbO_{Obs}: HbO_{Pred})

	DeltaTheta	Alpha	Spindle	lGam	Gam	hGam	vhGam	MUA
mean	0.0474	0.1174	0.0097	0.2768	0.3122	0.5077	0.4042	0.4796
sem	0.0539	0.0353	0.0481	0.0564	0.0687	0.0500	0.0521	0.0623
*p**	0.3054	0.0061	0.8394	0.0034	0.0012	0.0002	0.0002	0.0002

* Wilcocon's signed rank test

Supplementary figure 6. System identification based HRF estimation and prediction of stimulus induced HbO.
a)The system identification toolbox in Matlab was used to obtain transfer functions (HRFs) between the band-envelope of each LFP band and the HbO signal from recordings of spontaneous activity. Each figure represents the mean HFR for that band.
b) The HRFs were then convolved with each run of stimulus induced activity.
c) The table represents the mean Pearson s coefficient of correlation for each band, along with the standard error and p-value. As can be observed, the higher fre uencies elicited stronger HRFs from the spontaneous activity and also stronger correlations between the predicted and observed HbO during stimulus induced activity.

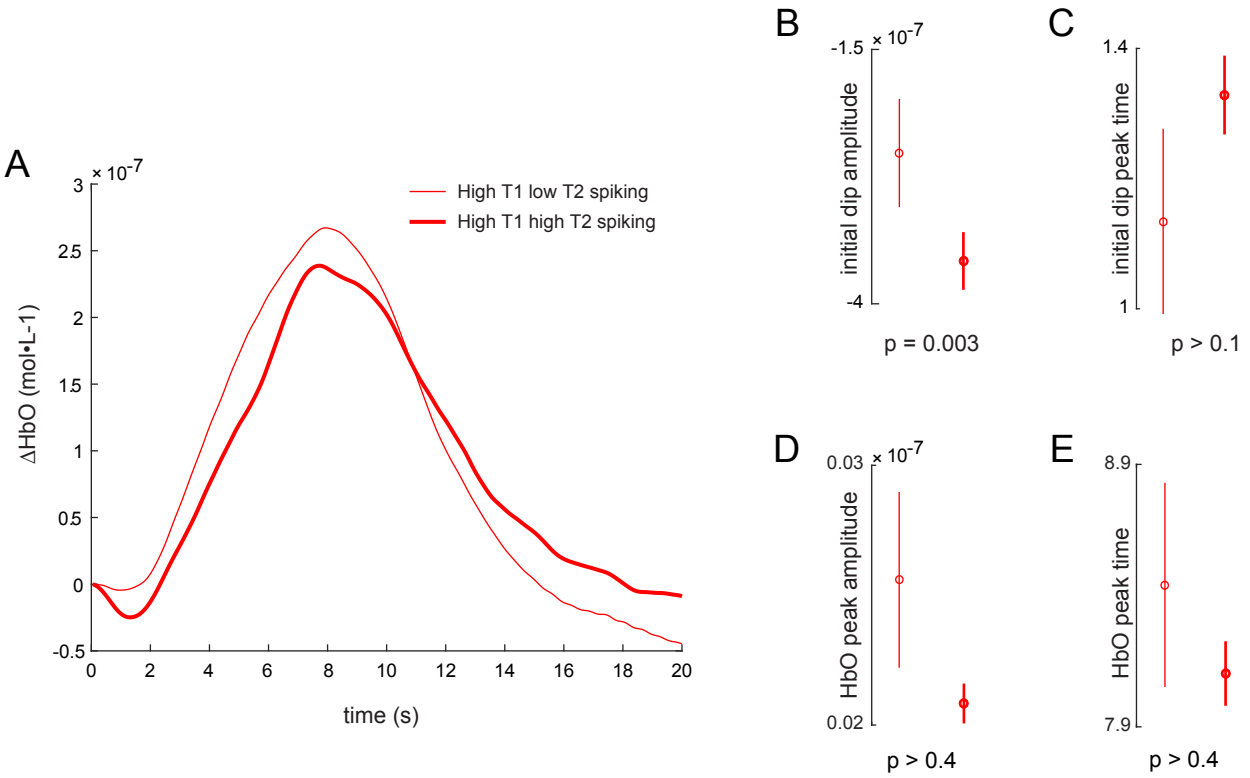

Supplementary figure 7. Larger spread of spike-bursts correspond to larger initial-dip amplitudes.
A) The mean HbO responses for all trials with high spiking on Tetrode 1 and low (thin) and high (thick) spiking on Tetrode 2. As can be clearly observed, the initial-dip is larger for the high-spiking trials (B), without affecting either the initial-dip peak time (C), or the HbO peak amplitude or peak-time (D,E). Interestingly, larger initial dips did not correspond to larger HbO peak-times in this case, demonstrating that the initial-dip does not affect the overall HbO peak-amplitude or peak-time.

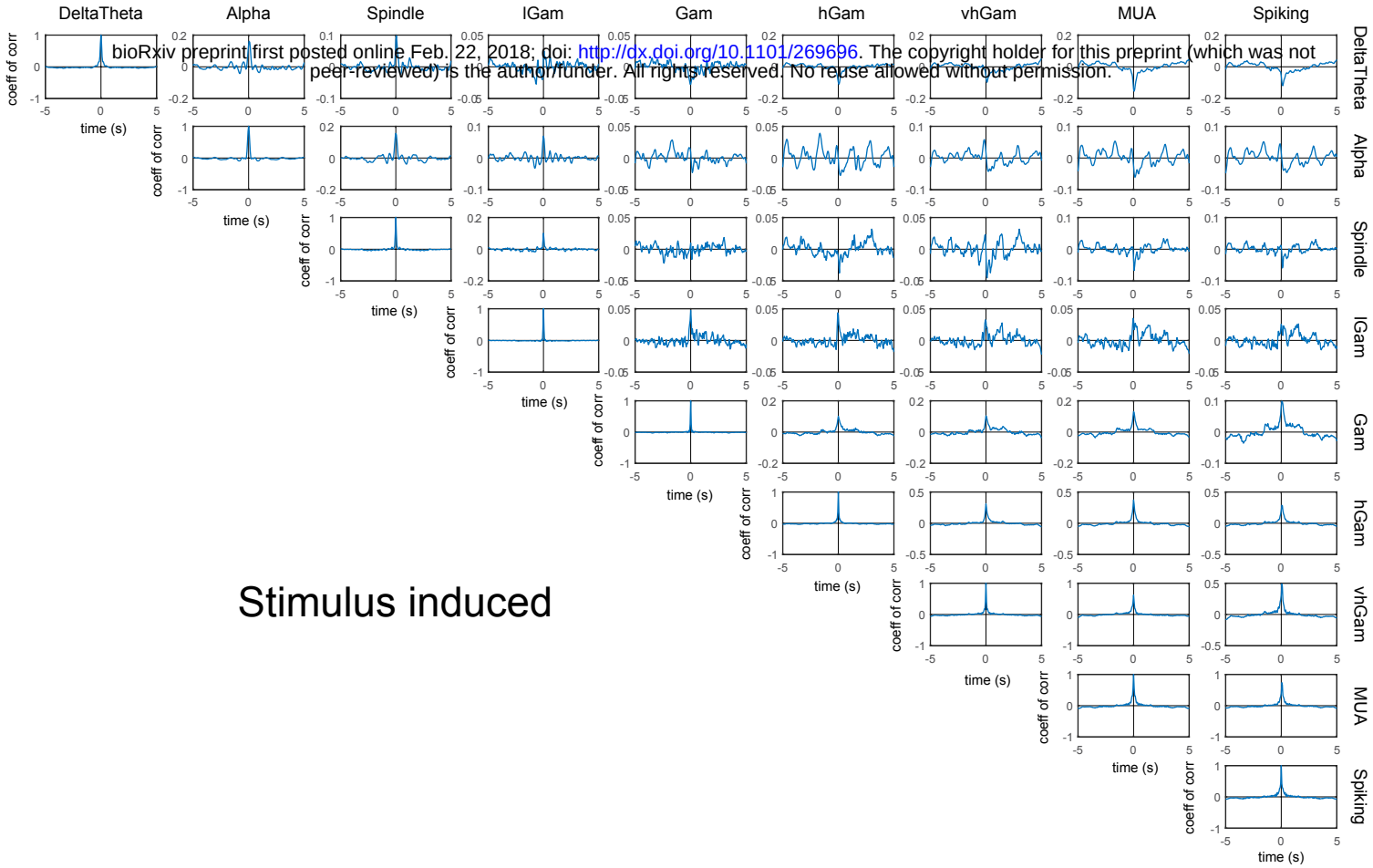

Stimulus induced

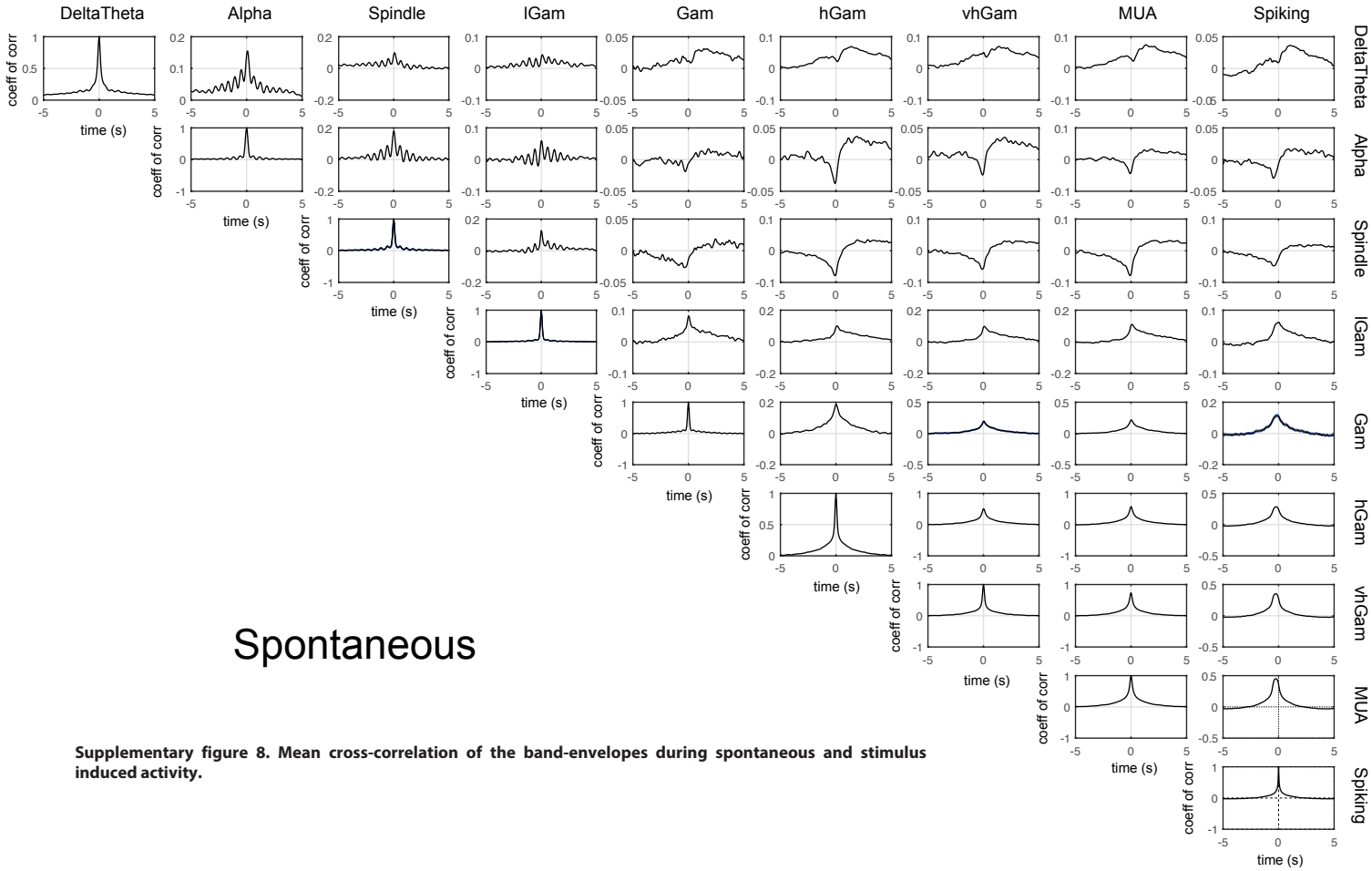

Spontaneous

Supplementary figure 8. Mean cross-correlation of the band-envelopes during spontaneous and stimulus induced activity.

Appendix 3: The hemodynamic initial-dip consists of both volumetric and oxymetric changes correlated to localized spiking activity.

The hemodynamic initial-dip consists of both volumetric and oxymetric changes correlated to localized spiking activity

Ali Danish Zaidi*†[1,2,3], Niels Birbaumer[2,3], Eberhard Fetz[4], Nikos Logothetis[1,5], Ranganatha Sitaram†[2,6]

* Lead contact

† Corresponding authors

Affiliations:
1. Max Planck Institute for Biological Cybernetics, Tübingen, Germany. 2. Institute for Medical Psychology and Behavioral Neurobiology, University of Tübingen, Germany. 3. Wyss Center for Bio and Neuroengineering, Geneva, Switzerland. 4. Department of Physiology and Biophysics and Washington National Primate Research Center, University of Washington, Seattle, USA. 5. Center for Imaging Sciences, Biomedical Imaging Institute, University of Manchester, UK. 6. Institute of Biological and Medical Engineering, and Department of Psychiatry and Section of Neuroscience, Pontificia Universidad Católica de Chile, Santiago, Chile.

Abstract

The "initial-dip" is a transient decrease frequently observed in functional neuroimaging signals, immediately after stimulus onset, and is believed to originate from a rise in deoxy-hemoglobin (HbR) caused by local neural activity. It has been shown to be more spatially specific than the hemodynamic response, and is believed to represent focal neuronal activity. However, despite being observed in various neuroimaging modalities (such as fMRI, fNIRS, etc), its origins are disputed and its neuronal correlates unknown. Here, we show that the initial-dip is dominated by a decrease in total-hemoglobin (HbT). We also find a biphasic response in HbR, with an early decrease and later rebound. However, HbT decreases were always large enough to counter spiking-induced increases in HbR. Moreover, the HbT-dip and HbR-rebound were strongly coupled to highly localized spiking activity. Our results suggest that the HbT-dip helps prevent accumulation of spiking-induced HbR-concentration in capillaries by flushing out HbT, probably by active venule dilation.

Introduction

Functional neuroimaging is a powerful non-invasive tool for studying brain function in health and disease, that uses changes in blood oxygenation as a proxy for estimating local neuronal activity [1]. However, which feature of the hemodynamic signal best reflects local neuronal activity remains an open question. The most commonly used feature is the hemodynamic response amplitude, which is slow and unspecific[1]. Since neuronal processes such as multi-unit spiking are fast, dynamic and spatially localized, a feature in the BOLD signal with similar properties, which also correlates strongly with local neuronal activity, would be an ideal candidate. Early fMRI studies reported such a quick and localized dip in the initial BOLD signal immediately following stimulus onset in various brain areas[2], [3]. This early decrease was termed the 'initial-dip', and was believed to originate from a rise in deoxy-hemoglobin (HbR) caused by stimulus-induced changes in localized neuronal activity[2]. Supporting evidence comes from studies reporting spatially localized dips in tissue partial oxygen pressure[4], [5], and increases in the concentration of HbR [6], observed at the time of the dip. The initial-dip is also more spatially localized than the positive BOLD response [7], and has been used to accurately map orientation columns in the visual cortex (better than the positive-response)[8]. Based on these observations, the initial-dip is believed to represent focal neuronal activity [8]. Although the initial-dip has been observed in various

functional neuroimaging modalities (such as BOLD-fMRI [2], [7], [9], optical imaging [10], [11], fNIRS[12] and pO_2-measurements [4]), its origins are disputed [11] and its precise neuronal correlates are all but entirely unknown.

We recently documented a method for the simultaneous acquisition of epidural fNIRS and intra-cortical electrophysiology in primates (**Fig. 1A-B**), demonstrating that fNIRS has high SNR when acquired epidurally[12], making it ideal for studying local neuro-vascular interactions. FNIRS uses a light-emitter and detector pair (optode pair) to measure changes in concentrations of oxygenated (HbO), deoxygenated (HbR) and total (HbT) hemoglobin, within the vascular compartments in a small volume of tissue[13], [14]. We recorded runs of both spontaneous and stimulus-induced activity in the primary visual cortex of two anesthetized monkeys.

Results

Fig. 1C shows the traces of HbO, HbR, HbT and multi-unit spike-rates for an example run with visual stimulation, consisting of 20 trials. The grey bars mark the 5s of visual stimulation (whole-field rotating chequerboard with high contrast), which were followed by 15 seconds of rest (white spaces). Obvious dips in the HbO signals can be observed on some trials (black arrows). The average traces of these 20 trials elicited observable dips in both HbO and HbT (**Fig. 1D**). We used the mean signal slope between 0 and 1s as a metric of the 'strength' of the initial-dip for each hemodynamic signal, and found that both the HbO and HbT traces had significant dips (**Fig. 1E**). Similarly, in the mean traces of all 260 trials from our dataset, a clear dip in the HbO and HbT signals can be observed, without any changes in HbR (**Fig. 1F-G, Table 1**).

To understand the relationship between neuronal activity and the initial-dip, we divided the 260 trials in our dataset into two groups based on the peak spike-rate during stimulus onset, namely, high-spiking trials (899.96 ± 12.89 spk/s; n=122) and low-spiking trials (497.28 ± 8.35 spk/s; n=125) (**Fig. 2A**). For high-spiking trials we observed strong dips in HbO, HbR and HbT traces. Although the overall distribution of dips in HbO and HbT were not significantly different ($p>0.32$; Wilcoxon's rank-sum test), a trial-by-trial comparison revealed that HbT dips were in fact larger ($p<10^{-5}$, Wilcoxon's signed-rank test; **Fig. 2B-C**). Although low-spiking trials seem to elicit faint modulations in the HbO and HbT signals, we did not observe significant changes in their corresponding slopes ($p<0.1$; **Fig. 2C**). The low-spiking trials themselves, however, had both significantly high peak spike-rates, and strong stimulus-induced spike-rate modulations (**Fig. 2D**). Furthermore, in high-spiking trials, we observed a biphasic response in the slope of HbR traces, which was absent in the low-spiking trials (**Fig. 2E**). The HbR elicited a small but significant dip (between 0-0.75s, epoch I) and a later rebound in the high spiking trials (defined as mean HbR slope between 0.75-1.75s, epoch II, **Fig. 2F**). This illustrates that there is indeed an increase in HbR signal with higher spiking activity.

We next assessed the relationship of the initial-dip with various bands of the local field potential (LFP). We filtered the extra-cellular field potential into eight frequency bands, namely the DeltaTheta (1-8 Hz), Alpha (9-15 Hz), Spindle (15-20 Hz), low-Gamma (lGam, 20-40 Hz), Gamma (Gam, 40-60 Hz), high-Gamma (hGam, 60-100 Hz), very high-Gamma (vGam, 125-300 Hz) and multi-unit activity (MUA, 1-3 kHz) bands, and obtained their respective band envelopes (see Methods for details). From the various LFP bands we analyzed, only peaks in high-frequency bands had a significant correlation with the HbO and HbT dips (**Fig. 2G**). However, the strongest dependence was still observed with peaks in spiking activity for both HbO and HbT dips, with slightly

higher correlations observed with HbT than HbO (**Fig. 2G**, **Fig. S1**). We next determined how this relationship with spiking varied as a function of distance over cortical surface. We obtained the correlations between the HbT dip and the peak spike-rates on the three tetrodes placed between the emitter and detector. We found that the correlation was strongest with the tetrode closest to the emitter, and that it decreased with increasing distance from the emitter ($r = -0.94$; $p < 10^{-4}$, **Fig. 2H**). The results were identical when we used the peak-amplitude of the initial-dip instead of the mean signal slope for both HbO and HbT dips (**Fig. S2**). This finding not only corroborates the idea that the initial-dip is a spatially localized hemodynamic response, but also provides neurovascular evidence that fNIRS has a spatial sampling bias in favor of the emitter, questioning the popular "banana model" that assumes uniform sampling through the volume of tissue between the emitter and detector[13].

It might be argued that stimulus induced activity introduces artificial correlations between the neuronal and hemodynamic responses, by inducing highly synchronous spatio-temporal patterns [15]. To ensure our results didn't arise from such correlations, we analyzed recordings of spontaneous ongoing activity in the absence of visual stimulation, where the monkeys' eyes were closed and covered with thick gauze. **Fig. 3A** shows traces of HbO, HbR, HbT and spike-rates for an example run of spontaneous activity, consisting of 15 minutes. Dips in the HbO and HbT signals can be seen to coincide with strong bursts in spiking activity (**Fig. 3A**, arrows and bars). To analyze the relationship between spiking and hemodynamic signals, we used system identification to estimate the impulse response from spiking to HbO, HbR and HbT traces. This method uses the Wiener-Hopf relationship [16] to estimate the impulse-response to a unit-pulse (1 SDU amplitude, 1s duration at t=0) from the input (spiking activity) on the output (hemodynamic signal), and is independent of the shape and auto-correlation structure of the input. **Fig. 3B** shows the mean impulse-responses from spiking on HbO, HbR and HbT traces. There is an evident dip in the HbO and HbT traces. However, the slopes of these impulse response functions provide a clearer picture of the signal dynamics (**Fig. 3C**), where a decrease in HbO and HbT can be observed at t=1s (**Fig. 3D**; n=48; **Š**), and a late rebound of HbR can be observed at t=2s. We next used the total spike count in each run to separate the runs into high-spiking and low-spiking runs (**Fig. 3E**). **Fig. 3F** shows the impulse-responses obtained for the high-spiking (thick) and low-spiking (thin) runs. The slopes of the impulse-responses show that the high-spiking trials had large, significant dips for all three hemodynamic signals (HbO, HbR and HbT; **Fig. 3G-H**). Furthermore, we found no significant difference between the overall distributions of HbO and HbT dips ($p>0.45$, n=85, Wilcoxon's rank-sum test). However, on trial-by-trial comparison, HbT dips were significantly stronger than HbO-dips (**Fig. 3H**; $p<10^{-4}$, n=85, Wilcoxon's one-tailed signed-rank test). Interestingly, although the low spiking runs seemed to elicit dips as well, they did not reach significance. Furthermore, only the high-spiking runs elicited significant modulations in HbR with both significant dips at t=1s and rebounds at t=2s (**Fig. 3I**). These results are identical to those obtained from the analysis of stimulus induced activity, and are thus independent of the visual stimulation paradigm.

In the analysis of both spontaneous and stimulus-induced activity, we find that the initial-dip is dominated by a decrease in HbT, in trials with strong bursts in spike-rates. However, it might be argued that this decrease in HbT is not an actual change in blood volume, but a consequence arising from signal trends, such as the slope of the hemodynamic signal before stimulus onset, or the choice of analytical parameters, such as the differential path-length factors (DPFs) used for the conversion of optical density to concentration changes (the only parameter-dependent transformation in the analysis). Surprisingly, the strength of the initial-dip

failed to correlate with the mean slope of the hemodynamic signal 0-2s prior to stimulus onset (r=-0.002, p>0.9, Pearson's correlation coefficient of correlation), suggesting that the trend of the hemodynamic signal before the dip fails to affect the initial-dip. We also used various combinations of physiologically relevant DPFs, as reported earlier[6], in the estimation of concentration changes in HbO, HbR and HbT, and obtained identical results (see **Fig. S3**). To be sure, we also analyzed the raw optical density changes for both wavelengths (760nm and 850nm). We found a significant decrease in the optical densities for both chromophores, which was enhanced in high-spiking trials (see **Fig. S4**). The decrease in chromophore concentration at both wavelengths can only be attributed to decreases in total hemoglobin concentration (HbT). Furthermore, within trials with low spiking activity, even though we do not see significant changes in the slope of the HbO and HbR signals, we do find small but significant changes in their concentration (see **Fig. S5**). We detected significant increases in the HbR concentration (mean HbR concentration change between 0 to 0.8s, $p<0.05$, Wilcoxon's signed-rank test) as well as significant decreases in the HbO concentration (see **Fig. S5C**, $p < 0.05$; n=125; Wilcoxon's sign-rank test) but failed to detect significant changes in HbT ($p>0.1$, n=125; Wilcoxon's signed rank test), an observation that is in agreement with previous reports on the initial-dip [6], [17]. Finally, the trials within the lowest quartile of spike-rates elicited neither initial-dips (in HbO, HbR or HbT traces, mean slope between 0-1s), nor changes in concentration (mean concentration change between 0-1s), even though these trials still had significantly high bursts in spike rates (peak rate 300±40 spk/s; $p<10^{-11}$; n=59, Wilcoxon's signed-rank test). These observations demonstrate two different manifestations of the initial-dip. During low-spiking, there is an oxymetric change consisting of an increase in HbR and decrease in HbO concentration. During very high spiking, there is a volumetric change, consisting of a decrease in HbT (and consequently HbO and HbR).

Interestingly, all significant dips detected in optical density traces also translated to changes in hemoglobin concentration, irrespective of the choice of parameters used for converting optical density to concentration change (**see Fig. S3**). Combined with previous studies [6], these results are in conflict with an earlier report where changes in optical density failed to translate to changes in HbO, HbR or HbT signals[11].

Discussion

Although the exact vascular compartments that fNIRS samples from have not yet been firmly established, it is generally believed to reflect oxymetric changes within vessels smaller than 1mm in diameter[14], such as pre-capillary arterioles, capillaries and post-capillary venules (Capillary and Peri-capillary Vessels, henceforth CPVs), which is where most of the oxygen-exchange occurs[18], and hence where the largest changes in blood oxygenation occur. This is exemplified by the increase in HbO and decrease in HbR observed during influx of oxy-saturated blood into CPVs during the positive hemodynamic response (**Fig. 1F**). Thus, even though neuronal activity leads to an increase in HbR concentration, the HbR signal during the positive response decreases, once oxy-saturated blood passes through the CPVs post arteriole dilation. Even the transient increases observed in the HbR signal during the dip only last until the HbT response commences. Hence, a decrease in both HbO and HbR during the initial-dip most likely represents decreases in the blood-volume within CPVs. In our data, the HbO/HbT dip ratio (the ratio of HbO to HbT decrease at maximal dip) is 50.4±17% (mean±sem) for stimulus-induced, and 58.9%±32% for spontaneous activity, which is within the range of oxygen saturation reported within CPVs [18]. A possible means to attain a decrease in CPV blood volume would be through the dilation of post-capillary venules. Post-capillary venules have recently been shown to have band-like smooth muscles encircling

their circumference, similar to those associated with precapillary arterioles [19]. Furthermore, small venules have been shown to increase their diameter simultaneously with strong arteriolar dilations in recordings of spontaneous activity [20]. However, since the primary arterioles that are dilated are further away from the capillaries, the influx of blood takes longer to reach the capillaries. Therefore, upon post-capillary venule dilation, the decrease in capillary blood pressure would briefly compress the capillary, flushing the blood out, before the influx of oxygenated blood caused by arteriole dilation. Recently, erythrocytes have been reported to deform with reduced oxygen tension, facilitating an increase in their flow-rate through the capillary lumen[21], aiding this process. Indeed, a transient increase in capillary RBC velocity can be observed immediately after stimulus onset, which briefly subsides, before finally increasing again (see figures 4B and 4D in 20).

Such a flushing of CPV blood could serve to prevent HbR accumulation in the capillaries, enforcing a virtual "upper-limit" of HbR concentration in the vascular tissue, as well as facilitating the influx of oxygen saturated blood from the arterioles. Indeed, in our data, we found that spiking correlated strongly with the HbR-rebound (**Fig. 4A**). However, the HbT dips were consistently larger than the HbR-rebounds, maintaining an upper-limit of HbR concentration, and hence no relationship was observed between spiking and HbR concentration change between 0.75-1.75s (**Fig. 4B**). Moreover, when corrected for the HbT dip (by subtracting HbT traces from HbR traces), the "dip-corrected" HbR traces reveal increases in concentration that are correlated to spiking activity (**Fig. 4C**). In contrast, no such relationship is observed with "dip-corrected" HbO traces (**Fig.** 4**D**), illustrating that the initial-dip counters rising HbR concentration in the vascular tissue. This deoxygenated blood flushed from individual CPVs would flow into the surface venules, transiently increasing their HbR concentration. Indeed, cortical-depth resolved BOLD-fMRI, believed to reflect changes in tissue HbR [1], [22], reveals that the amplitude of the initial-dip is largest near the cortical surface, in both human [9] and animal [10] studies. Further experiments quantifying changes in HbO and HbR in the various vascular compartments could shed further light on the exact vascular mechanisms of the initial-dip. Nevertheless, our results conclusively demonstrate that the initial-dips in both HbO and HbT traces are strongly correlated with highly localized spiking activity. Furthermore, since we find no relationships between the initial-dip and low-frequency LFP activity, it establishes that the initial-dip is a highly specific marker of localized bursts in spiking activity.

Although we recorded signals from anesthetized monkeys, it has been shown that this anesthesia regime does not significantly alter local neuro-vascular coupling [23]. We also find that fNIRS represents focal neuro-vascular changes close to the emitter, challenging the generally accepted "banana" model that assumes the cortical volume sampled by fNIRS to be uniformly distributed between the emitter and detector [14]. Concurrently, a study comparing simultaneously recorded fNIRS and fMRI signals in humans finds that the voxels correlating best with HbO/HbR changes are consistently closer to the emitter (see Fig. 2 and Table 2 in [24]), though this is not explicitly stated in their results. Overall these results shed further light on the neuro-vascular changes underlying the initial-dip, and enable a better interpretation of functional neuroimaging signals.

In conclusion, we show that the initial dip, though present in both HbO and HbT signals, is dominated by HbT changes that are correlated to highly-localized spiking, demonstrating that these changes are specific to excitatory neuronal activity. This study is, to the best of our knowledge, the first report of an exclusive marker of spiking activity in hemodynamic signals.

Abbreviations

BOLD: blood-oxygen level dependent signal

CPVs: Capillary and Peri-capillary Vessels (precapillary-arterioles, capillaries and post-capillary venules)

fMRI: functional Magnetic Resonance Imaging

fNIRS: functional Near Infra-Red Spectroscopy

HbO: concentration of oxy-hemoglobin

HbR: concentration of deoxy-hemoglobin

HbT: concentration of total hemoglobin

LFP: local field potential

R: Wilcoxon's one-tailed rank-sum test

Š: Wilcoxon's two-tailed signed rank test

T_1: Tetrode 1 (0.55mm from emitter)

T_2: Tetrode 2 (1.75mm from emitter)

T_3: Tetrode 2 (2.95mm from emitter)

Acknowledgements

We would like to thank Matthias Munk, Cristina Risueno and Rebekka Bernard for help during the collection of data, and Mirsat Memej and Eduard Krampe for their help during the design and construction of the recording system, and Vishal Kapoor and Mastaka Watanabe for feedback on an earlier version of the manuscript. We acknowledge funding from the DFG, CIN and Max-Planck Society.

References

[1] N. K. Logothetis, "What we can do and what we cannot do with fMRI.," *Nature*, vol. 453, no. 7197, pp. 869–878, 2008.

[2] X. Hu and E. Yacoub, "The story of the initial dip in fMRI," *Neuroimage*, vol. 62, no. 2, pp. 1103–1108, 2012.

[3] E. Yacoub and X. Hu, "Detection of the Early Decrease in fMRI in the Motor Area," vol. 441, no. 1999, p. 55455, 2000.

[4] A. Parpaleix, Y. G. Houssen, and S. Charpak, "Imaging local neuronal activity by monitoring PO2 transients in capillaries," *Nat. Med.*, vol. 19, no. 2, pp. 241–246, Jan. 2013.

[5] C. Zhang, S. Belanger, P. Pouliot, and F. Lesage, "Measurement of local partial pressure of oxygen in the brain tissue under normoxia and epilepsy with phosphorescence lifetime microscopy," *PLoS One*, vol. 10, no. 8, pp. 1–14, 2015.

[6] G. Jasdzewski, G. Strangman, J. Wagner, K. K. Kwong, R. A. Poldrack, and D. A. Boas, "Differences in the hemodynamic response to event-related motor and visual paradigms as measured by near-infrared spectroscopy," *Neuroimage*, vol. 20, no. 1, pp. 479–488, 2003.

[7] M. Watanabe, A. Bartels, J. H. Macke, Y. Murayama, and N. K. Logothetis, "Temporal Jitter of the BOLD Signal Reveals a Reliable Initial Dip and Improved Spatial Resolution," *Curr. Biol.*, vol. 23, no. 21, pp. 2146–2150, 2013.

[8] D. S. Kim, T. Q. Duong, and S. G. Kim, "High-resolution mapping of iso-orientation columns by fMRI.," *Nat. Neurosci.*, vol. 3, no. 2, pp. 164–169, 2000.

[9] J. C. W. Siero, J. Hendrikse, H. Hoogduin, N. Petridou, P. Luijten, and M. J. Donahue, "Cortical depth dependence of the BOLD initial dip and poststimulus undershoot in human visual cortex at 7 Tesla.," *Magn. Reson. Med.*, vol. 73, no. 6, pp. 2283–95, Jun. 2015.

[10] P. Tian *et al.*, "Cortical depth-specific microvascular dilation underlies laminar differences in blood oxygenation level-dependent functional MRI signal.," *Proc. Natl. Acad. Sci. U. S. A.*, vol. 107, no. 34, pp. 15246–15251, Aug. 2010.

[11] Y. B. Sirotin, E. M. C. Hillman, C. Bordier, and A. Das, "Spatiotemporal precision and hemodynamic mechanism of optical point spreads in alert primates.," *Proc. Natl. Acad. Sci. U. S. A.*, vol. 106, no. 43, pp. 18390–18395, 2009.

[12] A. D. Zaidi *et al.*, "Simultaneous epidural functional near-infrared spectroscopy and cortical electrophysiology as a tool for studying local neurovascular coupling in primates," *Neuroimage*, vol. 120, pp. 394–399, 2015.

[13] A. Villringer, "Non-invasive optical spectroscopy and imaging of human brain function," *Trends Neurosci.*, vol. 20, no. 10, pp. 435–442, Oct. 1997.

[14] M. Ferrari and V. Quaresima, "A brief review on the history of human functional near-infrared spectroscopy (fNIRS) development and fields of application," *Neuroimage*, vol. 63, no. 2, pp. 921–935, 2012.

[15] N. K. Logothetis, J. Pauls, M. Augath, T. Trinath, and a Oeltermann, "Neurophysiological investigation of the basis of the fMRI signal.," *Nature*, vol. 412, no. 6843, pp. 150–157, 2001.
[16] K. J. Keesman, *System identification: an introduction*. Springer Science & Business Media, 2011.
[17] C. Martin, J. Martindale, J. Berwick, and J. Mayhew, "Investigating neural-hemodynamic coupling and the hemodynamic response function in the awake rat," *Neuroimage*, vol. 32, no. 1, pp. 33–48, 2006.
[18] S. Sakadžić *et al.*, "Large arteriolar component of oxygen delivery implies a safe margin of oxygen supply to cerebral tissue," *Nat. Commun.*, vol. 5, p. 5734, 2014.
[19] R. A. Hill, L. Tong, P. Yuan, S. Murikinati, S. Gupta, and J. Grutzendler, "Regional Blood Flow in the Normal and Ischemic Brain Is Controlled by Arteriolar Smooth Muscle Cell Contractility and Not by Capillary Pericytes," *Neuron*, vol. 87, no. 1, pp. 95–110, 2015.
[20] P. J. Drew, A. Y. Shih, and D. Kleinfeld, "Fluctuating and sensory-induced vasodynamics in rodent cortex extend arteriole capacity.," *Proc. Natl. Acad. Sci. U. S. A.*, vol. 108, no. 20, pp. 8473–8478, May 2011.
[21] H. Wei *et al.*, "Erythrocytes Are Oxygen-Sensing Regulators of the Cerebral Microcirculation," *Neuron*, vol. 91, no. 4, pp. 851–862, Aug. 2016.
[22] S. A. Huettel, A. W. Song, and G. McCarthy, *Functional magnetic resonance imaging*. 2014.
[23] J. B. M. Goense and N. K. Logothetis, "Neurophysiology of the BOLD fMRI Signal in Awake Monkeys," *Curr. Biol.*, vol. 18, no. 9, pp. 631–640, 2008.
[24] X. Cui, S. Bray, D. M. Bryant, G. H. Glover, and A. L. Reiss, "A quantitative comparison of NIRS and fMRI across multiple cognitive tasks," *Neuroimage*, vol. 54, no. 4, pp. 2808–2821, 2011.

Methods

Surgery and craniotomy

Two healthy adult monkeys, M1 (female; 8 kg) and M2 (male; 10 kg), were used for the experiments. All vital parameters were monitored during anesthesia. After sedation of the animals using ketamine (15 mg/kg), anesthesia was initiated with fentanyl (31 µg/kg), thiopental (5 mg/kg), and succinylcholine chloride (3 mg/kg), and then the animals were intubated and ventilated. A Servo Ventilator 900C (Siemens, Germany) was used for ventilation, with respiration parameters adjusted to each animal's age and weight. Anesthesia was maintained using remifentanil (0.2–1 µg/kg/min) and mivacurium chloride (4–7 mg/kg/h). An iso-osmotic solution (Jonosteril, Fresenius Kabi, Germany) was infused at a rate of 10 ml/kg/h. During the entire experiment, each animal's body temperature was maintained between 38.5 °C and 39.5 °C, and SpO2 was maintained above 95%. Under anesthesia, a craniotomy was made on the left hemisphere of the skull to access the primary visual cortex. During each experiment, the bone was removed to create a rectangular slit measuring 3 mm anterio-posteriorly and 20 mm medio-laterally, exposing the dura. Connective tissue, if present above the dura, was carefully removed. For each monkey, at least two weeks were allowed to pass between successive experiments. All protocols were approved by the local authorities (Regierungspräsidium, Tübingen) and are in agreement with European guidelines for the ethical treatment of laboratory animals.

Near-infrared Spectroscopy

We used a NIRScout machine purchased from NIRx Medizintechnik GmbH, Berlin. The system performs dual wavelength LED light-based spectroscopic measurements. The wavelengths used were 760nm and 850nm, with a maximum of 5µW effective power at the emitter end. Sampling was performed at 20Hz. We used modified emitters and detectors, and optical fiber bundles for sending the light from the LED source into the tissue, and also for detecting refracted light from the tissue. The fiber bundles were ordered from NIRx Medizintechnik GmbH, Berlin, Germany. Both the emitter and detector fiber bundles had iron ferrule tips with an aperture of 2.5mm on the ends that touched the dura. We used three optodes in a linear arrangement separated by 6mm each. Three tetrodes and single-wire electrodes each were added between each pair of adjacent optodes. We used the central optode as a constant detector, and alternated the peripheral optodes during sessions, such that on a given experimental day, 50% of data came from one emitter-detector pair and 50% from the other. The recording instrument was connected via USB to a laptop computer running an interactive software called NIRStar provided along with the instrument. The software was used for starting and stopping recordings, and also for setting up the various parameters, such as, the number of sources and detectors, and the sampling rate. The instrument

received TTL pulses from the stimulus system and the electrophysiological recording system, for synchronization purposes. The system sent 1ms TTL pulses every 50ms to the recording system that corresponded to light pulses.

Electrophysiology

Custom built tetrodes and electrodes were used. All tetrodes and single electrodes had impedance values less than 1 MΩ. The impedance of each channel was noted before loading the tetrodes on to the drive, and once again while unloading the tetrode after the experiment, to ensure that the contacts were intact throughout the duration of the experiment. To drive the electrodes into the brain a 64-channel Eckhorn matrix was used (Thomas Recording GmbH, Giessen, Germany). The electrodes were loaded in guide tubes a day before the experiment. On the day of the experiment, the tetrodes were driven using a software interface provided by Thomas Recording GmbH, Giessen, Germany. The output was connected to a speaker and an oscilloscope, with a switch to help cycle between different channels. We advanced electrodes into the cortex one by one until we heard a reliable population response to a rotating checkerboard flickering at 0.5Hz.

Spontaneous activity

For each run, spontaneous activity was recorded for 15 minutes, in the absence of visual stimulation. The eyes of the monkey were closed and thick cotton gauze was used to cover the eyelids.

Visual stimulation

A fundus camera was used to locate the fovea for each eye. For presenting visual stimulation, a fiber optic system (Avotec, Silent Vision, USA) was positioned in front of each eye, so as to be centered on the fovea. To adjust the plane of focus, contact lenses (hard PMMA lenses, Wöhlk, Kiel, Germany) were inserted to the monkey's eyes. We used whole-field, rotating chequerboard to drive the neural activity. The direction of rotation was reversed every second. Each trial consisted of 5 seconds of visual stimulation followed by 15 seconds of a dark screen. A single run consisted of 20 trials. Data presented are from 13 runs spread over 8 experimental days.

Signal processing and data analysis

All analyses were performed in MATLAB using custom written code. Only runs that cleared visual screening for artifacts were used. Data points that were larger than 5 SDU were excluded from the analysis, so as to avoid tail-effects for correlation analysis. Normality for each distribution was confirmed before analysis was performed.

FNIRS signal processing

The raw wavelength absorption data from the NIRS system was converted to concentration changes of [HbO] and [HbR] using a modified Beer-Lambert equation (DPF = 6,6). For correlating hemodynamic signals with neural activity, the signals were filtered between 0.01 and 1 Hz to remove any low frequency drifts. For a trial-by-trial analysis, the hemodynamic response for each trial was zero-corrected by subtracting, from each hemodynamic response, the value at the start of the trial.

Electrophysiological signal processing

The extracellular field potential signal was recorded at 20.8333 kHz and digitized using a 16-bit AD converted. From the raw signal, eight frequency bands (namely, DeltaTheta (1-8 Hz), Alpha (9-15 Hz), Spindle (15-20 Hz), low Gamma (20-40 Hz), Gamma (40-60 Hz), high Gamma (60-120 Hz), very high Gamma (120-250 Hz) and MUA (1-3 kHz)) were band-pass filtered using a 10^{th} order Butterworth filter. The envelope for each band was then obtained by taking the absolute value of the Hilbert transform of the filtered signal. The band-envelope was then converted to standard deviation units by subtracting the mean and dividing by the standard deviation of the signal. This signal was then resampled at 20 Hz, to allow comparisons with hemodynamic signals.

Spike rates were obtained by detecting peaks in the MUA signal larger than a threshold (2 SDU), and by counting the threshold-crossing events in 50ms bins. Varying the detection threshold between 2, 3 or 4 SDU did not affect the results.

System identification based impulse response estimation in spontaneous activity

Impulse response functions from spiking to HbO, HbR and HbT were obtained using the system identification toolbox in Matlab.

Each hemodynamic signal was first filtered between 0.01 to 1Hz and then normalized by subtracting the mean and dividing by the standard deviation. Spike-counts were obtained by counting the number of threshold crosses (>3 SDU) in the 1-3kHz band in 50ms bins. The bin-count was then divided by the length of the time window to obtain spike rates in spikes/s. Each spike-rate trace was then smoothened by convolving with a Gaussian function of unit amplitude and 100ms standard deviation. The 900s (15 min) recordings were divided into four epochs of 225s each. All signals were then decimated to 1Hz to enable processing with the toolbox.

For estimating the impulse response function for each epoch, the spike-rate for that epoch was used as the input and the hemodynamic signal as output.

Calculation of modulation indices

The 'On' epoch for each trial was defined as the time from 0 to 5.05 seconds. The extra 0.05s were added to accommodate for the off response. The 'Off' epoch was defined as the time between 5.05 to 10.05 seconds. The modulation index (MI) was then calculated using the formula: neural modulation = $(SR_{On}-SR_{Off}) / (SR_{On}+SR_{Off})$; where SR_{On} is the mean spike-rate during Stim On, and SR_{Off} is the mean spike-rate during Stim Off for each trial. Runs without significant visual modulation of spike-rates were excluded from the analysis.

Statistics

All distributions were confirmed to be normally distributed using the Kolmogorov-Smirnov test in Matlab, before using means as a measure of central tendency. All correlation coefficients represent Pearson's correlation coefficient and corresponding significance values. To calculate the correlations, the trials were sorted and divided into 10 bins (with 26 trials per bin). The mean values of each bin were then correlated. This was done to avoid an otherwise large trial-by-trial variation. The results were independent of the number of bins used for correlation analysis (see Fig. S1)

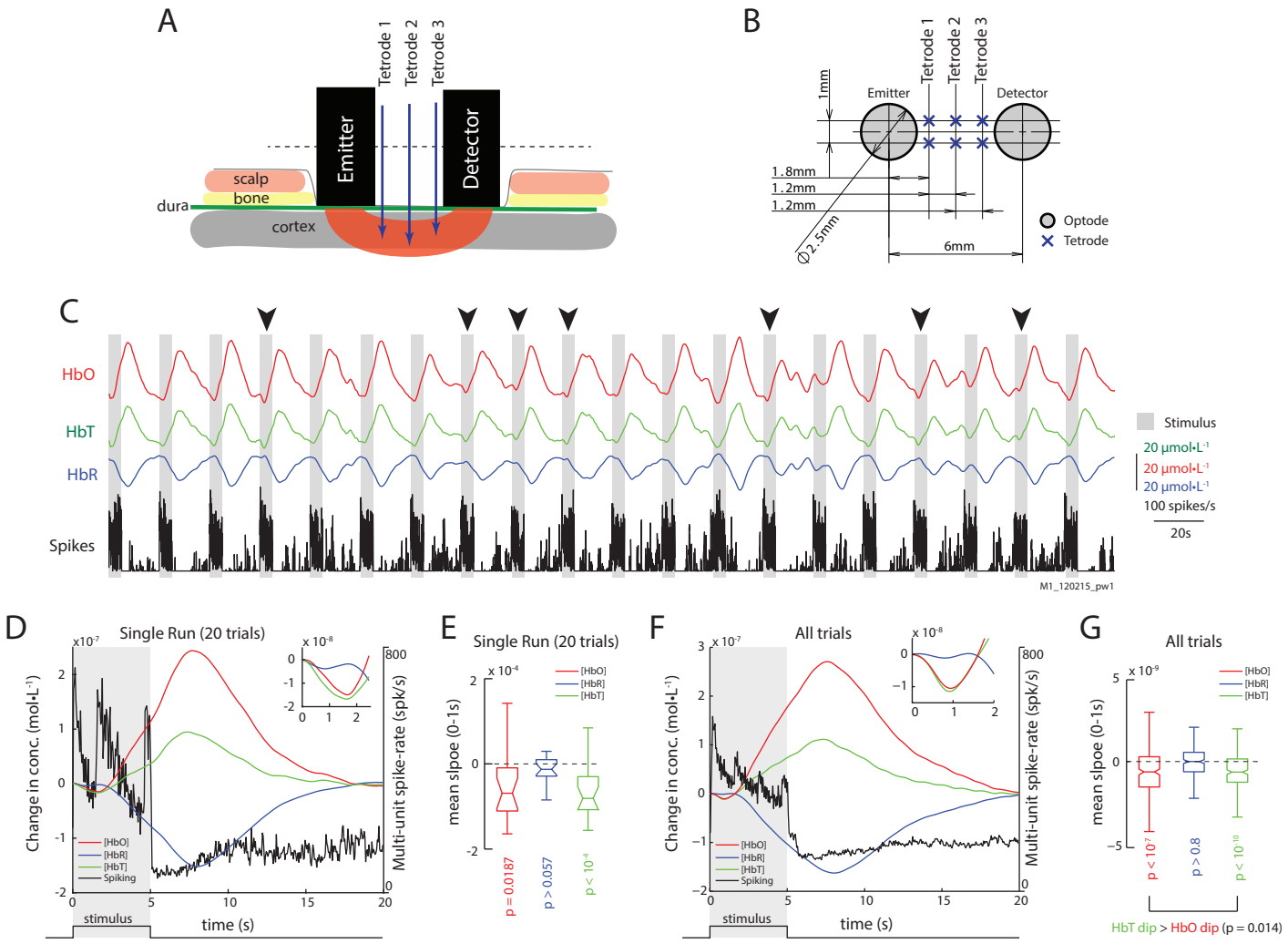

Figure 1. Epidurally measured fNIRS measurements reveal initial dips in hemodynamic signals. A) Illustration of the sensor array with placement of fNIRS optodes and electrodes relative to scalp and brain tissue. B) Transverse section of the sensor array with distances between optodes and electrodes. See methods for details. C) Traces of HbO, HbR, and Spiking from an example run with 20 trials. Grey bars represent epochs of visual stimulation. Arrows mark trials where initial dips are obvious in signal trends. D) The mean traces of HbO, HbR, HbT and multi-unit spiking (units on the right) for trials shown in (C). Inset) Same hemodynamic traces, but from 0-2.5s. The initial dip is observed in the HbO and HbT (inset), but not in the HbR traces. The shaded region represents visual stimulus presentation. E) Distribution of slopes from 0-1s for HbO, HbR and HbT traces for trials in (C). The distributions of HbO and HbT slopes are less than zero, but not for those for HbR (p_{HbO}=0.0187; $p_{HbT}<10^{-4}$; p_{HbR}=0.099; n=20; Š). F) The mean traces of HbO, HbR, HbT and multi-unit spiking activity (units on the right) for all trials. Inset) Same hemodynamic traces, but from 0-2s. G) Distribution of signal slopes from 0-1s for HbO, HbR and HbT traces for all trials. The distributions for HbO and HbT are less than zero, but not for HbR ($p_{HbO}<10^{-7}$; $p_{HbT}<10^{-10}$; $p_{HbR}>0.1$; n=260; Š). However, HbT dips were stronger than HbO dips (p = 0.028; Ś)

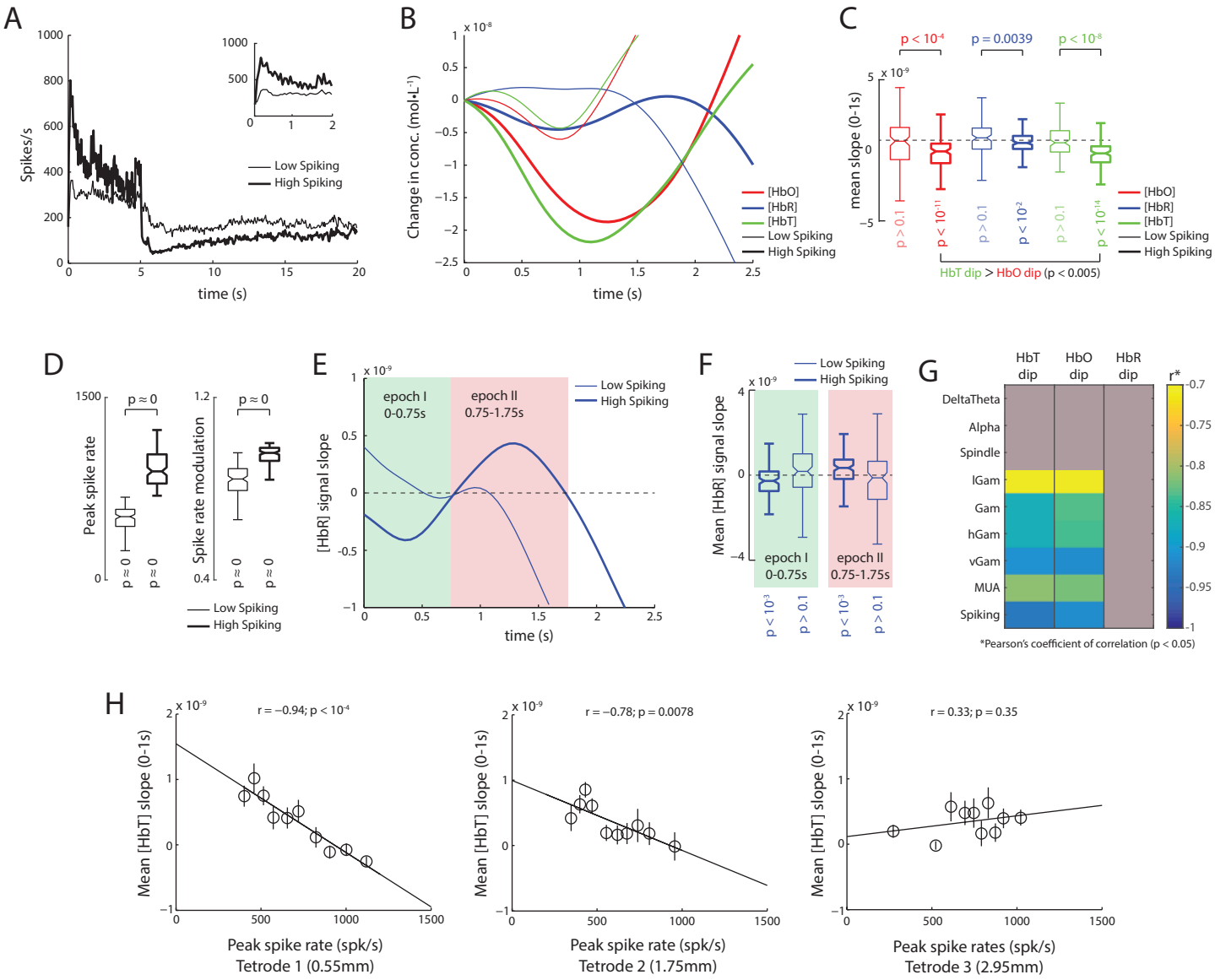

Figure 2. Trials with high spiking activity reveal initial dips comprise of an early HbT decrease, and late HbR increase. A) Mean traces of spike-rates for trials with high and low spiking immediately after stimulus onset (thick and thin traces, respectively). Inset) Same traces, but between 0-2s. B) Mean traces of hemodynamic signals for trials with low (thin) and high spiking as shown in (A). A clear increase in the dips is observed for high spiking trials with the largest dips elicited in HbT traces. C) Average slopes from 0-1s for HbO, HbR and HbT traces for high (thick) and low (thin) spiking trials. HbO, HbR and HbT all elicit significant dips in high-spiking trials ($p_{HbO}<10^{-11}$; $p_{HbT}<10^{-14}$; $p_{HbR}<10^{-2}$; n=128; Š), with larger dips in HbT than HbO (p<0.005; n=125; pairwise Ś). Interestingly, trials with low spiking trials do not elicit significant dips in either HbO, HbR or HbT (p<0.1; n=122; Š). D) Distribution of peak spike-rates and visual modulation of spike-rates for trials with high (thick) and low (thin) peak spike-rates. This illustrates that even though the peak rates were lower in the low-spiking trials, the overall spiking activity was significantly high, as was the visual stimulus induced modulation of spike rates (see Methods for calculation of modulation index). E) Analysis of the slope of HbR traces in high spiking trials reveals a biphasic response, which is almost all but absent in low spiking trials. In high spiking trials (thick trace), an initial negative slope is observed roughly between 0-0.75s (epoch I, shaded green), followed a positive slope roughly between 0.75-1.75s (epoch II, shaded red). F) For high spiking trials, the distribution of mean HbR slopes were significantly negative during epoch I ($p<10^{-3}$; n=125; Š), and significantly positive during epoch II ($p<10^{-3}$; n=125; Š). In contrast, low spiking trials showed no significant modulation of HbR slopes during either epoch I or II (p>0.1; n=122; Š). G) Correlation of mean dips in HbT, HbO and HbR stimulus induced peaks in the power of various LFP frequencies bands and Spiking. Correlations with p>0.05 are greyed. Only high frequency bands showed a significant correlation with initial dips, with spiking activity eliciting the strongest relationship, that were marginally higher for HbT than HbO. H) Strength of the relationship between the HbT dip and spiking activity decreases with distance from the NIRS emitter. Strongest correlations are observed on tetrode closest to emitter (0.55mm away from emitter edge, 1.8mm from emitter center), whereas no correlations are observed on tetrode 2.95mm away (4.2mm from center).

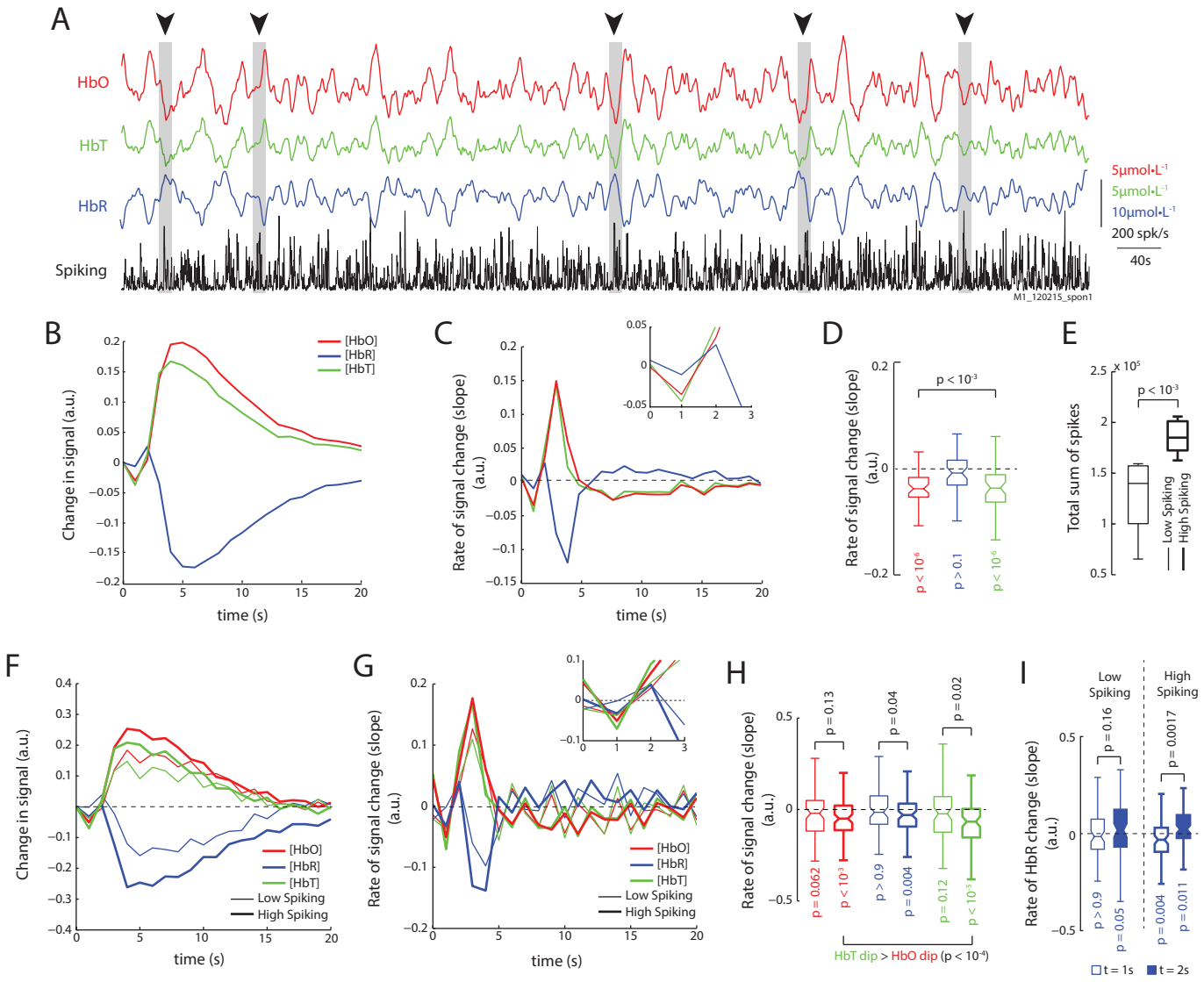

Figure 3. Analysis of spontaneous activity in the absence of visual stimulation reveals identical relationships. A) Traces of HbO, HbR, HbT and spike-rates from an example run of 900s. Periods of high spiking activity that elicit an observable dip in HbO and HbT are marked with arrows and grey bars. B) We used system identification to estimate the impulse response functions from spiking to HbO, HbR and HbT signals in recordings of spontaneous activity. The mean impulse response reveals a dip in HbO and HbT (mean of 48 impulse response functions obtained from 16 runs lasting 900s each; see Methods for details). C) Rate of change of the impulse response functions for HbO, HbR and HbT reveals dips in both HbO and HbT, and a late rise in the HbR. Inset) Same traces but between 0 to 3s. D) Distribution of slopes for HbO, HbR and HbT at t=1s. Only HbO and HbT have significant dips, but not HbR (Š; n=48). E) The runs were divided based on the total sum of spikes in each run, and seperated into low spiking and high spiking runs. High spiking runs had signficanlty higher spike sums (Ś; n=8). F) The mean impulse responses for high and low spiking runs reveal stronger modulation of hemodynamic signals on high spiking trials. Color-code same in following figures G) Mean traces of slopes of impulse responses shown in F. High spiking trials elicit an obvious dip at t=1s. Inset) Same traces but from 0 to 3s. H) Distribution of dips for low and hihg spiking trials (legend same as F). Only high spiking trials have significant dips in all three signlas. Also, HbT dips were larger than HbO dips (Ś; n=80). I) When comparing the HbR dip and rebound at t=1s and t=2s resp., only high spiking trials reveal a strong dip and rebound in the HbR signal.

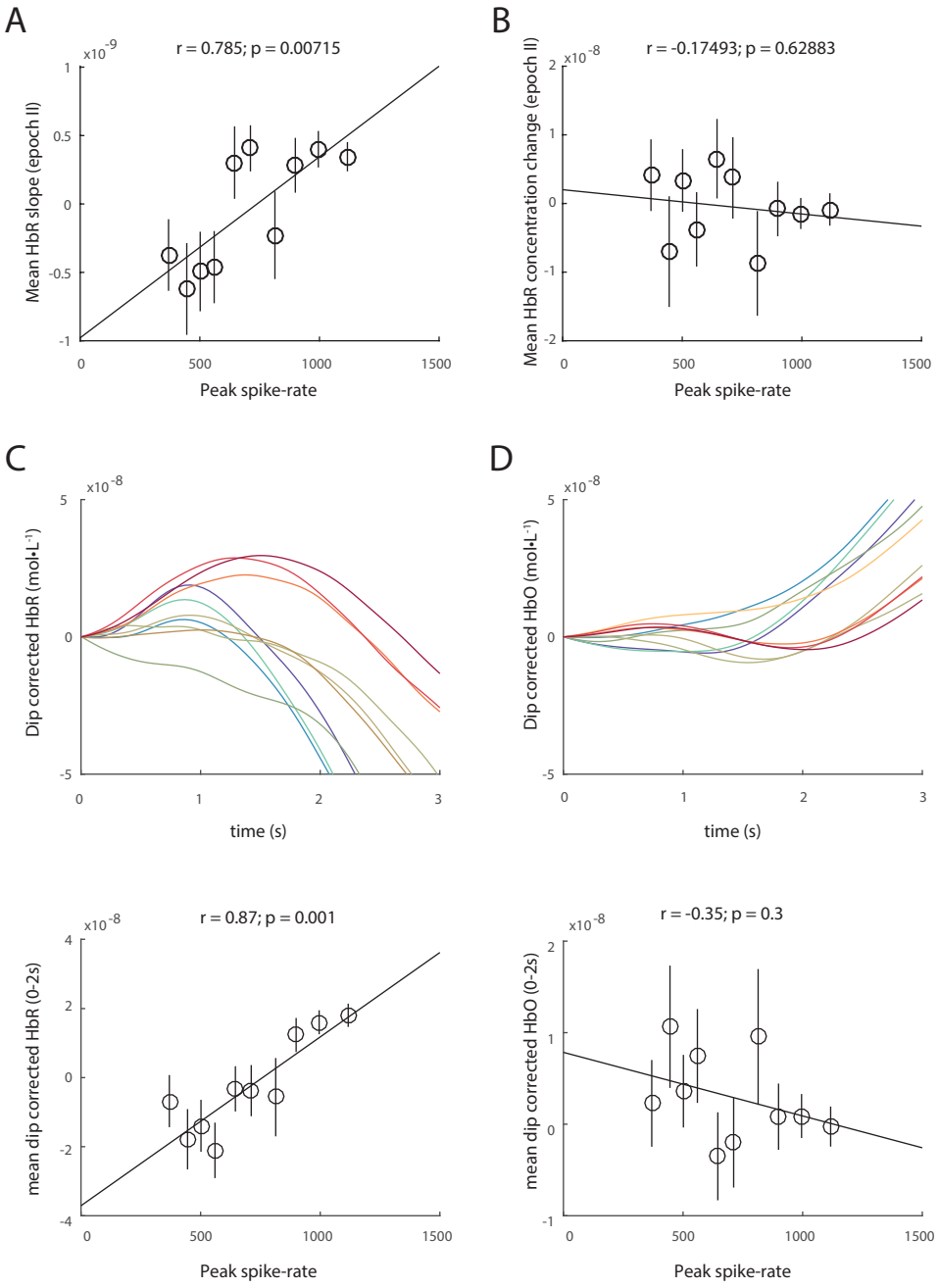

Figure 4. HbR-rebound does not lead to increase in HbR concentration. Although there is a significant correlation between spiking and the mean HbR slope in epoch II (A), the relative HbR concentration change remains unchanged with spiking (B). C) Dip-corrected HbR traces, obtained by imply subtracting the HbT traces from HbR reveals obvious increases in HbR concentration that correlate with spiking. However, no such relationship is observed with dip-corrected HbO traces.

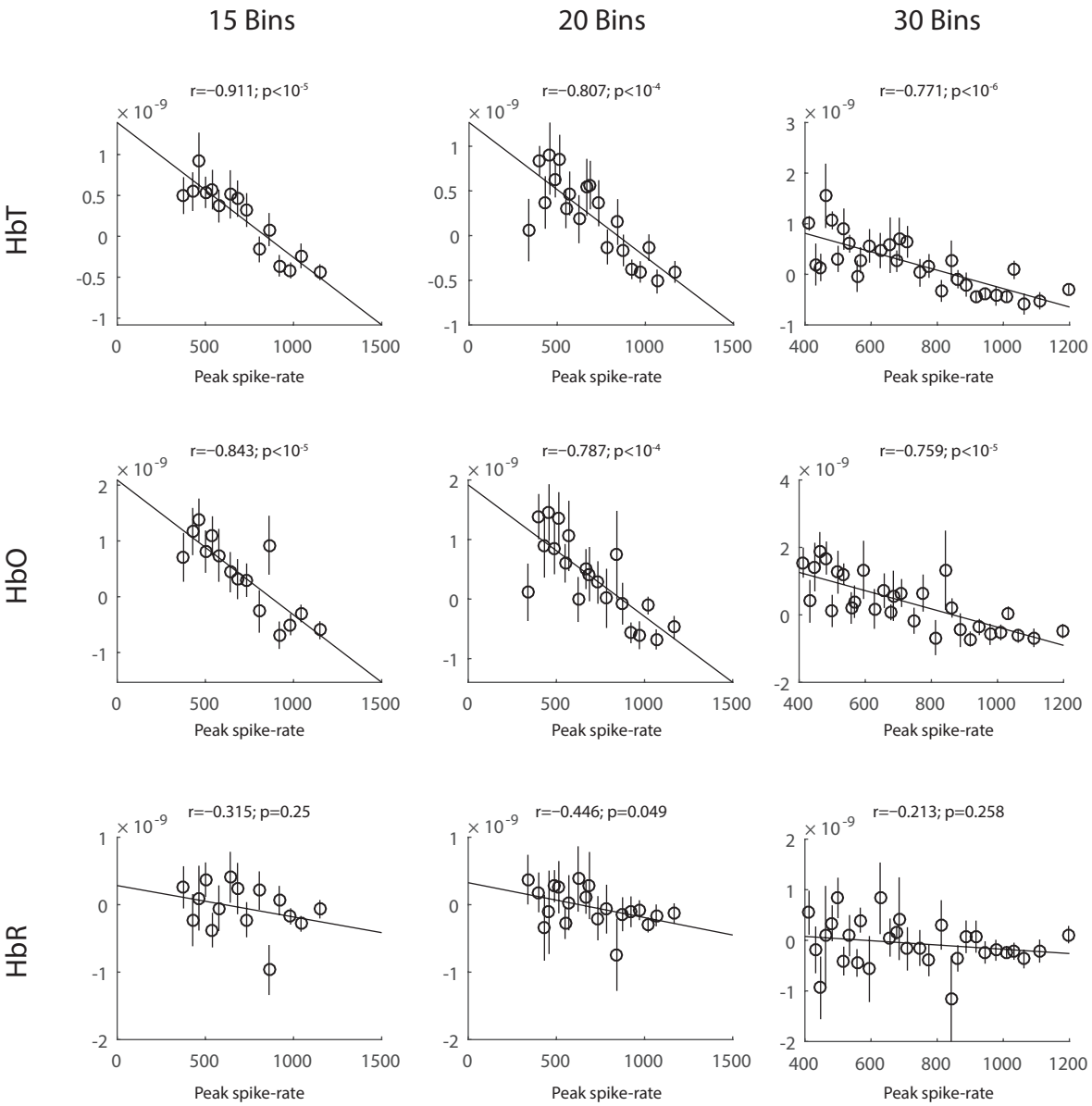

Figure S1. Related to Figure 1. Correlations of spiking activity with HbT, HbO and HbR dips are independent of binsize. Although both HbT and HbO dips showed strong correlations with peaks in spike-rates, the correlations with HbT were stronger than HbO. Although the strength of the correlations got weaker with increasing the number of bins, the significance was not very different. No correlations were observed with the dip strength in HbR. These correlations were independent of the number of groups the data were divided into.

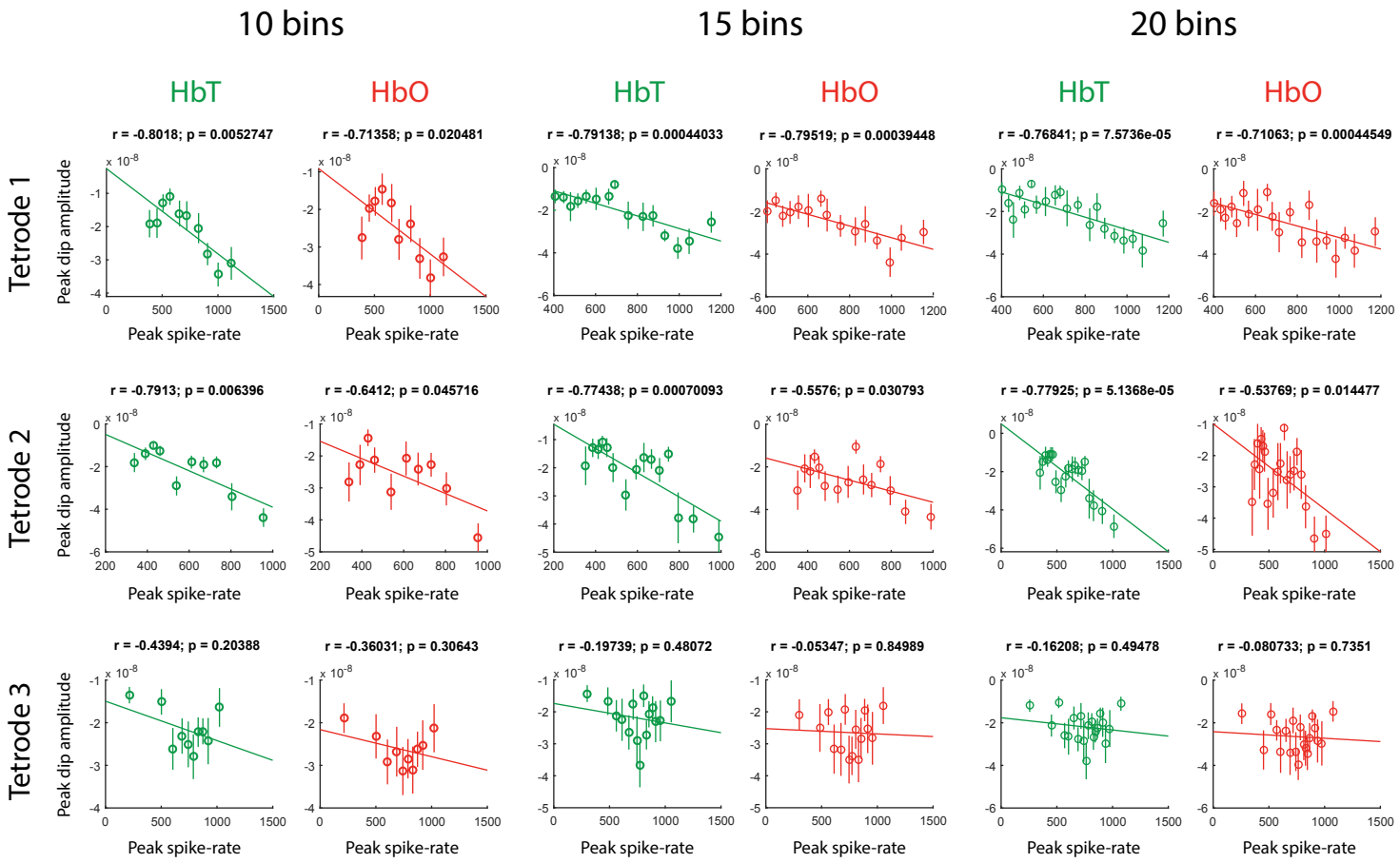

Figure S2. Related to Figure 1. Correlations between peak amplitude of inital dip and peak spike-rates across tetrodes. Instead of using the mean slope between 0-1s, we used the peak dip amplitude (minimum signal value between 0 and 3s) for HbT and HbO and correlated it with the peak spike-rate. We found that the correlations of peak dip amplitude with peak spike-rates were strongest on the tetrode closest to the emitter, and decreased with increasing distance of tetrode from emitter (see figure 2H for comparison). These results were independent of the number of bins the trials were divided into. These results demonstrate that both HbO and HbT dip amplitudes can be used a proxy for underlying spiking activity.

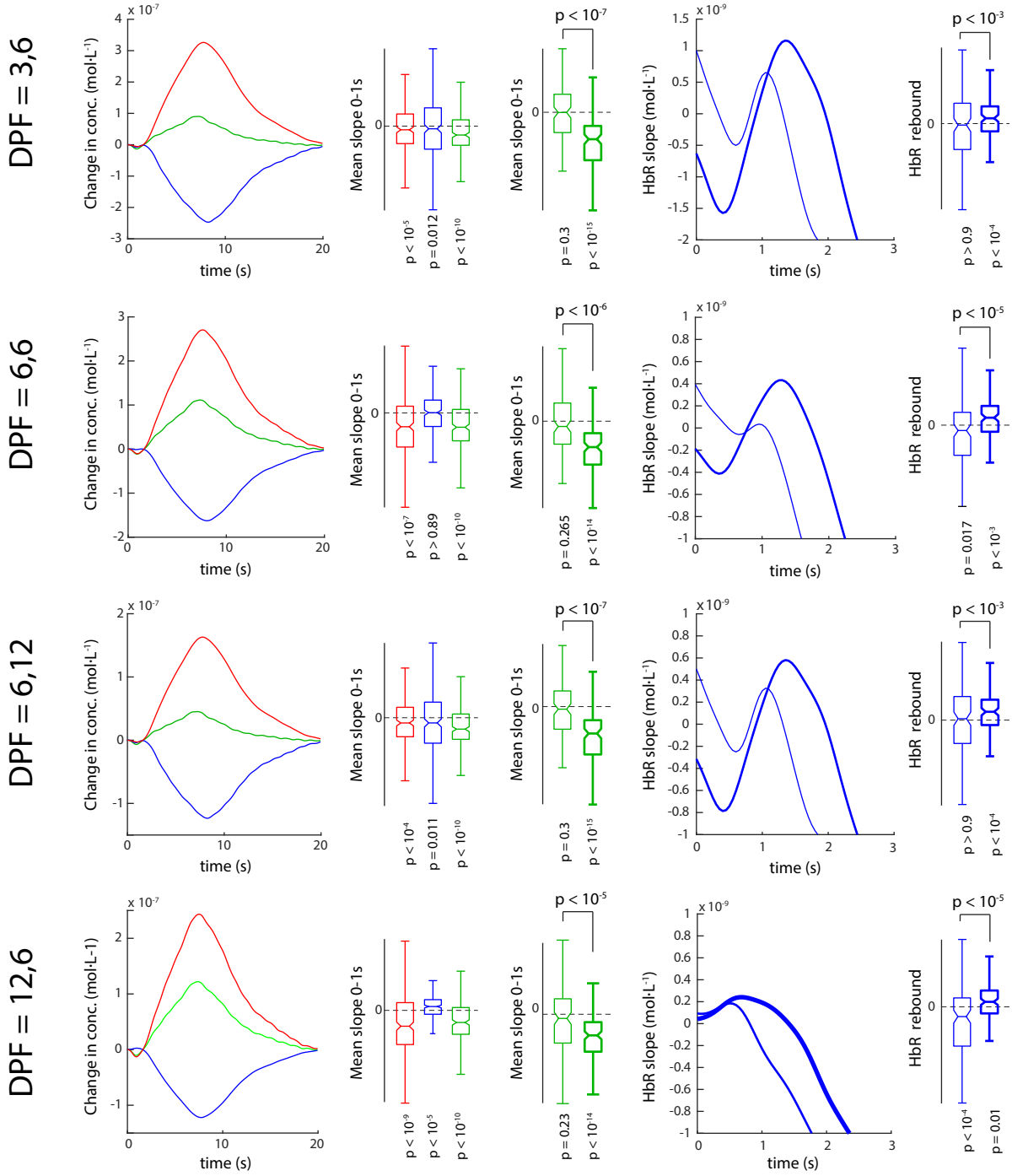

Figure S3. Verification of results across various differential path length factors (DPF). The conversion of optical density to concentration may vary based on the choice of DPF[1]. To ensure that our results did not depend on the DPF, we used multiple combinations of physiologically relevant DPF as reported earlier[1] (the pair of values represent the DPFs at 760 and 850nm resp.) and found that although different DPFs lead to a change in the amplitude of the signals, the overall results were not affected. For each combination of DPFs, we observed strong dips in the HbO and HbT signals. We also observed an increase in the dip strength for HbT during high spiking trials. Low spiking trials failed to elicit a significant dip. The HbR signal also elicited a strong dip and rebound modulation in each case. For each combination of DPFs, the results were nearly identical and individually significant.
Interestingly, the DFP combination 12,6 revealed increases in HbR within the 0-2s of trial onset. However, there was no difference in HbR concentration in high-spiking vs low-spiking trials ($p>0.4$; n=130/group, Wilcoxon rank-sum test). Furthermore, the strongest difference between high and low-spiking was still oberved in the HbT-dip ($p<10^{-5}$) than HbO-dip ($p<10^{-3}$).
This reaffirms previous results[1] that, at least in the primary visual cortex, although the choice of DPF might alter the amplitude of the calculated change in concentrations of HbO, HbR and HbT, it does not alter their relationship to underlying spiking activity. Notches represent 95% confidence intervals.

1. Jasdzewski, G., Strangman, G., Wagner, J., Kwong, K.K., Poldrack, R.A. and Boas, D.A., 2003. Differences in the hemodynamic response to event-related motor and visual paradigms as measured by near-infrared spectroscopy. Neuroimage, 20(1), pp.479-488.

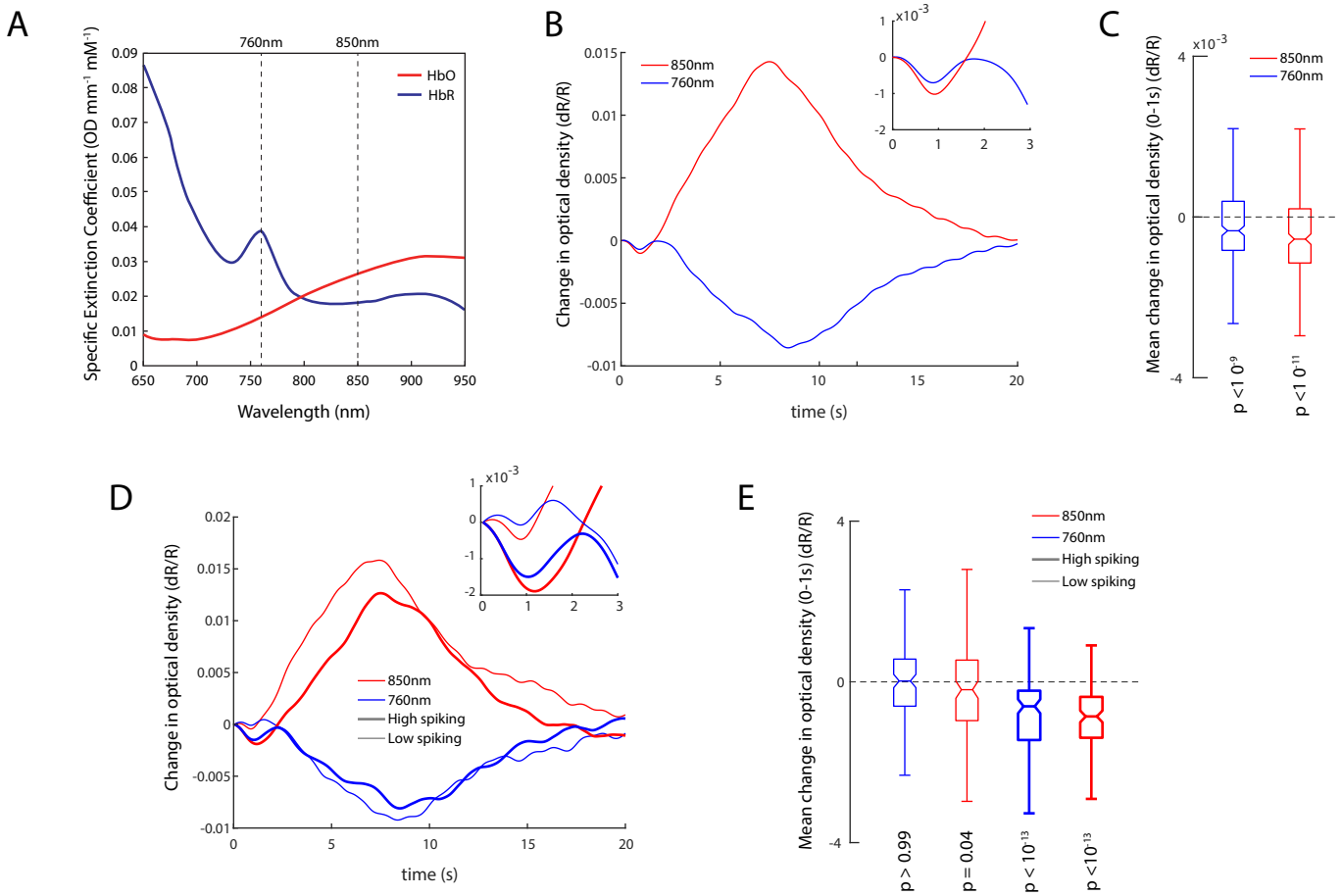

Figure S4. Changes in optical density for both imaging wavelenghts (760nm and 850nm) reveal an early decrease in chromophore concentration. A) Specific extinction coefficients for HbO and HbR as a function of wavelength. Although both HbO and HbR absorb light at both wavelengths, 760nm is more sensitive to HbR changes whereas 850nm is more sensitive to HbO changes. Changes in the observed optical density are proportional to changes in the chromatophores according to Beer's law. B) Mean changes in the optical densities at 760nm and 850nm across all 260 trials. Inset represents the changes between 0-3s. A decrease in optical density for both wavelenghts can be observed. C) Mean change in optical density between 0 and 1s for 760 and 850nm. The distributions are significanlty less than zero. D) Optical density changes for trials with high and low spiking activity. Inset represents the changes between 0-3s. Larger decreases in optical density are observed for the high spiking trials. E) Mean changes in optical density between 0-1s reveal significant decreases in optical density for high-spiking trials. The decrease in optical density for both chromatophores implies a decrease in both HbO and HbR concentrations. Since HbT is the sum of changes in HbO and HbR, simultaneous decreases in HbO and HbR would lead to larger decreases in HbT when changes in optical density are converted to changes in concentration. Surprisingly, we found mildly significant decreases i n the optical density at 850nm for low-spiking trials. However, after conversion to concentration changes, none of the traces (HbO, HbR or HbT) revealed significant changes between 0-1s.

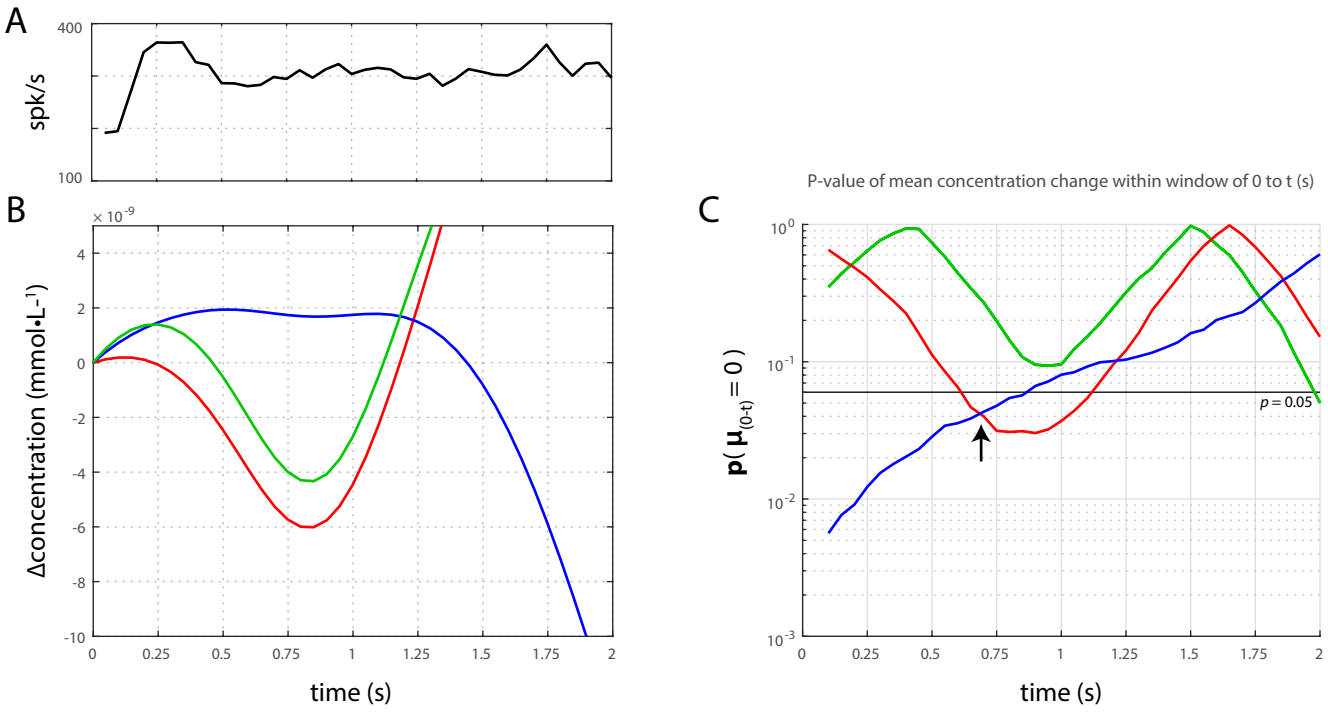

Figure S5. Further analysis of low-spiking trials reveals a significant increase in HbR and decrease in HbO concentrations within the first 750ms. We further analyzed trials where the peak spike-rate was less than the median value of all trials (**A**, see also Figure 2A). Although these trials belonged to the lower half of the distribution, they still had significantly high peak spike-rates and stimulus induced spike-rate moduations (see Fig. 2D). We obtained the mean HbO, HbR and HbT traces from these trials (**B**). Increases in HbR traces and decreases in the HbO traces are clearly observable within these trials. We determined the temporal window within which these changes were significant, by incrementing the width of the window from 0 to 2s (**C**, $p<0.05$ based on the Wilcoxon signed-rank test). We found the changes to be significant for HbO and HbR within 0-0.7s of stimulus onset (arrow). We failed to find significant changes for HbT for the same period (**C**, green trace). These findings demonstrate that during conditions of low spiking, the initial-dip consists of increases in HbR and decreases in HbO, and the HbT dip is absent. This suggets that the HbT dip is only induced during conditions of strong bursts in spiking activity.

Supplementary table 1. Hemodynamic initial dips during spontaneous and stimulus-induced activity.

dataset	parameter	condition	mean	SEM	p-value*	Sample-size
Stimulus-induced activity	Peak spike-rate (spk/s)	all trials	705.85	14.7	$<10^{-10}$	260
		high-spiking	899.96	12.89	$<10^{-10}$	122
		Low-spiking	497.28	8.35	$<10^{-10}$	125
	HbO dip ($\mu mol \cdot L^{-1}$)	All trials	-0.52	0.12	$<10^{-7}$	260
		high-spiking	-0.87	0.146	$<10^{-11}$	122
		Low-spiking	-0.22	0.188	0.21	125
	HbR dip ($\mu mol \cdot L^{-1}$)	All trials	-0.04	0.078	0.89	260
		high-spiking	-0.2	0.089	0.0076	122
		Low-spiking	0.09	0.12	0.18	125
	HbT dip ($\mu mol \cdot L^{-1}$)	All trials	-0.56	0.11	$<10^{-10}$	260
		High-spiking	-1.08	0.112	$<10^{-14}$	122
		Low-spiking	-0.13	0.179	0.287	125
	HbR buildup ($\mu mol \cdot L^{-1}$)	All trials	-0.041	0.805	0.634	260
		High-spiking	0.236	0.093	$<10^{-3}$	122
		Low-spiking	-0.365	0.133	0.007	125
	HbR- modulation (epoch II – epoch I)	All trials	0.029	0.095	0.135	260
		High-spiking	0.534	0.077	$<10^{-10}$	122
		Low-spiking	-0.481	0.165	$<10^{-3}$	125
	HbO/HbT dip (%)	High-spiking	50.36	17	-	122
Spontaneous activity	Total spike count	All runs	$1.56x10^5$	$1.03x10^4$	$<10^{-3}$	16
		High-spiking	$1.86x10^5$	$5.81x10^3$	0.0078	8
		Low-spiking	$1.27x10^4$	$1.36x10^4$	0.0078	8
	HbO dip (a.u.)	All runs	-0.034	0.005	$<10^{-6}$	48
		High-spiking	-0.051	0.012	$<10^{-3}$	80
		Low-spiking	-0.036	0.015	0.06	80
	HbR dip (a.u.)	All runs	-0.009	0.005	0.1	48
		High-spiking	-0.032	0.014	0.0041	80
		Low-spiking	-0.001	0.016	0.9	80
	HbT dip (a.u.)	All runs	-0.043	0.007	$<10^{-6}$	48
		High-spiking	-0.07	0.016	$<10^{-5}$	80
		Low-spiking	-0.037	0.018	0.122	80
	HbR buildup (a.u.)	High-spiking	0.04	0.0136	0.011	80
		Low-spiking	0.039	0.012	0.049	80
	HbR- modulation	High-spiking	0.072	0.024	0.0017†	80
		Low-spiking	0.041	0.031	0.16†	80
	HbO/HbT dip (%)	High-spiking	58.9	32	-	48

* Wilcoxon's two-tailed sign-rank test

† Wilcoxon's one-tailed sign-rank test

Appendix 4: Real-Time Subject-Independent Pattern Classification of Overt and Covert Movements from fNIRS Signals.

PLOS | ONE

RESEARCH ARTICLE

Real-Time Subject-Independent Pattern Classification of Overt and Covert Movements from fNIRS Signals

Neethu Robinson[1☯¤a], Ali Danish Zaidi[2,3☯*], Mohit Rana[3¤b], Vinod A. Prasad[1], Cuntai Guan[1,4], Niels Birbaumer[3,5], Ranganatha Sitaram[1,2,3,6*]

1 School of Computer Science and Engineering, Nanyang Technological University, Singapore, Singapore, **2** Max Planck Institute for Biological Cybernetics, Tuebingen, Germany, **3** Institute of Medical Psychology and Behavioral Neurobiology, University of Tuebingen, Germany, **4** Department of Neural and Biomedical Technology, Institute for Infocomm Research, A*STAR, Singapore, Singapore, **5** Wyss Center for Bio and Neuroengineering, Geneva, Switzerland, **6** Department of Psychiatry and Division of Neuroscience, Schools of Engineering, Biology & Medicine, Pontificia Universidad Católica de Chile, Santiago, Chile

☯ These authors contributed equally to this work.
¤a Current address: Birla Institute of Technology and Science–Pilani, Goa, India
¤b Current address: Department of Psychiatry and Division of Neuroscience, Schools of Engineering, Biology & Medicine, Pontificia Universidad Católica de Chile, Santiago, Chile
* rasitaram@uc.cl (RS); azaidi@tue.mpg.de (ADZ)

OPEN ACCESS

Citation: Robinson N, Zaidi AD, Rana M, Prasad VA, Guan C, Birbaumer N, et al. (2016) Real-Time Subject-Independent Pattern Classification of Overt and Covert Movements from fNIRS Signals. PLoS ONE 11(7): e0159959. doi:10.1371/journal.pone.0159959

Editor: Eleni Vasilaki, University of Sheffield, UNITED KINGDOM

Received: April 17, 2016

Accepted: July 11, 2016

Published: July 28, 2016

Data Availability Statement: All relevant data are within the paper. The raw matlab data and figure files relevant to the manuscript have also been uploaded to Figshare (https://figshare.com/s/56ee9be75c3a891fd1d2).

Funding: Funded by Deutsche Forschungsgemeinschaft (DFG BI 195/59-1, DFG BI 195/56-1 and DFG 195/65-1); the Badenwürttemberg-Singapore Life Sciences Grant; the INDIGO research grant from the European Union and India; FP7-ICT-2009-258749 - CEEDs: The Collective Experience of Empathic Data Systems;

Abstract

Recently, studies have reported the use of Near Infrared Spectroscopy (NIRS) for developing Brain–Computer Interface (BCI) by applying online pattern classification of brain states from subject-specific fNIRS signals. The purpose of the present study was to develop and test a real-time method for subject-specific and subject-independent classification of multichannel fNIRS signals using support-vector machines (SVM), so as to determine its feasibility as an online neurofeedback system. Towards this goal, we used left versus right hand movement execution and movement imagery as study paradigms in a series of experiments. In the first two experiments, activations in the motor cortex during movement execution and movement imagery were used to develop subject-dependent models that obtained high classification accuracies thereby indicating the robustness of our classification method. In the third experiment, a generalized classifier-model was developed from the first two experimental data, which was then applied for subject-independent neurofeedback training. Application of this method in new participants showed mean classification accuracy of 63% for movement imagery tasks and 80% for movement execution tasks. These results, and their corresponding offline analysis reported in this study demonstrate that SVM based real-time subject-independent classification of fNIRS signals is feasible. This method has important applications in the field of hemodynamic BCIs, and neuro-rehabilitation where patients can be trained to learn spatio-temporal patterns of healthy brain activity.

FP7-ICT-2009-247935 – BETTER: BNCI-driven Robotic Physical Therapies in Stroke Rehabilitation of Gait Disorders; and the Centre for Integrative Neuroscience (CIN) (PP 2012-16).

Competing Interests: The authors have declared that no competing interests exist.

Introduction

In contrast to the classical method of presenting stimuli and studying evoked brain responses, BCI and neurofeedback work by altering the neural activity first, and then observing the effect of this altered activity on the subjects' behavior [1,2]. This allows the dissection of the functional anatomy of the brain. Furthermore, the ability to learn to volitionally regulate activity from a circumscribed brain area has potential for applications towards rehabilitation. Since most of the evoked responses in the brain are in the form of spatio-temporal patterns of activity (electrical or hemodynamic), a system capable of successfully classifying these patterns is an indispensable tool for rehabilitation [2]. Such a system has been successfully developed for fMRI based BCI using real-time Support Vector Machine (SVM) based classification algorithms [3], and an earlier study has also demonstrated the feasibility of implementing machine learning algorithms in classifying single trial activations using multi-channel fNIRS [4]. Furthermore, feasibility and potential effectiveness of an fNIRS based real-time neurofeedback system on performance of kinesthetic motor imagery has also been reported recently [5]. In this study participants performed motor imagery of finger movements with feedback from relevant cortical signals and irrelevant sham signals. The study showed that true neurofeedback induced significantly greater activation of the contra lateral pre-motor cortex and greater self-assessment scores for kinesthetic motor imagery compared with sham feedback. These results illustrate the efficacy of using both fNIRS signals for neurofeedback and machine-learning algorithms for implementing single-trial classifications from such signals. In the present study, we aimed at combining these two approaches so as to develop a real-time SVM based neurofeedback system based on multi-channel fNIRS signals.

Our first objective was the development of a real-time SVM based pattern classification and neurofeedback system. For our study, we used fNIRS signals from the motor cortex while subjects were performing overt and covert hand movements (movement execution (ME) and movement imagery (MI), respectively). We trained the classifier on patterns evoked during ME and tested them on those evoked during MI, and vice versa, establishing the robustness of the classifier on both modalities. Finally, we determined if a pattern-classifier modeled on a group of subjects could be used to classify activation patterns in a new subject. We trained the generalized, subject-independent classifier on movement execution data of four participants and tested it on both movement imagery and execution in new, untrained participants. The main purpose was to establish that the activation patterns from different subjects can be successfully utilized to generate a group classifier that can then identify similar patterns in new subjects. The most significant application of this technique is toward neurofeedback based neuro-rehabilitation, where such a 'generalized' classifier can be trained on spatio-temporal activation patterns of healthy subjects, and then used to help train patients to 'modulate' their activity to represent healthy activation patterns.

Methods

Experiment Protocol

To analyze brain activations during bilateral hand movement execution (ME) and imagery (MI), the experimental protocol was designed to consist of five conditions, namely movement execution of left and right hand, motor imagery of left and right hand, and rest condition. The participants were asked to perform repetitive hand movements similar to clenching and unclenching an imaginary ball at a frequency of ~1 Hz during motor execution. During movement imagery, participants were asked to imagine similar movements, without actually moving their hands. No physical movement was observed in any subject during the imagery tasks.

Participants were asked to participate in five runs of one experiment, each of which consisted of six task blocks separated by seven rest blocks (Fig 1A). Some participants, however, did not complete all five runs. One participant, S11 performed both Experiments 1 and 2. A break of about 5–10 minutes was given between runs. In Fig 1A, Left and Right refers to left and right hand's movement for both execution and imagery tasks. Each participant was seated in front of the screen that displayed the visual cues. As per the protocol, the cues for each block were as follows: a blue screen with a black dot for "Rest", a red screen with a Right arrow, for "Task-Right" and green screen with Left arrow, for "Task-Left". An activation-level meter (hereafter called thermometer as it is depicted graphically as a thermometer) with baseline level indicated at its middle, appeared on center of the screen during the training runs. For test runs, neurofeedback was given as the thermometer grades. The dynamic range of the thermometer was 20 units or levels.

Our study comprises three different experiment paradigms as shown in Table 1 and the details are given in this section. In all the experiments, the initial one or two runs were used for training the system. No feedback was provided during training runs, and the thermometer grade remained at the baseline. Following this, the subjects were instructed to perform the test runs with neurofeedback. Feedback was provided as increase or decrease in thermometer grade during correct and incorrect classification respectively.

Experiment 1. The main objective of this study was to implement real-time subject-dependent classification of bilateral hand movement using a movement execution trained BCI. The system was validated on bilateral motor execution and imagination data, to provide real-time classification results and spatial activation patterns for further analysis. In the experiment, the classifiers were adapted as per Eq (9) for the following test runs. Run 3 tested the classifier on ME for each subject. Runs 4 and 5 were used to test classification of MI based on ME models, and the subjects were asked to imagine the movements. In all the test runs, the subjects were provided a visual feedback based on the classification output.

Experiment 2. The objective of this study was to perform a corollary to Experiment 1, i.e., to implement real-time subject-dependent classification and feedback of left versus right hand motor imagery, based on a classifier built using covert hand movement data. In the MI runs, 1 to 4, the subjects (S21, S22, S23, S11) were instructed to imagine the movement they had practiced. The first run was used for training the classifier. For Runs 2 to 4, the classifier was updated after each Run, as per Eq (9). The performance of subjects performing MI was tested using the classifier and a neurofeedback was provided. Run 5 was used to test classification of ME based on MI models (with the classifier modeled based on the last two MI runs) and the subjects were asked to perform ME.

Experiment 3. The objective was to demonstrate the feasibility of a Subject-Independent Classifier (SIC) built from the ensemble data of all participants from Experiment 1, performing hand movement execution. At the beginning of this experiment, a practice session was provided where the subjects (S31, S32, S33, S34) were asked to perform hand clenching actions. During the experiment, in test runs 2, 3 and 4, the subjects were asked to perform MI of the practiced movements without moving their hands. In the ME run 5, the subjects were asked to execute the movement. Real-time classifications of overt and covert movements from new subjects were performed using the SIC and neurofeedback was provided in all the runs.

Feature Extraction and Selection

The study aims to use multi-channel temporal information of changes in concentration levels of blood oxy hemoglobin (HbO) to classify volitional overt and covert hand movements. The smaller levels of concentration changes and lesser discrimination between movement classes

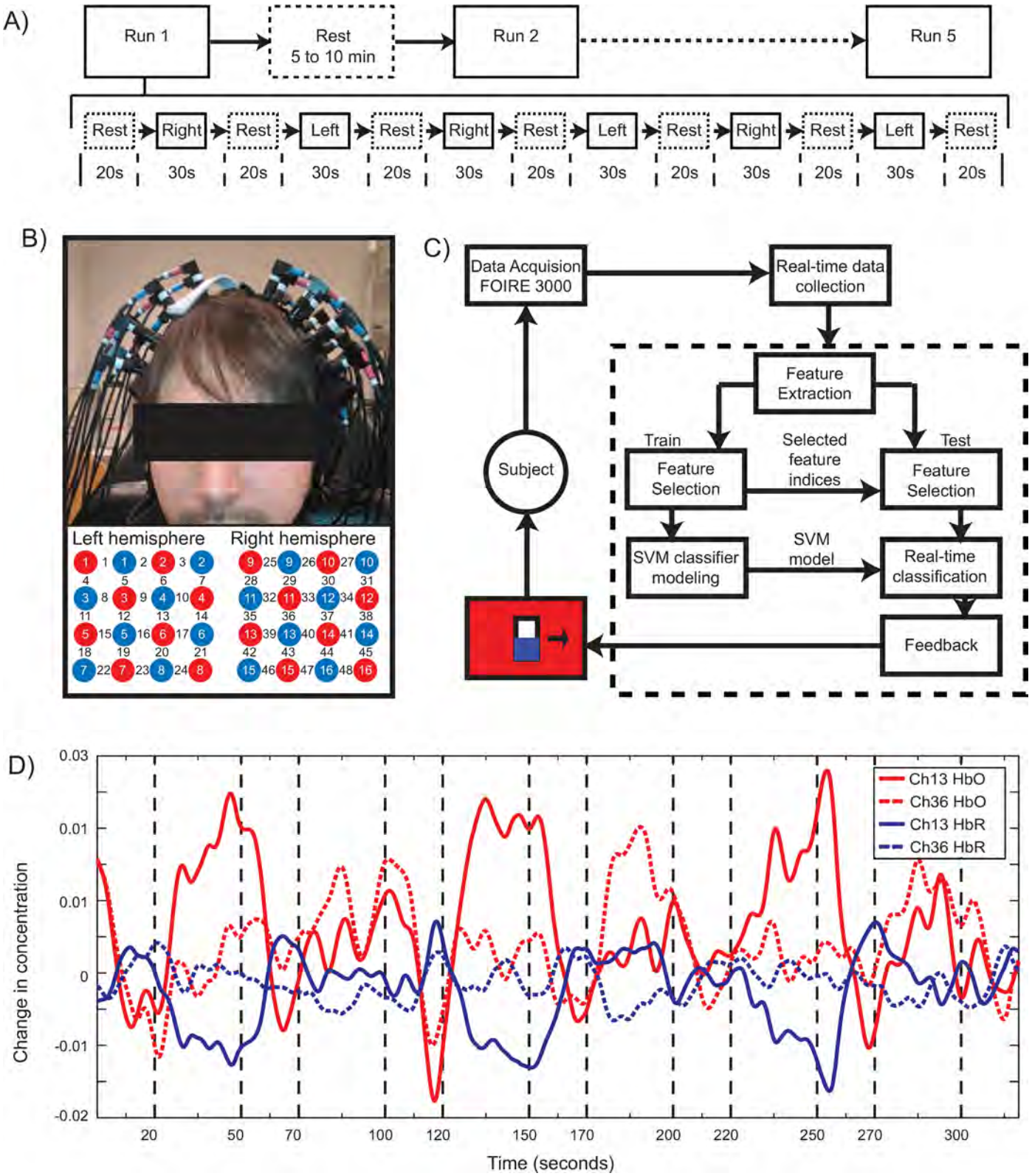

Fig 1. Overview of the real-time neuro-feedback binary classification system. A) Experiment protocol and timeline for the experiment: Runs 1–5 are separated by 5–10 minutes rest periods. The sequence of blocks with their durations for each Run is shown under Run 1. B) Arrangement of optodes and the headmount. The optodes are placed over the motor area and arranged in 4x4 checkerboard topography. The red and blue circles

indicate emitters and detectors respectively. The numbers 1–48 indicate the recorded channels. C) The architecture of the designed system indicating its various functional units. The feedback generated by BCI is displayed to the subject as indicated. For details refer to text. D) Sample time course of activations during motor execution. The pre-processed data from Experiment 1, Subject S11, Run 3 is shown. Channel 13 and 36 are from PMC in left and right hemispheres. The contralateral activations of HbO and dip in HbR can be clearly identified from the plots.

doi:10.1371/journal.pone.0159959.g001

offered by HbR, limits its use for further processing. The discriminative features from fNIRS recordings are extracted from the time averages of changes in HbO concentration from the various channels located over the motor cortex. The real-time classification of signal features and estimation of neurofeedback are performed at every unit time (1 second). Hence, for an N_t -channel arrangement, the features extracted at k^{th} second of a trial from nth channel is given by,

$$f^n(k) = \sum_{i \in 1 \text{ to } f_s} \Delta HbO_i^n\ (k) \tag{1}$$

where f_s is the sampling frequency and $n = 1$ *to* N_t. The feature set at k^{th} instant is given by,

$$F(k) = \{f^1(k), f^2(k), f^3(k), \ldots\ldots, f^{N_t}(k)\} \tag{2}$$

A feature selection technique based on mutual information [6,7] selects $N < N_t$ features from Eq (2). This technique effectively chooses the channels that provide optimal discriminating information for the task performed by the participant. For an N_t—dimensional feature set F, the mutual information based technique selects, $S \subset F$, an N-dimensional subset that maximizes the mutual information, $I(F;\omega)$, where ω represents each class $i \in \{1,2\}$. Mutual information is given by,

$$I(F;\omega) = H(\omega) - H(\omega|F), \quad \omega \in \{\omega_1, \omega_2\} \tag{3}$$

$$H(\omega|F) = -\sum_{i=\{1,\ 2\}} p(\omega_i|F) \log_2 p(\omega_i|F) \tag{4}$$

where, $H(\omega)$ denotes the class entropy and $H(\omega|F)$ gives the conditional entropy. The conditional probability $p(\omega|F)$ is estimated using Parzen window method. The mutual information for all the N_t features are calculated and the best N features are selected to obtain,

$$S(k) = \{f^n(k)\},\ n \in \textit{selected N features} \tag{5}$$

The value of N is set to 12 in this work, and it is ensured that equal number of features are selected from both left and right hemispheres. The performance of the system may vary depending on N, however, characterization of the effect of number of features on classification accuracy is beyond the scope of this work and hence would not be considered in this

Table 1. Overview of experimental design for various experiments.

	Run 1	Run 2	Run 3	Run 4	Run 5
Experiment 1	*ME*[a]	*ME*	ME	MI[b]	MI
Experiment 2	*MI*	MI	MI	MI	ME
Experiment 3	*ME*	MI	MI	MI	ME

[a]ME stands for Motor execution

[b]MI stands for Motor Imagery. Italicized runs represent the ones used to train the classifier.

doi:10.1371/journal.pone.0159959.t001

manuscript. The feature set *S(k)* for every k^{th} instant is fed as input to the classifier for real-time classification and to calculate neurofeedback.

Support Vector Machines (SVM)

SVM is a supervised learning technique that creates a boundary between two classes of data based on a set of available training samples [8]. It designs a decision function that optimally separates the two classes in the training data. In this study we use a linear-SVM to separate left versus right hand movements. For real time classification, we consider the features obtained at each instant *k* as a separate training data sample. The data sample at k^{th} instant is the feature vector denoted by *S(k)* or S^k. The SVM-classifier determines a weight vector *W*, that discriminates a class against the other by the projection *W'S* and linear discriminant rule,

$$\omega \begin{cases} \in \omega_i & W'S^k \geq b \\ \in \omega_i & W'S^k < b \end{cases} \tag{6}$$

where *b* is a bias. This vector is determined by minimizing the cost function,

$$J(W) = \frac{1}{2}\|W\|^2 \tag{7}$$

subject to the constraint,

$$Y^k\ (W'.S^k - b) \geq b,\ \ k = 1\ to\ K \tag{8}$$

where Y^k is the class label corresponding to S^k, that is a sample from the training data set {S^1, S^2,. . ...,S^K} and *K* is the number of training data samples. The SVM classifier thus modeled is used to classify or to determine the label of incoming data samples.

1.3 Adapting Classifier and Feature selector

For neurofeedback training applications, the BCI is designed to provide feedback information regarding the quality of the performed task to the user in real time. Considering the non-stationarity of the neural signals there is a need to adaptively update the classifier and feature selector in the system [4,9].

In the subject-dependent classifier experiments, the initial run is used to select the most informative features and model the SVM classifier that optimally discriminates the binary class data. This is used to classify the data samples of Run 2 in real time. As given in (9), from the 3rd Run onwards, the classifier is re-modeled using the data from two previous runs.

$$\{N; W\}^{(r)} = \left\{ \begin{array}{cc} C(S^{(r-1)}), & r = 2 \\ C([S^{(r-1)}; S^{(r-2)}]), & r > 2 \end{array} \right\} \tag{9}$$

where, *r* is the run number, $S^{(r)}$ is the data set collected during Run *r* and *C* denotes the feature selection and classifier modeling functions. Moreover, a bias cancellation is performed from Run 2 onwards that subtracts the average of SVM output during the Rest block from the following Task block. The real-time system thus adopts a between-runs adaptive strategy of re-training classifiers after each run and within-run adaptive bias correction of SVM outputs.

Participants

The data were recorded from 11 healthy participants (both male and female, aged 21–35). All participants signed a written informed consent. The study was approved by the Institutional

Review Board, Faculty of Medicine of the University of Tuebingen, Germany. Each participant was compensated monetarily for participation in the experiment.

Data Acquisition

FNIRS signals were acquired using a Shimadzu FOIRE-3000 imaging system operating at a sampling rate of 7.69Hz, using wavelengths of 780nm and 830nm from laser sources. Emitters and detectors were separated by 25mm, and were placed on top of the participant's head using a semi-flexible head mount. Sixteen sources and detectors were arranged in two 4-by-4 checkerboard topographies, as shown in Fig 1B centered on C3 and C4 of the International 10–20 System. This arrangement covered most of the primary motor, pre-motor and somatosensory cortices.

Real-Time fNIRS-BCI System Schematic

The architecture of the real-time system designed is shown in Fig 1C. FNIRS signals are received online in the BCI-processing computer from the FOIRE-3000 equipment. The BCI-processing system consists of a feature extractor, a feature selector and a classifier. The data are fed into the processing system in real-time. As indicated in Section 1.1, we extract the relevant features from the recorded fNIRS data. The data from training runs are used to select the informative features and to model the classifier as explained in Section 1.3. For the test runs, after the movement task stimulus onset, a bias correction is performed and the extracted features are classified in real-time using the SVM model created. The classified output is generated at every second so as to provide feedback in real time. This output is presented to the participant in the form of a graphical thermometer in which a correct classification would lead to a unit rise in the thermometer, and incorrect classifications would lead to a unit fall in the thermometer reading. The thermometer reading remains at 0 (middle) during "Rest" period and returns to this position at the end of every movement task.

Offline Data Analysis

The preprocessing steps used to improve the Signal-to-Noise ratio and derive optimal information from recorded fNIRS data were as follows: the data was baseline corrected followed by pre-coloring using a hemodynamic response function-low pass filter; the global trends were removed using Wavelet-Minimum Description Length technique. A sample time course of activation of pre-processed fNIRS recording is shown in Fig 1D, which plots the HbO and HbR signals from channels 13 and 36 (corresponding to primary motor cortex (BA4) in left and right hemispheres respectively) from Subject S11, Experiment 1, Run 2 From the figure, distinct changes can be seen in the contralateral activity of oxy- and deoxy-hemoglobin concentrations. These changes were utilized for feature extraction and modeling of the SVM-based classifier.

To ensure stationarity of the training data used to create classifiers, 5- fold cross-validation analysis was performed. The training data was randomly split into five subsets. In each cross-validation fold, data from four subsets were used to select features and model classifier that was used to classify the remaining test subset. The process was repeated to test all the subsets and an average performance over all the folds was calculated. The low values of training classification accuracy's standard deviations indicated the low variance of the training dataset used (not shown).

fNIRS signals were also analyzed to determine statistically significant spatial activations by a univariate approach using SPM 5 fNIRS toolbox [10]. The spatial plots of mutual information

obtained from Eq (4) and the SVM outputs obtained from Eq (8) are also reported among the various results.

Results

The evaluation results of the real time fNIRS based neurofeedback system for classifying left versus right hand overt and covert movements are presented in this section. Subsection 3.1 indicates the real time classification performance of the system and the system parameters identified by offline analyses on the data, followed by 3.2 explaining the subject independent classifier, its parameters and the results obtained. Subsection 3.3 reports the results indicating homologous activations during overt and covert movements using spatial activation maps. The practical significance of each of the results is also discussed.

Real-Time Classification

The motor performance of subjects is evaluated in real-time by online feature extraction and SVM classification of bilateral motor tasks and the percentage classification accuracies are reported. Fig 2 summarizes the performance of the proposed real-time classification system for overt movement execution and imagery with neurofeedback. The results indicated are percentage classification accuracies attained by subjects in each of the runs for various tasks indicated using MI (motor imagery) and ME (motor execution) labels. To comply with experimental guidelines, subjects were allowed to discontinue the experiment if they experienced fatigue.

The *Experiments 1* and *2* used subject-dependent classifier models for bilateral MI and ME classification. In *Experiment 1*, the average classification accuracy over four subjects obtained for runs 3 and 4 are 80% (ME) and 72% (MI) respectively, where the task performed is indicated within brackets. Not all subjects were able to complete the five runs due to fatigue. In *Experiment 2*, for all subjects the accuracy falls after the first run and improves afterwards. On an average, the classification accuracies are reported as 69% (MI), 41% (MI), 51% (MI) and 73% (ME) for runs 2, 3, 4 and 5 respectively. The last run (run 5) used the classifier trained on MI for online classification of bilateral ME. A general trend seen in the results is a dip in performance after the first run, followed by gradual rise. Although the paradigm we use is insufficient to prove the effect of neurofeedback training and its learning effect in subjects, the performance trend obtained indicates subject's capability to identify and enhance motor control strategy after each run. Longer experiment sessions might reveal more information on such a learning curve. The simple adaptive strategies of re-training classifier and bias correction seem to work efficiently in this real-time system.

Classification parameters. The intermediate results in the online system, namely, the data used for modeling the classifiers, the classifier models created, and the feature selection proceedings were evaluated. The results are shown in Figs 3 and 4. The objectives were: (1) to demonstrate offline classification accuracies, (2) to obtain various parameters of the SVM classifier used and identify how they contribute to the classification performance, (3) to illustrate how mutual information based feature selection helps extract the optimal information and (4) to show the temporal averages over runs demonstrating class-dependent hemodynamic activity.

The results for analyses (1)-(4) in experiments 1 and 2 are illustrated in the following subsections. Fig 3 and Fig 5 represent Experiment 1, and Fig 4 and Fig 6 indicate results of Experiment 2 respectively.

Fig 3A indicates the cross-validation accuracies for offline classification of ME data in *Experiment 1* used to create SVM models. The average accuracies are 82.06±1.31% and 85.70 ±1.59% respectively (classifier modeling using Run 1 was not performed for all the subjects). As seen, the standard deviation for each subject indicated in the curves is less than 2%. This

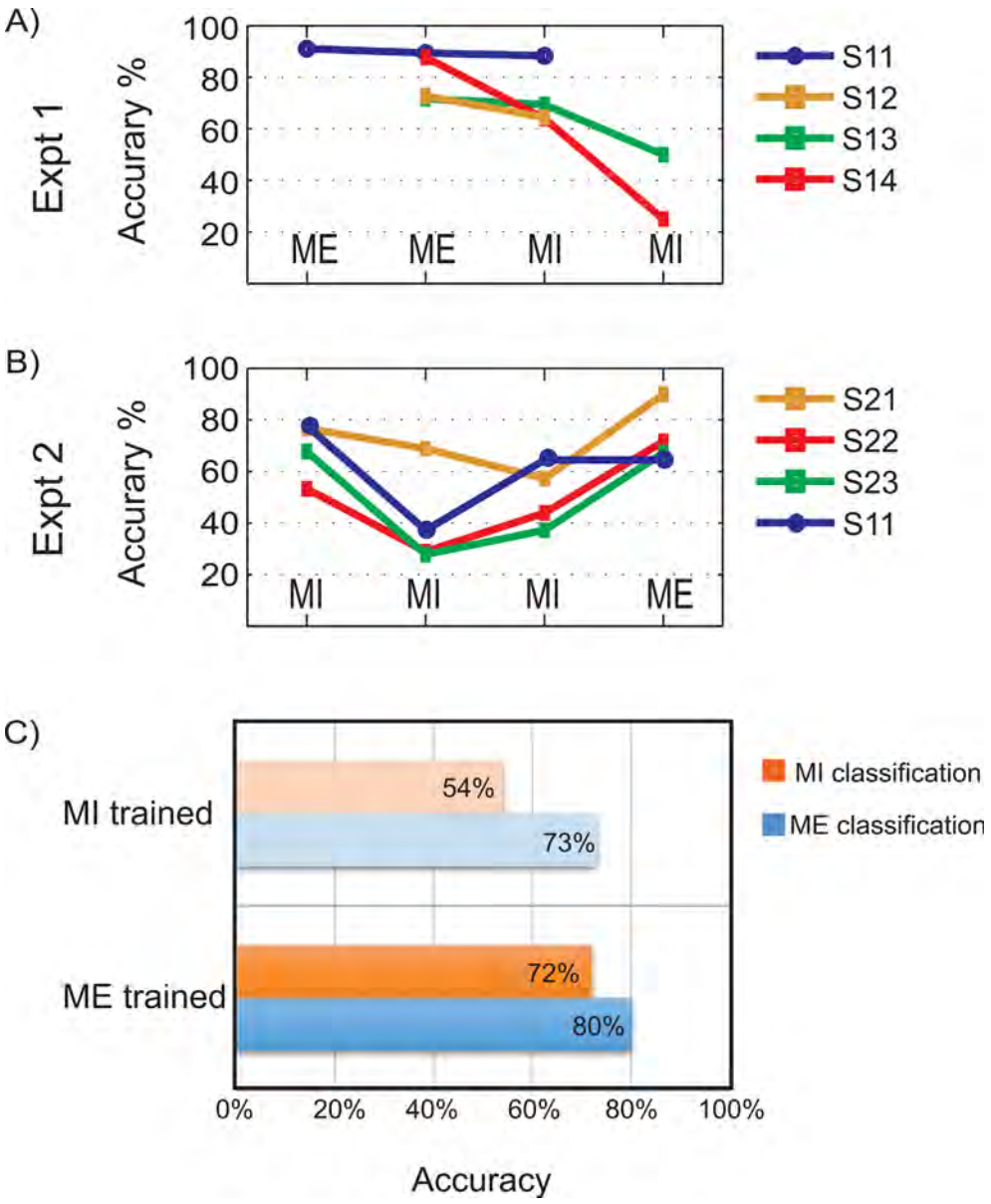

Fig 2. Real-time classification performance for experiments 1 and 2. A and B) The percentage classification accuracies for online binary (right v/s left motor tasks) classification for 7 subjects for the Experiment 1 (A) and Experiment 2(B) are shown. The motor tasks involved are right and left Motor Execution (ME) and Motor Imagery (MI). Note: Subject S11 was common between both experiments 1 and 2. C) Comparison of mean classification accuracies of motor imagery and execution when classifier was trained on either motor imagery or motor execution.

doi:10.1371/journal.pone.0159959.g002

indicates a uniform performance in all folds of cross validation and so, the entire data are used to create classifiers. To demonstrate the various characteristics of the system, data from Subject S11 is used as an example. Fig 3C indicates the SVM output obtained in the real-time classification of data for all the runs. The curves clearly indicate the advantage of using bias correction for real-time classification. In all the runs, the SVM output gradually increases and reaches its peak value after 3 to 5 seconds from the onset of the movement cue. This can be identified as an effect of hemodynamic delay. However, in this experiment this delay is not taken into

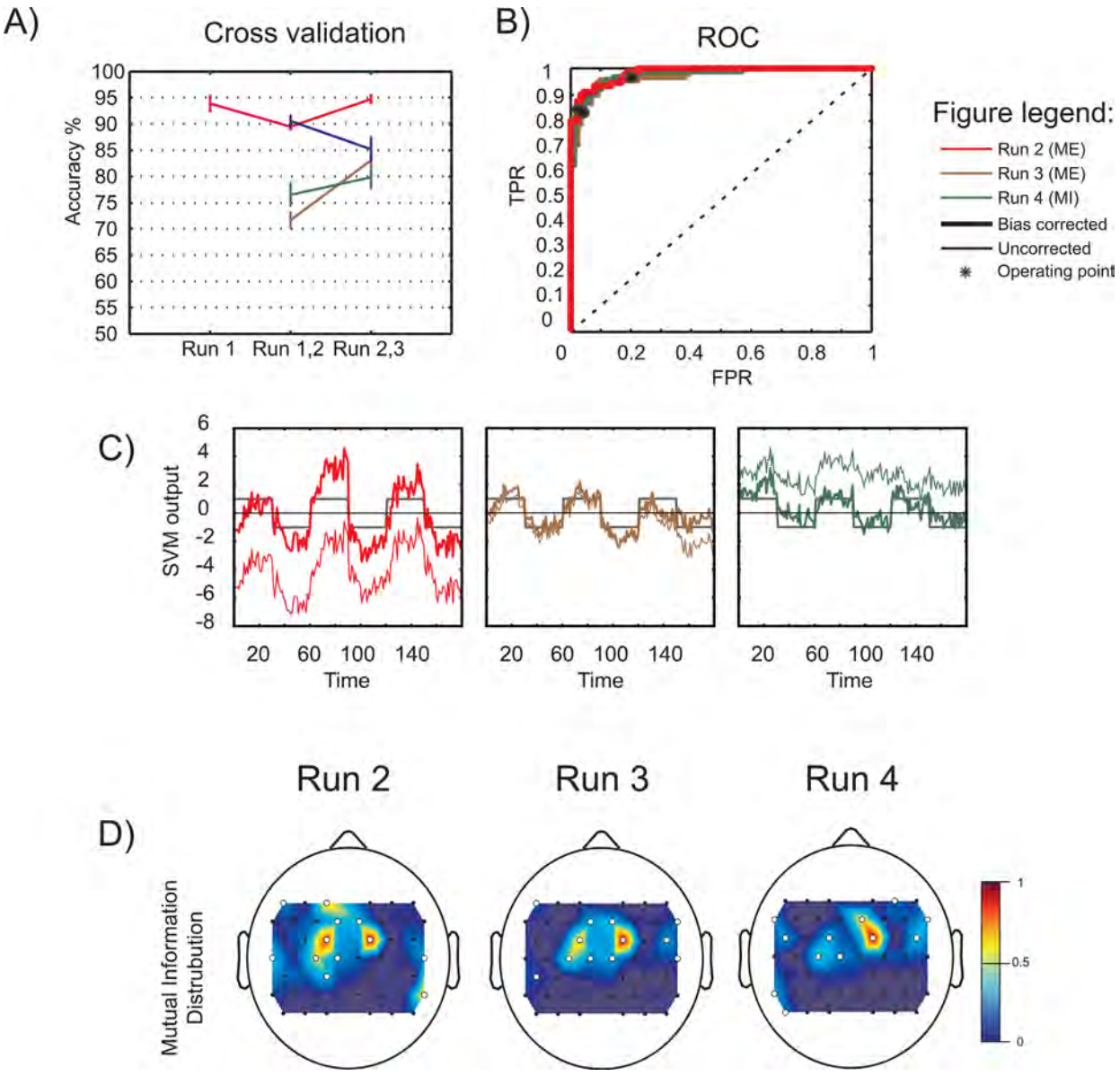

Fig 3. Classifier parameters for Experiment 1. A) The offline 5-by-5 cross-validation classification accuracies in percentage. The x-axis indicates the runs that contribute to the dataset, which is later used to generate the online classifier model. The error bars represent standard deviations. B) ROC curves of the classifiers used in the different runs during online classification. The operating point is indicated by an asterisk (*). C) The SVM outputs obtained from the online classification. The uncorrected and bias-corrected values are represented using thin and thick lines respectively. The class of data is indicated as +1 for right hand and -1 for left hand blocks. D) The spatial distribution of mutual information for each of the training dataset. The white dots represent selected channels based on high mutual information.

doi:10.1371/journal.pone.0159959.g003

account by the classifier as it provides real-time output right from the start of movement onset. Fig 3D displays the spatial distribution of mutual information obtained based on oxy-hemoglobin data. The channels with higher mutual information are indicated by white dots and the features from these channels are selected for further classification. The channels providing highest mutual information of bilateral movement are obtained from the primary motor cortex of the brain. Fig 3B illustrates the receiver operating characteristics (ROC) curves of the various classifiers used. The classifier operation points (indicated by the black asterisk) are at high True

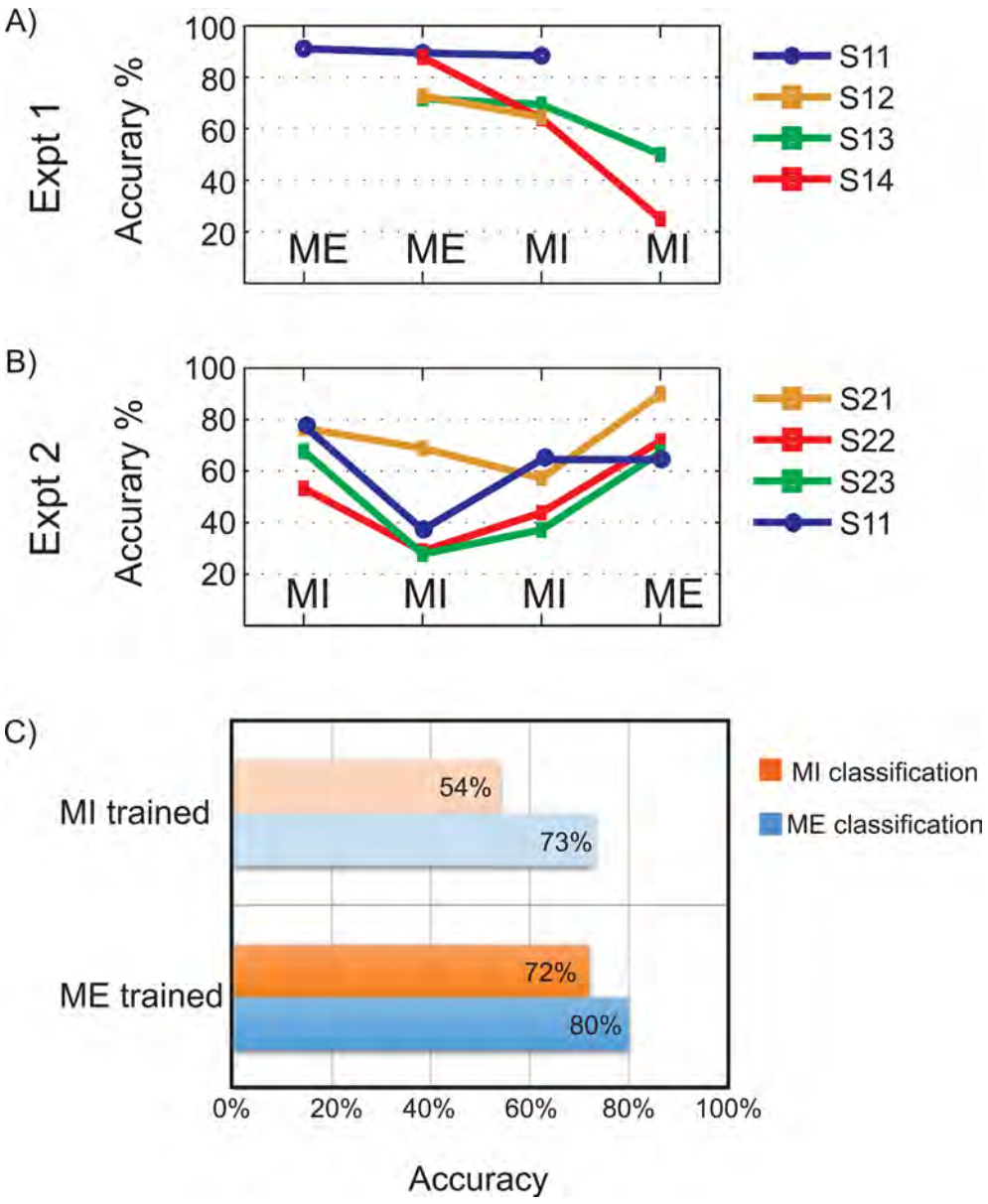

Fig 4. Classifier parameters for Experiment 2. A) The offline 5-by-5 cross-validation classification accuracies in percentage. The x-axis indicates the runs that contribute to the dataset, which is later used to generate the online classifier model. The error bars represent standard deviations. B) ROC curves of the classifiers used in the different runs during online classification. The operating point is indicated by an asterisk (*). C) The SVM outputs obtained from the online classification. The uncorrected and bias-corrected values are represented using thin and thick lines respectively. The class of data is indicated as +1 for right hand and -1 for left hand blocks. D) The spatial distribution of mutual information for each of the training dataset. The white dots represent selected channels based on high mutual information.

doi:10.1371/journal.pone.0159959.g004

Positive Rate (TPR)—low False Positive Rate (FPR) regions, which indicate good classification performance.

The cross-validation accuracies obtained from classifier-training data for various runs of *Experiment 2* are shown in Fig 4A. The offline classification results reported are for MI classification. The mean over subjects for classifier models 1 to 4 are obtained as 84.11 ± 2.69%,

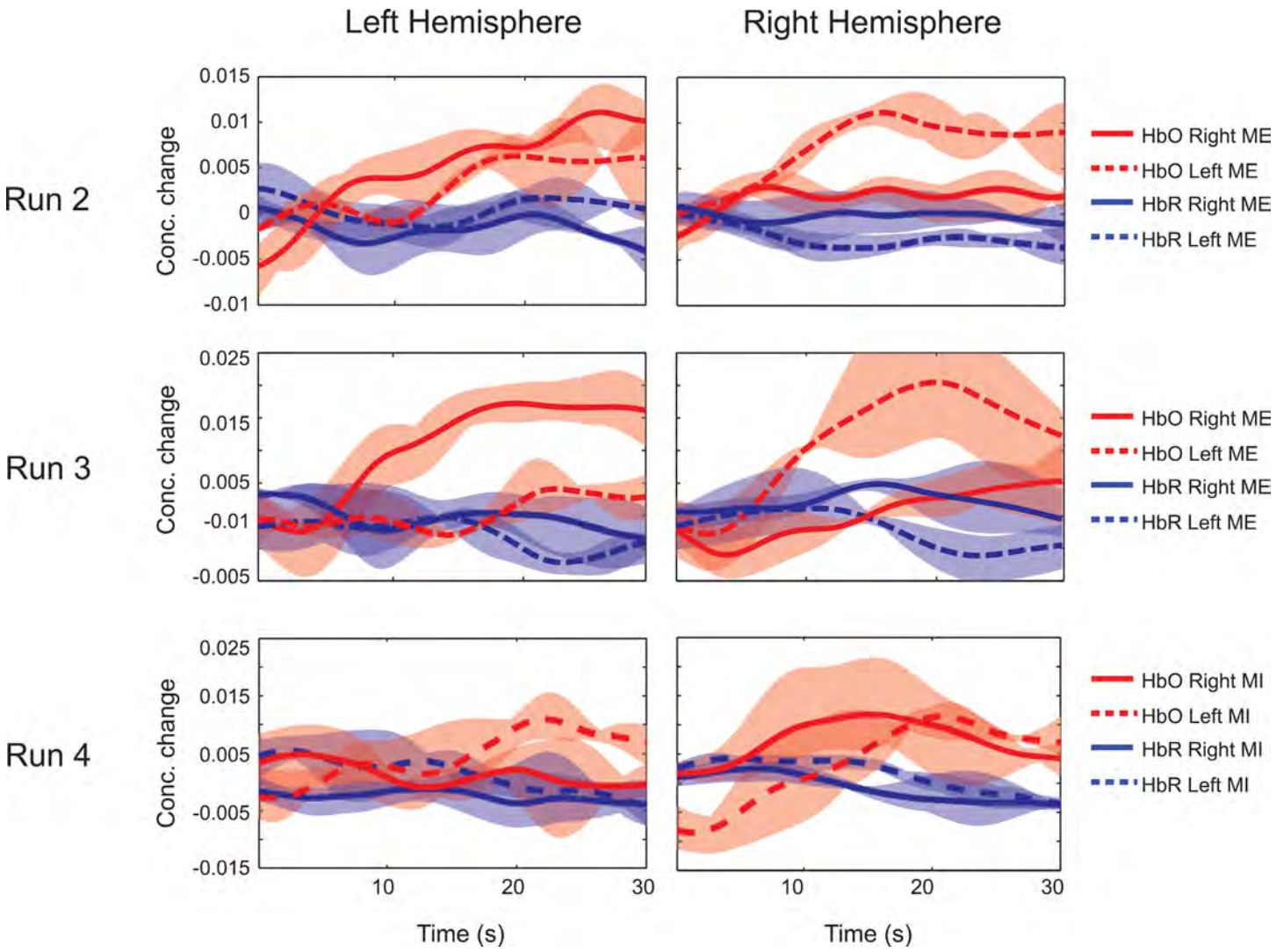

Fig 5. Average time series of activations in Subject S11 during Experiment 1. Runs 2, 3, 4 indicate activation levels given by concentration changes of HbO and HbR averaged over trials and selected channels. The channel selection is based on mutual information. The discriminative contralateral activations during both classes of movement can be noted.

doi:10.1371/journal.pone.0159959.g005

73.75 ± 2.47%, 74.17 ± 2.11% and 77.29 ± 2.21% respectively. The data recorded from subject S11 is used for further analyses and the results are reported. The SVM output obtained for every sample-classification in real-time for all the four runs are reported in Fig 4C. Fig 4D displays the mutual information distribution in the recorded channels. Comparing the activation maps, it can be noted that in all runs, except run 3, activations are observed over the pre-motor and motor areas. However, it can be noted that the patterns are as not localized as during ME. The ROC curves, obtained from each classifier, are shown in Fig 4B. The classifier used in run 2 generates a good ROC with operating point in high TPR–low FPR region providing an accuracy of 78% in real-time classification. But the ROC curve for Run 3 indicates a bad classifier design. This is reflected in the low classification accuracy (37%) obtained using this classifier (Fig 4B, brown curve). The classifier ROC improves later for runs 4 and 5 with better trend and operating points yielding better accuracy (64.44% in both runs).

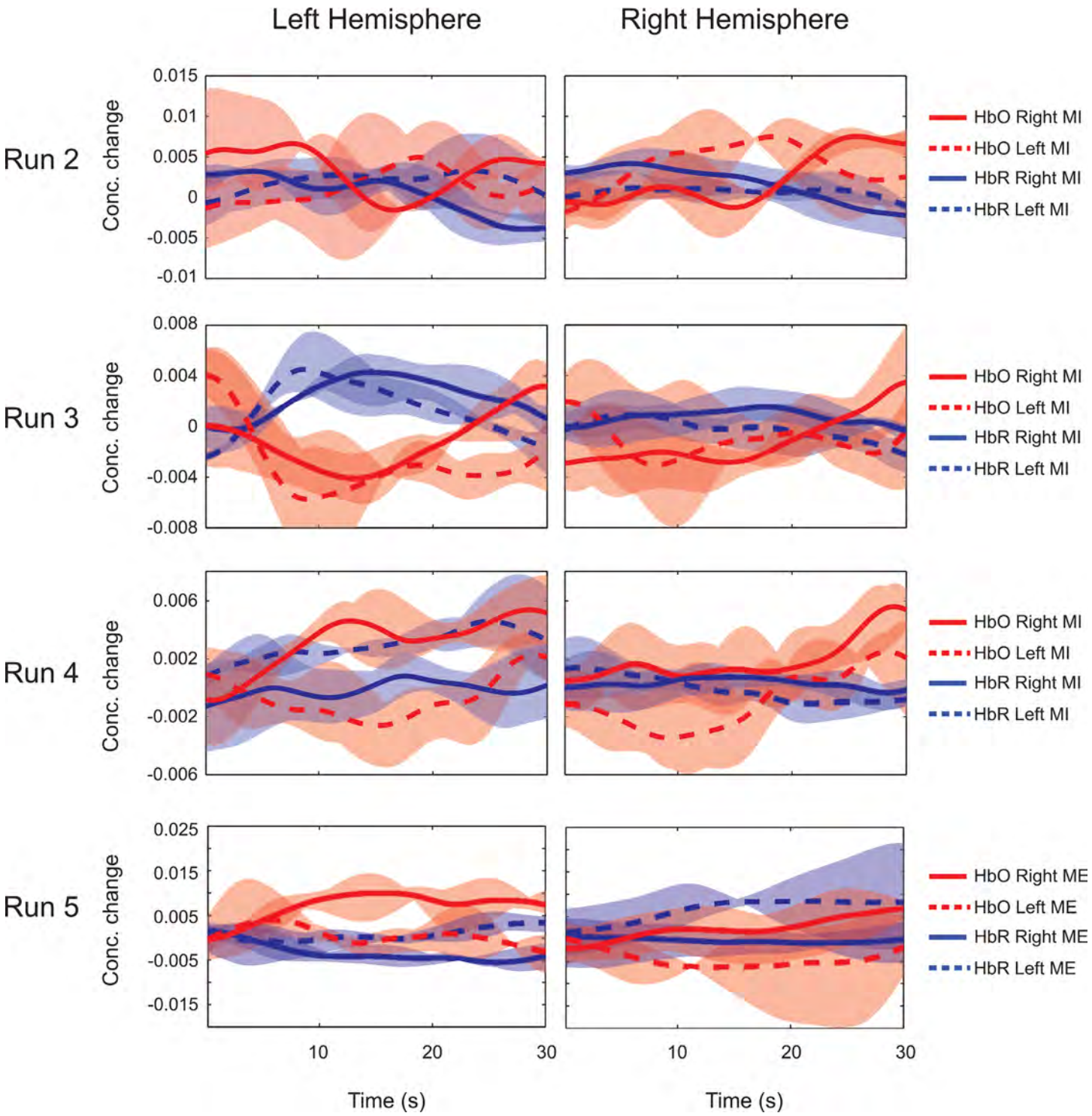

Fig 6. Average time series of activations in Subject S11 during Experiment 2. Runs 2–5 indicate activation levels given by concentration changes of HbO and HbR averaged over trials and selected channels. The channel selection is based on highest mutual information between left and right blocks. Note: Y-axis labels are different for different runs.

doi:10.1371/journal.pone.0159959.g006

Fig 5 (*Experiment 1*) and 6 (*Experiment 2*) explain the temporal changes in hemodynamic activity (HbO and HbR) averaged over selected channels in both hemispheres. The data are averaged over all the trials in each run and the upper and lower limits of the data are displayed along with their mean. The discriminating temporal activity in terms of contralateral activations can be seen in the curves. For example, in Fig 5, Run 3, for right hand ME, HbO levels show activations only in the left hemisphere. Similarly, in Run 3, HbO levels in right hemisphere rises as a result of activation during left hand movement. In Fig 6, the plots of Runs 2 to 4 and Run 5 correspond to MI and ME task respectively. It can be noted that, the levels of HbO concentration changes and the discrimination capabilities between MI classes are lesser when compared to ME data.

Subject-Independent Classification

The major focus of *Experiment 3* was to construct a subject-independent classifier (SIC) trained on multi-subject ME data, which could be used as a generalized classifier for MI and ME in real-time from new subjects. The ME data from Runs 1 to 3 of Experiment 1 was used to train an SVM subject-independent classifier. 5-fold cross-validation is performed to identify non-stationarity in data and a test accuracy of 68.22±3.25% was obtained. Due to the low variation in each of the cross-validation folds, the entire data were used to construct a subject-independent classifier model with a training accuracy of 68%. The features selected by the system are mentioned in *Section 3.2.3*. The real-time classification accuracy values obtained are displayed in Fig 7A. Out of four subjects, the performance of S34 was poor for MI classification which brought down the average accuracy. The subject reported difficulty imagining movements as they were tired and distracted. The mean classification accuracies for runs 2 to 5 were 64% (MI), 67% (MI), 57% (MI) and 80% (ME) respectively. The results prove the applicability of the proposed subject-independent pattern classifier for real-time neurofeedback movement classifications.

SIC System parameters. The detailed analysis of the subject-independent classifier generated in our study to classify MI and ME data is reported in this section and the data from Subject, S32 is used. Fig 7B shows the SVM outputs generated in four experimental runs. The advantage of using bias correction is evident from the plots. The spatial distribution of mutual information for the data used to train the classifier is shown in Fig 7C. Even though slightly shifted towards right hemisphere, the channels in the motor area are found to report high mutual information (indicated by white dots) and are hence selected for classification. The ROC curves for the classifiers used in all the four runs are given in Fig 7D. Runs 2, 3 and 5 indicate good ROC and selection of operating points, yielding real time classification accuracies of 72%, 72% and 88% respectively. Run 4 fails to perform well due to the bad ROC and hence could give only 58% classification accuracy. The temporal HbO activity during MI and ME for the data collected in *Experiment 3* are reported in Fig 8. The results are similar to previous experiments. The level of HbO concentration change is less for MI compared to ME, and the activation curves for both right hand and left hand MI overlap in most cases, providing minimum discrimination.

Discussion

The real-time neurofeedback system using our signal processing strategy offers the following advantages: (1) the system identifies the optimal discriminative features based on mutual information and applies these for classifier modeling, (2) the classifier adapts by itself after each run, making use of the data collected in the previous run, and (3) the bias correction within runs compensates for the dc shift in the feature space to provide better classification performance.

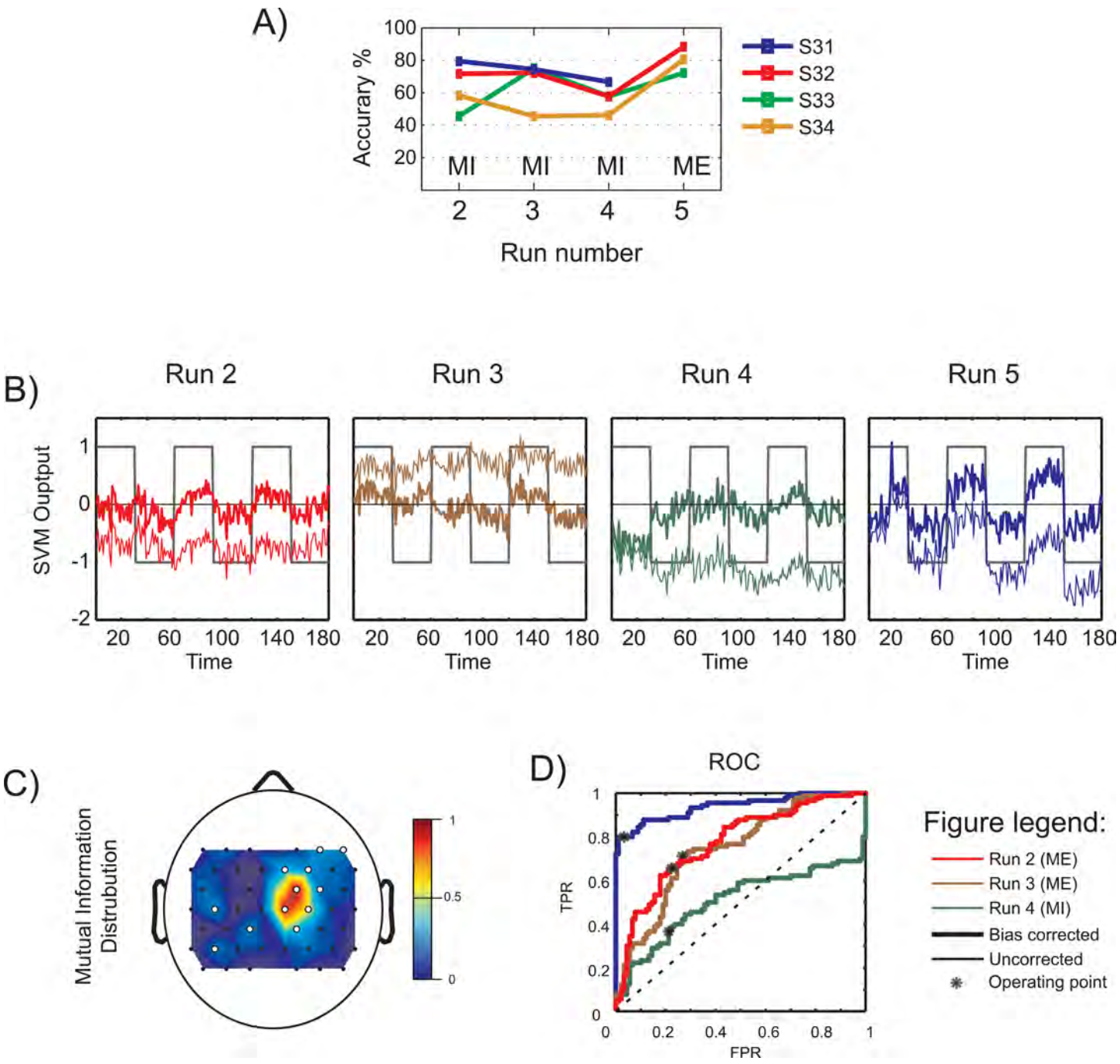

Fig 7. Subject-independent classification results and parameters. A) Online classification accuracies for each run. B) The SVM outputs obtained from the online classification. The uncorrected and bias-corrected values are represented using thin and thick lines resp. The class of data is indicated as +1 for right hand -1 for left hand blocks. C) The spatial distribution of mutual information for the ensemble data training set. The white dots indicate channels with high mutual information and hence selected. D) ROC curves of the classifiers used in the different runs of online classification. The operating point is indicated by an asterisk (*).

doi:10.1371/journal.pone.0159959.g007

The intermediate results of feature selection and classification and were reported in the previous section. The channels chosen using mutual information based feature selection are found to lie over the motor cortex in most of the cases. The bias correction that provides an intra-run

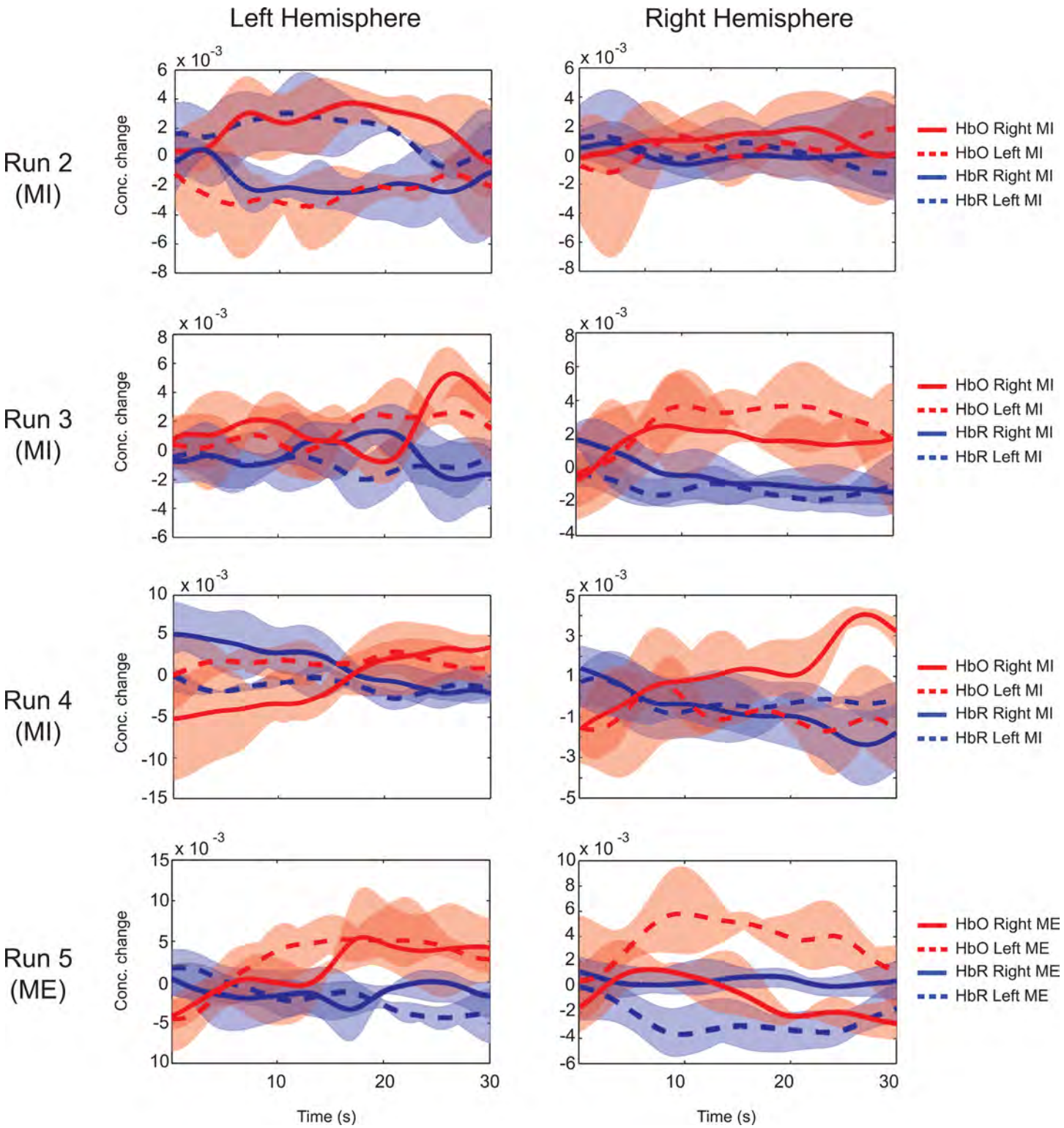

Fig 8. Average time series activations in Subject S32 during Experiment 3. Runs 2–5 indicate activation levels given by concentration changes of HbO and HbR averaged over trials and selected channels. The channel selection is based on highest mutual information between left and right blocks. Note: Y-axis labels are different for left and right panels for better visualization of differences.

doi:10.1371/journal.pone.0159959.g008

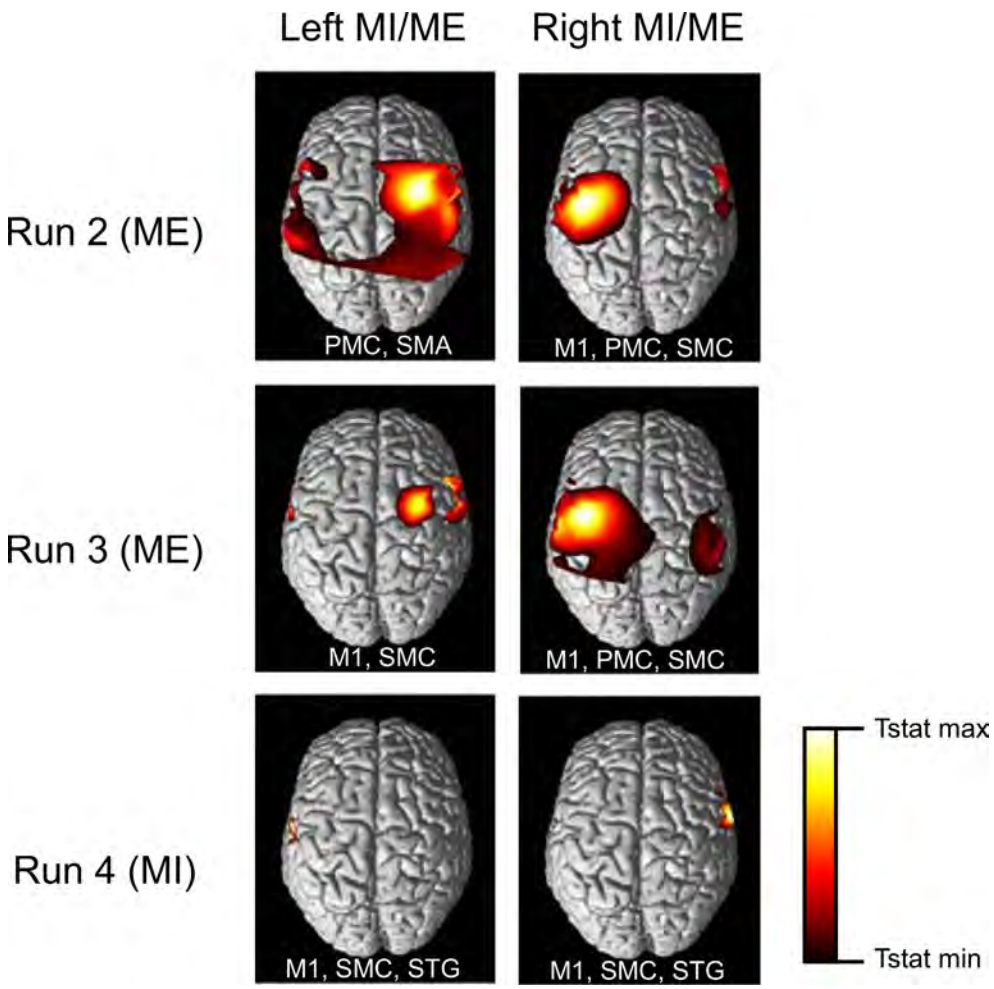

Fig 9. Experiment 1: Thresholded t-statistics maps. The statistically significant activations ($p<0.001$) during bilateral ME and MI for different runs are as shown. Abbreviations of the major areas activated in the contralateral hemisphere are written within each panel. The major areas activated include PMC: Pre-Motor Cortex, M1: Primary Motor Cortex, SMA: Supplementary Motor Area. MI activated superior temporal gyrus (in addition to others) in the final run.

doi:10.1371/journal.pone.0159959.g009

classifier adaptation clearly results in better classification accuracies. The performance of the binary classifiers used in various runs is demonstrated using ROC curves, with the operating point defining the threshold at which the system uses the classifier model. The runs with good classification accuracies generate almost ideal ROC curves, with their operating point in the high TPR-low FPR region. Each of the parameters are inter-related, and together, they define the real-time system.

The change in levels of HbO and HbR during ME and MI have been reported in earlier studies [4,11]. In our study, the time averages over the selected channels in both hemispheres are shown in Figs 5, 6 and 8. ME/MI is accompanied with activations in the contralateral hemisphere that reflect as a rise in HbO and a dip in HbR levels. For ME, we demonstrate a distinct representation of hemodynamic activity in various hemispheres for different runs. For MI, the discrimination is not as good as ME, due to lower levels of activation. The time series of the hemodynamic activity in these selected features is shown. Figs 9, 10 and 11 show the activation maps as heat-maps along with the channels used for feature selection. Interestingly, when

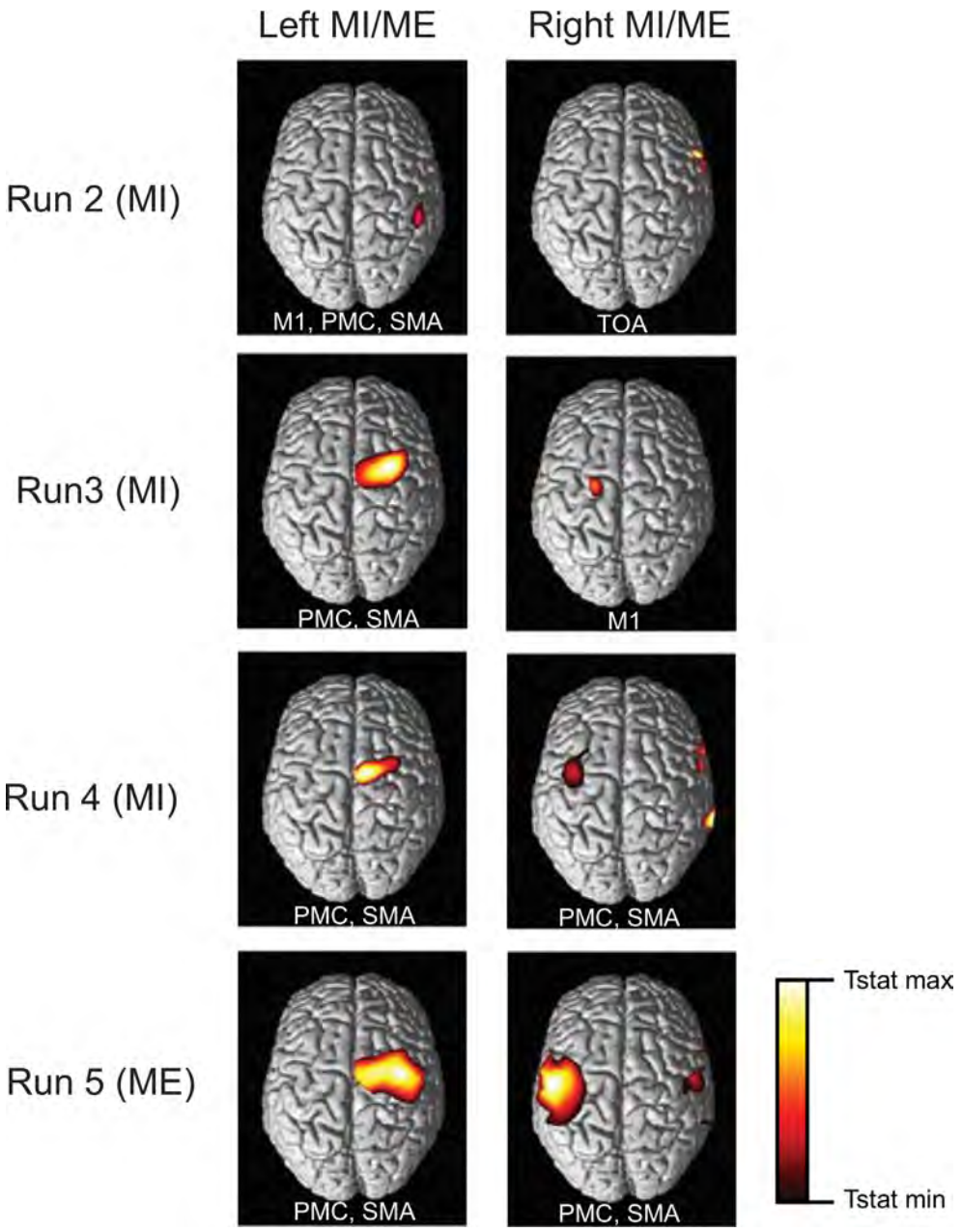

Fig 10. Experiment 2: Thresholded t-statistics maps. The statistically significant activations during bilateral MI and ME for different runs are as shown. Abbreviations of the major areas activated in the contralateral hemisphere are written within each panel. MI activates somatosensory cortex and temperopolar areas (TOA) in addition to Primary Motor Cortex (M1), Supplementary Motor Area (SMA) and Pre-Motor Cortex (PMC). For the MI runs the activations are for $p<0.05$ and for ME the activations are for $p<0.001$.

doi:10.1371/journal.pone.0159959.g010

contrasted with ME, the MI runs had activations that were more anterior and apical, localizing around the SMA. An earlier study comparing fMRI-BOLD activations between MI and ME in a similar task reports similar activations, with ME leading to larger activations in the M1 (primary motor cortex) and MI leading to higher activations in the SMA that localize towards the apical portion of the brain [12]. Although it appears that our results provide supporting evidence to this report, our interpretation cannot be conclusive due to the technical difficulties of

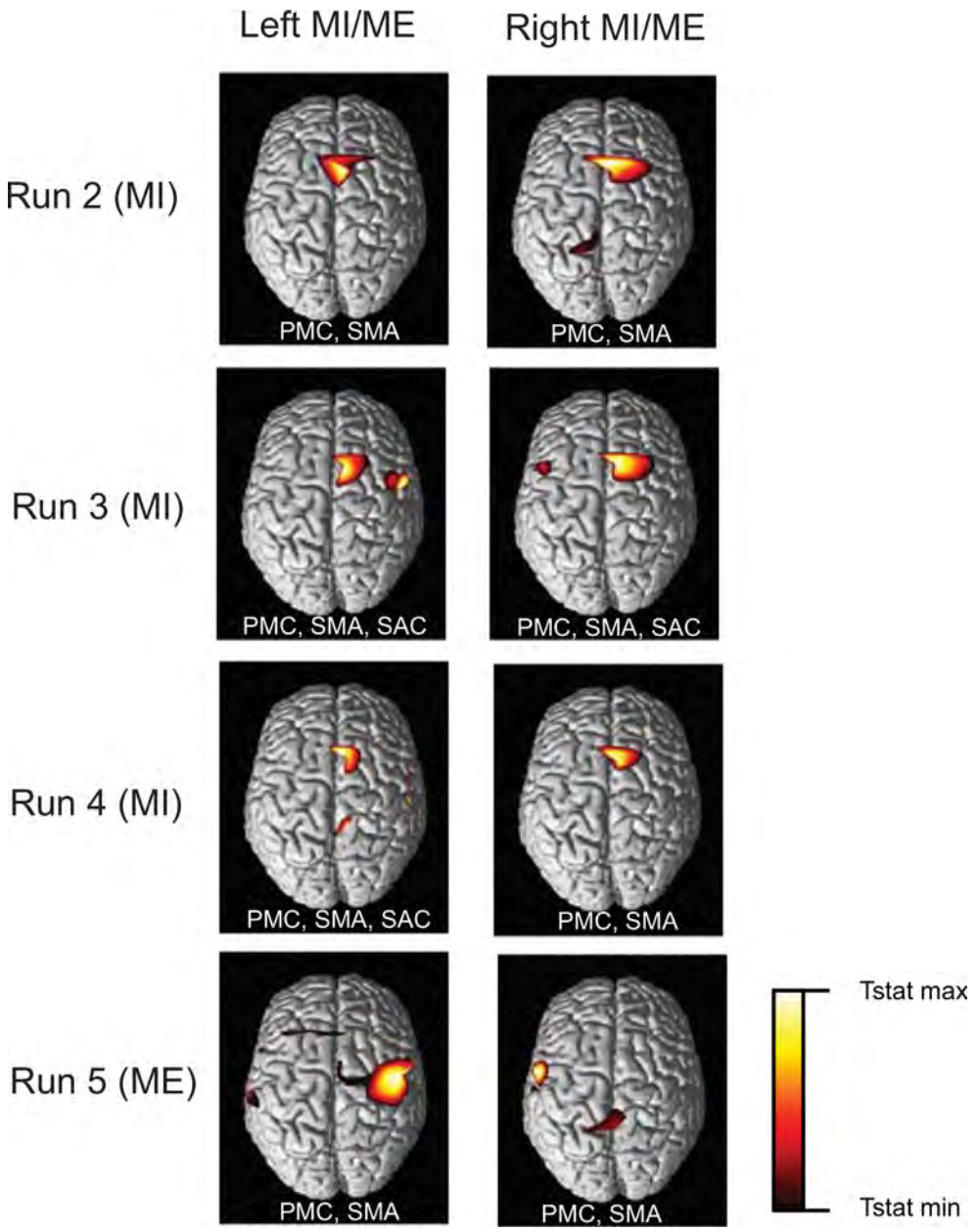

Fig 11. Experiment 3: Thresholded t-statistics maps. The statistically significant ($p<0.001$) activations during bilateral ME and MI for different runs are as shown. Abbreviations of the major areas activated in the contralateral hemisphere are written within each panel. In addition to Pre-Motor Cortex (PMC), Supplementary Motor Area (SMA) and Primary Motor Cortex (M1), primary somatosensory cortex (S1) was also activated during motor imagery runs as shown.

doi:10.1371/journal.pone.0159959.g011

proper co-registration of fNIRS optodes with the corresponding structural MRI of each subject.

Furthermore, the study is expected to bring us a step closer to assist stroke-patient rehabilitation using the subject-independent classifier with real-time neurofeedback. The study in healthy subjects can potentially be applied to patients with more optimizations. Also, the subject-independent motor activation patterns from healthy subjects can be used to train patients

with motor disabilities to imitate and later even generate similar patterns. Studies testing the feasibility of using BCIs for stroke rehabilitation found statistically and clinically significant gains in motor control and functional tasks in response to motor learning combined with functional electric stimulation (FES); [13,14]. Though these studies were quite promising, normal motor control and function were not completely attained, and not all subjects had significant improvement. Current theories in motor learning and instrumental conditioning of the brain responses propose a novel approach of closed-loop BCI for effective recovery of movement [15], by conditioning spatio-temporal patterns of the brain responses associated with the desired movement, concurrently with the afferent sensory input induced by peripheral stimulation of the muscles of the limbs that produces movement. A hypothesis that can be tested with real-time subject-independent classification and feedback is that: by training patients to produce normal brain activity, one may be able to influence brain plasticity that results in normal brain function and motor behavior. In the case of motor function, this strategy is supported by evidence that practicing movements that are as close to normal as possible might help to improve motor function [16], by guiding newly sprouting axons to the appropriate cortical regions [17]. The development of a subject-independent classifier based BCI is thus an important step towards successful stroke rehabilitation.

The results obtained in our experiments suggest the applicability of our technique for neurofeedback experiments. However, the system is still open to modifications in areas such as robustness, usability etc. The subject-independent classifier model, even though its performance is as good as subject-dependent classifiers, can still be optimized by incorporating head size, shape and activation pattern information from the individual subjects involved. The usability indicates the preparation time for the data acquisition and the extent to which subject can wear the equipment. Currently, it takes a long time for setting up the head cap, as it involves managing the obstructing hair from the optical path. Most of the subjects reported discomfort after wearing the cap for over 45 minutes, and pointed this out as a reason for failing to do well in the motor task. These are limitations in the current study and we intend to look into further possibilities to address them in the future. Furthermore, future studies should look at comparing the brain and behavioral changes induced by neurofeedback training with subject-independent classification and subject-dependent classification in a controlled manner so that the advantages and disadvantages of the methods are identified. Here, we present a preliminary step to extract optimal features in a motor activity and apply it on a simple adaptive classification system to provide better binary classifications. Concluding the subject's capability to regulate his own brain activity using neurofeedback is thus beyond the scope of this study.

Conclusions

In conclusion, this study primarily focuses on real-time binary classification of left versus right hand movement execution and imagery using a SVM based classifier. A subject-independent pattern classifier generated from movement execution data using the feature extraction and selection strategy discussed above was used in real-time classification of MI and ME. The neuronal activity correlates between MI and ME were explored and utilized to create a generic classifier. The performance of the system in terms of bilateral movement classification accuracies obtained in various sessions of the different subjects are reported. The classifier parameters obtained in each of the experiments conducted, indicating robust and accurate performance, are separately discussed. The data are analyzed offline to identify the spatial and temporal activations and the results were also demonstrated. The results are promising, and we hope to overcome and address the various drawbacks of the current system, and to develop a real-time BCI system for clinical rehabilitation purposes.

Author Contributions

Conceived and designed the experiments: RS. Performed the experiments: NR AZ. Analyzed the data: NR AZ. Contributed reagents/materials/analysis tools: MR. Wrote the paper: NR AZ RS. Edited manuscript: MR VAP CG NB.

References

1. Sulzer J., Haller S., Scharnowski F., Weiskopf N., Birbaumer N., Blefari M. L., et al. (2013). Real-time fMRI neurofeedback: progress and challenges. Neuroimage, 76, 386–399. doi: 10.1016/j.neuroimage.2013.03.033 PMID: 23541800
2. Birbaumer N, Ruiz S, Sitaram R (2013). Learned regulation of brain metabolism. Trends in Cognitive Sciences 17: 295–302. doi: 10.1016/j.tics.2013.04.009 PMID: 23664452
3. Sitaram R., Lee S., Ruiz S., Rana M., Veit R., & Birbaumer N. (2011). Real-time support vector classification and feedback of multiple emotional brain states. Neuroimage, 56(2), 753–765. doi: 10.1016/j.neuroimage.2010.08.007 PMID: 20692351
4. Sitaram R., Zhang H., Guan C., Thulasidas M., Hoshi Y., Ishikawa A., et al. (2007). Temporal classification of multichannel near-infrared spectroscopy signals of motor imagery for developing a brain–computer interface. NeuroImage, 34(4), 1416–1427. PMID: 17196832
5. Mihara M., Miyai I., Hattori N., Hatakenaka M., Yagura H., Kawano T., et al (2012). Neurofeedback using real-time near-infrared spectroscopy enhances motor imagery related cortical activation. PloS one, 7(3), e32234. doi: 10.1371/journal.pone.0032234 PMID: 22396753
6. Ang K. K., Chin Z. Y., Zhang H., & Guan C. (2012). Mutual information-based selection of optimal spatial–temporal patterns for single-trial EEG-based BCIs. Pattern Recognition, 45(6), 2137–2144.
7. Ang, K. K., Yu, J., & Guan, C. (2012, June). Extracting and selecting discriminative features from high density NIRS-based BCI for numerical cognition. In *The 2012 International Joint Conference on Neural Networks (IJCNN)* (pp. 1–6). IEEE.
8. Vapnik V. N., & Vapnik V. (1998). Statistical learning theory (Vol. 1). New York: Wiley.
9. Coyle S, Ward T, Markham C (2004) Physiological noise in near-infrared spectroscopy: implications for optical brain computer interfacing. Conf Proc IEEE Eng Med Biol Soc 6: 4540–4543. PMID: 17271316
10. Ye J. C., Tak S., Jang K. E., Jung J., & Jang J. (2009). NIRS-SPM: statistical parametric mapping for near-infrared spectroscopy. Neuroimage, 44(2), 428–447. doi: 10.1016/j.neuroimage.2008.08.036 PMID: 18848897
11. Abdelnour A. F., & Huppert T. (2009). Real-time imaging of human brain function by near-infrared spectroscopy using an adaptive general linear model. Neuroimage, 46(1), 133–143. doi: 10.1016/j.neuroimage.2009.01.033 PMID: 19457389
12. Dechent P., Merboldt K. D., & Frahm J. (2004). Is the human primary motor cortex involved in motor imagery?. Cognitive Brain Research, 19(2), 138–144. PMID: 15019710
13. Daly J. J., Hogan N., Perepezko E. M., & Krebs H. I. (2005). Response to upper-limb robotics and functional neuromuscular stimulation following stroke. Journal of rehabilitation research and development, 42(6), 723. PMID: 16680610
14. Daly J. J., Cheng R., Rogers J., Litinas K., Hrovat K., & Dohring M. (2009). Feasibility of a new application of noninvasive brain computer interface (BCI): a case study of training for recovery of volitional motor control after stroke. Journal of Neurologic Physical Therapy, 33(4), 203–211. doi: 10.1097/NPT.0b013e3181c1fc0b PMID: 20208465
15. Silvoni S., Ramos-Murguialday A., Cavinato M., Volpato C., Cisotto G., Turolla A., et al. (2011). Brain-computer interface in stroke: a review of progress. Clinical EEG and Neuroscience, 42(4), 245–252. PMID: 22208122
16. Nudo R. J., Wise B. M., SiFuentes F., & Milliken G. W. (1996). Neural substrates for the effects of rehabilitative training on motor recovery after ischemic infarct. Science, 272(5269), 1791. PMID: 8650578
17. Carmichael S. T., Wei L., Rovainen C. M., & Woolsey T. A. (2001). New patterns of intracortical projections after focal cortical stroke. Neurobiology of disease, 8(5), 910–922. PMID: 11592858